

# Oxide-Based Solid-State Batteries: A Perspective on Composite Cathode Architecture

Yaoyu Ren, Timo Danner, Alexandra Moy, Martin Finsterbusch, Tanner Hamann, Jan Dippell, Till Fuchs, Marius Müller, Ricky Hofst, André Weber, Larry A. Curtiss, Peter Zapol, Matthew Klenk, Anh T. Ngo, Pallab Barai, Brandon C. Wood, Rongpei Shi, Liwen F. Wan, Tae Wook Heo, Martin Engels, Jagjit Nanda, Felix H. Richter, Arnulf Latz, Venkat Srinivasan,\* Jürgen Janek,\* Jeff Sakamoto,\* Eric D. Wachsman,\* and Dina Fattakhova-Rohlfing\*

The garnet-type phase  $\text{Li}_7\text{La}_3\text{Zr}_2\text{O}_{12}$  (LLZO) attracts significant attention as an oxide solid electrolyte to enable safe and robust solid-state batteries (SSBs) with potentially high energy density. However, while significant progress has been made in demonstrating compatibility with Li metal, integrating LLZO into composite cathodes remains a challenge. The current perspective focuses on the critical issues that need to be addressed to achieve the ultimate goal of an all-solid-state LLZO-based battery that delivers safety, durability, and pack-level performance characteristics that are unobtainable with state-of-the-art Li-ion batteries. This perspective complements existing reviews of solid/solid interfaces with more emphasis on understanding numerous homo- and heteroionic interfaces in a pure oxide-based SSB and the various phenomena that accompany the evolution of the chemical, electrochemical, structural, morphological, and mechanical properties of those interfaces during processing and operation. Finally, the insights gained from a comprehensive literature survey of LLZO–cathode interfaces are used to guide efforts for the development of LLZO-based SSBs.

## 1. Introduction


There is considerable interest in the development of solid-state batteries (SSBs), which use solid electrolytes (SE) to supplant liquid electrolytes (LE). The motivation for this is the expectation of improved cell properties in terms of energy density, operating temperature range, stability, and safety—depending on the specific type of SSB. Currently, several SSB cell concepts are under consideration, distinguished by the type of SE: oxides, sulfides, halides, and polymers; each with relative advantages and disadvantages that impact their commercial viability.

The garnet-type  $\text{Li}_7\text{La}_3\text{Zr}_2\text{O}_{12}$  (LLZO) oxide is unique among this subset of SEs due to its: 1) relatively high ionic conductivity up to  $2 \text{ mS cm}^{-1}$  at  $25^\circ\text{C}$ , which can be tuned by doping elements;<sup>[1]</sup>

Y. Ren,<sup>[††]</sup> T. Hamann, R. Hofst, E. D. Wachsman  
Maryland Energy Innovation Institute (MEI<sup>2</sup>)  
University of Maryland (UMD)  
College Park, MD 20742, USA  
E-mail: ewach@umd.edu

T. Danner, J. Dippell, A. Latz  
Deutsches Zentrum für Luft- und Raumfahrt  
(DLR) – Helmholtz-Institut Ulm (HIU)  
Helmholtzstraße 11, 89081 Ulm, Germany

A. Moy, J. Sakamoto  
Mechanical Engineering  
University of Michigan (UofM)  
2350 Hayward Ave., Ann Arbor, MI 48109, USA  
E-mail: jeffsaka@umich.edu

 The ORCID identification number(s) for the author(s) of this article can be found under <https://doi.org/10.1002/aenm.202201939>.

<sup>[†]</sup>Present address: School of Materials Science and Engineering, Harbin Institute of Technology, Shenzhen 518055, China

<sup>[††]</sup>Present address: School of Materials Science and Engineering, Tsinghua University, Beijing 100084, China

© 2022 The Authors. Advanced Energy Materials published by Wiley-VCH GmbH. This is an open access article under the terms of the Creative Commons Attribution-NonCommercial License, which permits use, distribution and reproduction in any medium, provided the original work is properly cited and is not used for commercial purposes.

DOI: 10.1002/aenm.202201939

M. Finsterbusch, M. Engels, D. Fattakhova-Rohlfing  
Forschungszentrum Jülich (FZJ)  
Institute of Energy and Climate Research (IEK-1)  
Wilhelm-Johnen-Straße, 52425 Jülich, Germany  
E-mail: d.fattakhova@fz-juelich.de

T. Fuchs, F. H. Richter, J. Janek  
Institute of Physical Chemistry  
Justus-Liebig University Giessen (JLU)  
Heinrich-Buff-Ring 17, 35392 Giessen, Germany  
E-mail: juergen.janek@phys.chemie.uni-giessen.de

M. Müller, A. Weber  
Karlsruher Institut für Technologie (KIT)  
Institute for Applied Materials – Electrochemical Technologies (IAM-ET)  
Adenauerring 20b, 76131 Karlsruhe, Germany

L. A. Curtiss, P. Zapol, M. Klenk, A. T. Ngo, P. Barai, V. Srinivasan  
Argonne National Laboratory (ANL)  
Lemont, IL 60439, USA  
E-mail: vsrinivasan@anl.gov

B. C. Wood, R. Shi,<sup>[†]</sup> L. F. Wan, T. W. Heo  
Laboratory for Energy Applications for the Future (LEAF)  
Lawrence Livermore National Laboratory  
Livermore, CA 94550, USA

J. Nanda  
Oak Ridge National Laboratory (ORNL)  
Energy Storage and Conversion Group  
Chemical Sciences Division  
Oak Ridge, TN 37830, USA

2) processability in air; 3) high shear modulus compared to lithium to physically stabilize the anode interface; and 4) wide electrochemical stability window extending from the low potential of lithium metal to potentials higher than any current commercial cathode. As a ceramic oxide, LLZO provides unprecedented safety even at high operating temperatures, and can enhance safety in combination with other SEs. This unique combination of properties makes LLZO an attractive candidate for the development of safe and robust SSBs with potentially high energy density, provided it can be combined with lithium metal anodes and high-energy cathodes. Some previous reports have estimated theoretical densities of up to  $>400 \text{ Wh kg}^{-1}$  and  $>1000 \text{ Wh L}^{-1}$  for garnet-based SSBs.<sup>[2]</sup> However, practically achieved energy densities fall short of these values, and there is still an ongoing debate about a realistic estimate of theoretical energy density for practical LLZO-based cell concepts.

The lithium metal anode has been intensely studied in recent years and significant progress has been made in understanding the stability of LLZO/Li anode interfaces and lithium stripping/plating behavior. The state of research is summarized and analyzed in numerous reviews.<sup>[3]</sup> Owing to these efforts, Li/LLZO anode half cells capable of operating at  $10 \text{ mA cm}^{-2}$  at room temperature with no applied pressures have been demonstrated by the Wachsmann<sup>[4]</sup> and Sakamoto<sup>[5]</sup> groups. These high current densities were achieved at a cycling capacity of  $0.16 \text{ mAh cm}^{-2}$  with a planar interface<sup>[5]</sup> and in extended 3D interface architectures more commercially relevant capacities of  $1.25 \text{ mAh cm}^{-2}$ , with in fact over  $5 \text{ mAh cm}^{-2}$  demonstrated at  $2.5 \text{ mA cm}^{-2}$ .<sup>[4]</sup> As such, the SSB cathode is becoming the next frontier.

SSB cathodes, like Li-ion battery cathodes, are commonly a “composite cathode” due to its 3D design consisting of a random solid-state distribution of cathode active material (CAM) and SE (in some cases also with a carbon additive).<sup>[6]</sup> However, while significant progress has been made in composite cathodes using sulfide SEs, LLZO-based composite cathodes still lack sufficient performance and processing technology. One of the major reasons for the disparity in progress can be attributed to the ease in composite cathode manufacturing using sulfides (essentially compaction of mixed powders) compared to sintering LLZO and CAM in a composite cathode 3D structure. In fact, the cathode composite of oxide-based SSBs, its various interfaces and the charge transport properties are the major remaining challenges to enable high-performance LLZO-based SSBs.

Due to the polycrystalline nature of LLZO-based SSBs, they typically contain more interfaces than conventional liquid-based batteries or SSBs with soft and glassy SEs (such as polymers and sulfides). In general, the total internal resistance of a battery is defined by: 1) the total electronic/ionic resistance of the cathode; 2) the homo-ionic interface resistance between the grains of the active cathode and anode materials; 3) the heteroionic interface resistance between the SE and the CAM and SE and anode active materials (AAM), respectively; and 4) the resistance of the SE. In contrast to a continuity of LE resistance throughout the cell structure, for polycrystalline SEs, such as LLZO, it is largely determined by the homoionic interface resistance, e.g., grain boundaries (GBs), formed

during densification. The unique role of GBs in the ion transport distinguishes oxide-type SEs from soft and glassy (polymer and sulfide) SEs. The other important differences arise from the rigid nature of all interfaces in oxide SSBs and the need for densification at high temperatures (typically  $>1000 \text{ }^\circ\text{C}$ ) to chemically bond the particles and transform them into dense polycrystalline microstructures.

**Figure 1** provides an overview of the numerous homo- and heteroionic interfaces in an oxide SSB and of the phenomena that accompany the evolution of the chemical, electrochemical, structural, morphological, and mechanical properties of the interfaces during processing and operation.

Given the key role of cathode composites in the advancement of LLZO-based SSBs, the current perspective aims to discuss the critical issues that need to be addressed to achieve the ultimate goal of an all-solid-state LLZO-based battery that delivers high energy density at practical charge/discharge rate without degradation. As analyzed in benchmarking studies, competitive SSB cells should be able to achieve current densities up to  $10 \text{ mA cm}^{-2}$ , which, together with energy efficiency requirements, leads to an internal cell resistance of less than  $30 \text{ } \Omega \text{ cm}^2$ .<sup>[7]</sup> How this translates into material and structural requirements for a high-performance LLZO-based cathode composite is the main focus of this perspective. Our perspective complements existing reviews of solid/solid interfaces, with more emphasis on understanding interfacial phenomena. We do not address the phenomena related to  $\text{Li}^+/\text{H}^+$  exchange in LLZO, which is discussed in a recent comprehensive review.<sup>[6m]</sup>

We summarize the current state of knowledge in the field of cathode composites with oxide SEs and use the knowledge gained to calculate realistic theoretical energy density values to guide future oxide-based SSB development. Both experimental and theoretical advances are addressed, and prospects for linking these two complementary sets of tools are identified. Since good interface kinetics is key to fast charge and discharge steps, we focus on the mechanism of charge transfer across interfaces in LLZO-cathode half cells and on degradation processes during processing and operation. To identify critical bottlenecks, we draw a comparison with other SEs and also consider hybrid cathode composites containing a small fraction of liquid, gel or polymer electrolytes.

Our review is organized into seven topical sections that address solid electrolyte GBs in Section 2, the formation of SE/CAM interfaces during processing in Section 3, the behavior of SE/CAM interfaces during operation in battery cells in Section 4, the comparison with the other types of SEs in Section 5, and the approach of influencing poor interface kinetics through the formation of hybrid composites with non-solid components in Section 6. The insights gained from the literature on the interfacial properties are then used for the calculation of SSB energy density and rate capability and a detailed analysis of the prospect for oxide-based SSBs in Section 7.

## 2. Internal Electrolyte Interfaces

SE transport properties, across the dense separator layer and in any SE extending into the electrode structures, affect the cell

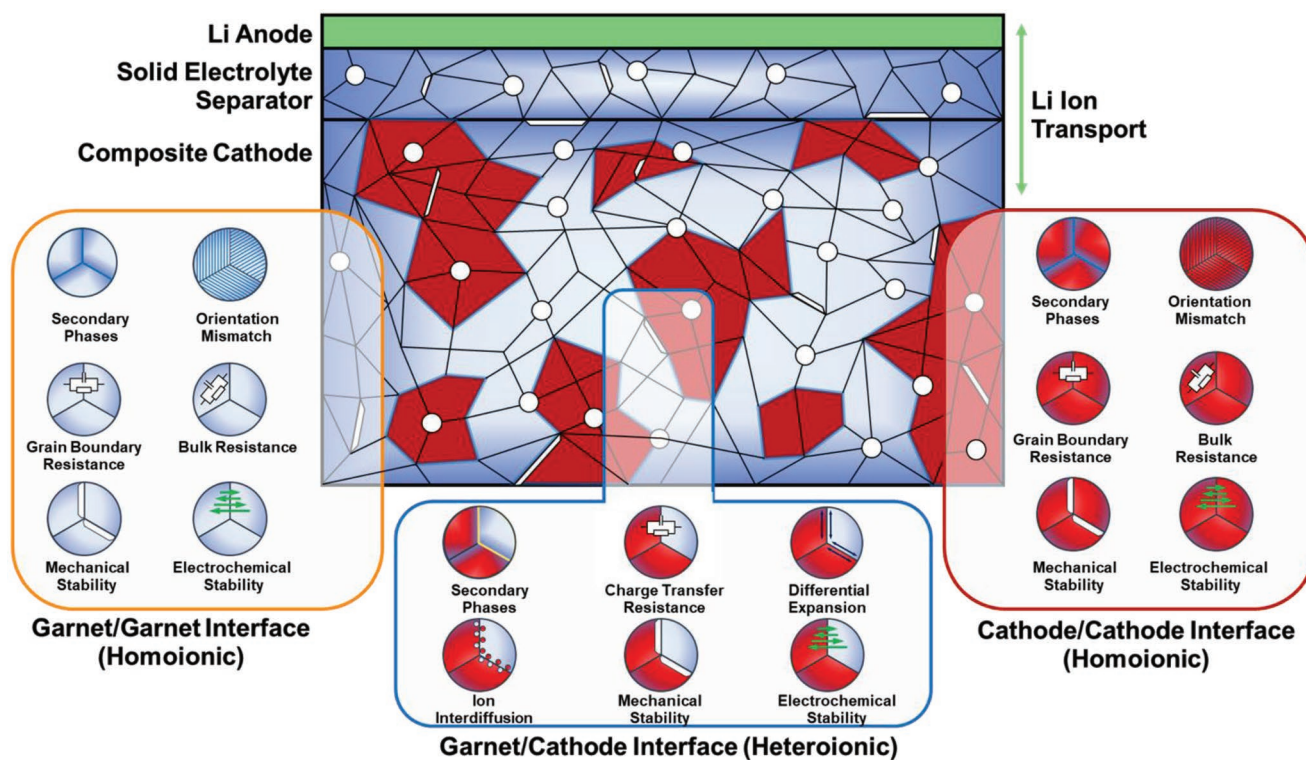


**Figure 1.** Overview of homo- and heteroionic interfaces in an oxide SSB and the phenomena that accompany the evolution of chemical, electrochemical, structural, morphological, and mechanical properties of the interfaces during processing and operation. White circles symbolize the pores.

resistance and ultimate performance. Therefore, to minimize the SE network resistance, it is necessary to understand the correlation between processing, microstructure, ion conduction, mechanical properties, and cell performance. Traditional solid-state synthesis of LLZO solid electrolytes consists of two steps:<sup>[8]</sup> powder synthesis by calcination and then densification by high temperature (>1000 °C) sintering, which also chemically bonds particles resulting in a polycrystalline microstructure. Typically, the goal is to achieve relative densities >95%. Understanding the underpinning mechanisms that control the evolution of oxide electrolyte particles into dense polycrystalline microstructures is necessary to develop viable LLZO-based components.

To understand the microstructural evolution, ideally in situ analyses should be used to characterize the evolution of particles into grains and GBs in polycrystalline microstructures. In situ analyses are however exceptionally challenging to conduct and as a result data are limited. As an alternative to in situ analyses, there have been numerous ex situ analyses that use a broad range of characterization approaches and tools to extrapolate and understand how variables such as densification time, temperature, and pressure affect relative density, GBs and other microstructural features. In addition to processing parameters, the chemical composition such as lithium content and cubic garnet-stabilizing dopants can affect grain morphology, stability, mechanical and transport properties. Therefore, the role of lithium loss, dopant type and concentration on the microstructural evolution are discussed. These experimental data provide guidance for theoretical studies to better understand lithium-ion

conductivity in grains and in poorly understood GBs. **Figure 2** provides experimental and theoretical insights into the phenomena that occur at the atomistic, microstructural, and macroscale.

## 2.1. Grain Boundaries in Garnet Phases and Evolution during Processing

### 2.2.1. Effects of Processing on Grain Boundary Structure and Composition

Although challenging to achieve due to the complex structure of LLZO and its sensitivity to air and electron beams, ex situ observations of individual GBs have been accomplished. Through TEM, EELS, EDX, EBSD, and X-ray Laue diffraction, these few studies have suggested some of the general properties, structures, and morphologies of GBs in LLZO. Wolfenstine et al.<sup>[15]</sup> and, more recently, Liu et al.<sup>[10]</sup> observed that LLZO has a thin GB ( $\approx 1.5$  nm) without evidence of amorphous or secondary phase formation. However, Kumazaki et al.<sup>[16]</sup> and Basappa et al.<sup>[17]</sup> observed that LLZO GBs contain secondary phases and are wider than the previous two studies. Hints for secondary phases are also found in classical molecular dynamics (MD) and Monte Carlo (MC) simulations.<sup>[18]</sup> Li and O co-segregation at the GBs were observed, which indicates potential formation of new lithium-rich secondary phases at the GBs. The formation of secondary phases and the difference are likely due to variations in sintering and densification



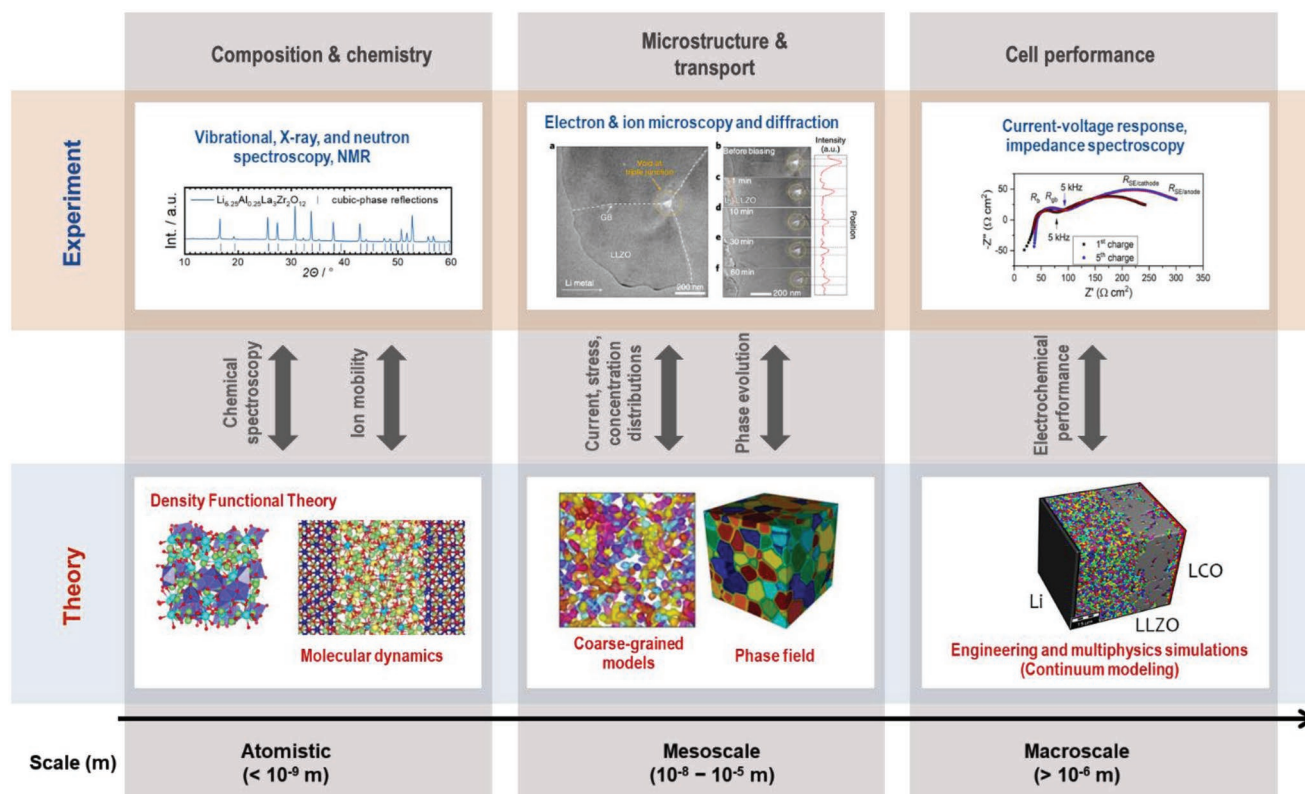


**Figure 2.** Internal interfaces cross-cutting relationships between experimental and theoretical techniques across multiple length scales. From top left, clockwise: Diffraction techniques to analyze atomic positions; Reproduced with permission.<sup>[9]</sup> Copyright 2020, ACS. Transmission electron microscopy of LLZO grain boundary triple points; Reproduced with permission.<sup>[10]</sup> Copyright 2021, Springer Nature. Electrochemical impedance spectroscopy of LLZO with lithium indium and lithium cobalt oxide electrodes; Reproduced with permission.<sup>[11]</sup> Copyright 2022, ACS. Virtual cell with lithium and LLZO/LCO composite electrodes for continuum simulations; Reproduced with permission.<sup>[12]</sup> Copyright 2018, ACS. Grain and phase field modeling of LLZO; Reproduced with permission.<sup>[13]</sup> Copyright 2021, Springer Nature. And atomic level modeling of LLZO and LLZO/electrode interfaces.<sup>[14]</sup>

parameters, such as pressure, doping, and particle coating, as discussed in more detail below. Through the use of TEM, it has been observed that samples densified without applied pressure have secondary phases (e.g., ternary Li-Al-O phases) in the GBs, while those sintered under pressure often do not.<sup>[10,15,16]</sup> The presence of secondary phases seems to be independent of the fact that the densification temperature was above the lithia-alumina eutectic.<sup>[10,15]</sup> However, due to the small number of studies performed, further work is necessary to verify this conclusion. Secondary phases may be absent from the GBs of LLZO processed under pressure due to the shorter required densification time for pressure-assisted methods (less than one hour for rapid induction hot pressing (RIHP) and spark plasma sintering (SPS)<sup>[19]</sup>). With increasing densification time at the temperatures used for sintering, the so called “lithium loss” (due to sublimation of lithia or reactions with the substrate or setter material) increases, and so does the evolution of secondary phases. Another contribution to the formation of secondary phases could be the effect of relative density, as porosity and secondary phases tend to accumulate around GBs. As such, it is expected that samples densified without pressure, and/or with a lower relative density, may be more likely in some cases to form secondary phases at the GBs than those processed under pressure. However, while pressure can enhance densification, current pressurized sintering techniques are

batch processes and therefore not as scalable as pressure-less densification. Therefore, insights gained through pressurized densification should ideally be translated to advance pressure-less sintering.

### 2.2.2. Ex Situ and Computational Analysis of Grain Boundary Orientation

Using electron backscatter diffraction (EBSD) and X-ray Laue diffraction, Cheng et al.<sup>[20]</sup> (pressure-less densification) and Sharafi et al.<sup>[21]</sup> (pressure-assisted densification) showed that LLZO consists of random GB misorientation distributions and similar misorientation angle averages ( $\approx 39^\circ$ ). Random misorientation in pressure-assisted sintering was also confirmed in TEM by Liu et al.<sup>[10]</sup> These findings suggest that while pressure can play a role in GB morphology and structure, the misorientation angle is independent of pressure and perhaps temperature. However, it is also possible that the crystal structure affects misorientation, e.g., misorientation angles may be less affected in a cubic crystal system such as in LLZO compared to less symmetric crystal systems.

Recent theoretical studies have provided additional insights into GB structures and orientations that can inform and guide the experimental investigations. While direct modeling

of sintering and processing behavior is one approach, it has generally not been pursued to build models of GBs in LLZO. Instead, atomic-scale simulations have focused on identifying possible GB structures as well as analyzing the effect of GBs on transport properties. Atomistic modeling of LLZO GBs has generally focused on highly ordered structures. For example, Yu and Siegel investigated coherent symmetric tilt, low-energy GBs of LLZO using classical MD and MC simulations.<sup>[18]</sup> Using a similar computational approach, Shiiba et al.<sup>[22]</sup> surveyed additional GB configurations using MD. Even for these narrow, well-defined GB types, the authors found that the atomic arrangements within the GBs can differ drastically from the crystalline grains with certain orientations, e.g.,  $\Sigma 3(100) \times (2-12)$ , closely resembling a locally amorphous arrangement. Lithium-deficient regions were generally observed at the GBs, which could be responsible for the lower lithium-ion conductivities. In addition to these well-defined GB orientations, Heo et al.<sup>[13]</sup> recently adopted a different approach by representing the atomic rearrangement in the interior of generic high-angle GBs with a range of disordered structures generated from MD simulations using a melt-and-quench technique. The authors also tested different densities and Li concentrations to account for potential variations in Li distribution and atomic spacing at the GBs. These disordered models reflected the atomic-scale characteristics of incoherent GB structures, keeping  $\text{LaO}_8$  and  $\text{ZrO}_6$  polyhedra intact while reorienting and disordering their lattice arrangements. The different local arrangements also gave rise to a broad distribution of local transport behavior, thus suggesting a connection between local atomic structural environments and lithium-ion mobility. Alongside this computational analysis, it is suggested that further TEM and EBSD analyses could be used to validate these models and provide a broader view of the range of possible local atomic arrangements within GBs.

Additionally, space charge layers (SCLs) might play a role in the transport across the GBs. Continuum models for ceramic materials have been transferred to Li-ion conducting solid electrolytes<sup>[23]</sup> to correlate material properties with SCL thickness, capacity, and resistance.<sup>[23a,24]</sup> However, the effect of the GB orientation and the complex dependence on local atomic structural environments in the SCL on the lithium mobility<sup>[24a,25]</sup> and resulting effective GB conductivity has not been considered in the models.

Owing to the complex nature of grain boundaries, it will also be important to integrate the influence of processing condition in the analysis, in particular with respect to  $\text{Li}_2\text{O}$  vapor pressure during calcination and densification.

### 2.2.3. Microstructural Evolution

In order to mitigate lithium dendrite penetration, enable thin film fabrication, and develop viable composite cathodes, it is important to understand how processing affects microstructural features. Specifically, the various important aspects of the LLZO microstructure can be categorized as: 1) grain size; 2) LLZO volume fraction; 3) percolation factor; 4) constriction factor; and 5) geometric tortuosity.<sup>[26]</sup>

Ex situ observation have been widely adopted by experimentalists to investigate the grain/grain-boundary microstructure of LLZO, which include SEM fractography and particle size analysis, geometric density measurements, XRD, and EDX.<sup>[19a,20,28]</sup> Computational techniques have also been adopted to estimate the above-mentioned effective properties and compare with experiments,<sup>[29,30]</sup> which can be broadly divided into the following categories:

1. Image-based reconstruction of the LLZO microstructure, which uses X-ray computed tomography, or focused ion beam scanning electron microscopy (FIB-SEM).<sup>[26c,27,31]</sup>
2. Random addition of spheres representing cathode and SE domains.<sup>[32]</sup>
3. Discrete element-based methodologies.<sup>[33]</sup>
4. Phase field-based techniques.<sup>[34]</sup>
5. Monte Carlo-based computational schemes.<sup>[35]</sup>

All these computational techniques led to reconstruction of micron-sized LLZO (or cathode/LLZO) microstructures,<sup>[27]</sup> which were used to estimate the ionic and electronic transport limitations at the electrode scale.<sup>[26c,33]</sup>

Microstructural features form during densification, so a fundamental understanding of densification mechanisms and the processing/microstructure relationship is necessary to maximize performance and enable manufacturing. While there are many different processing parameters that can affect the microstructure and the GBs, the focus in this section is on pressure, temperature, time, and particle size. Since it is known that LLZO formulation affects densification behavior, there is a separate discussion on the effect of chemical formula in Section 2.1.4. It is also important to note that all of these processing effects are intertwined; thus, future works that aim to decouple the varying effects of the processing parameters will prove useful in increasing the understanding in the aspects that affect internal interfaces.

While pressure-less densification is successful in ceramic processing, it often comes with microstructural challenges for LLZO. These include incomplete sintering/densification, GBs that are weak resulting in intergranular fracture, lithium loss and secondary phase formation, all of which are detrimental to conductivity.<sup>[16,20,28d,36]</sup> Pressure-assisted densification methods, such as RIHP, SPS, and hot isostatic pressing, were investigated to improve microstructural homogeneity and quality. These methods are often, though not always, successful in creating higher relative density samples (> 97%) with low GB resistance, thereby lowering the resistance of the cells.<sup>[19–21,28,36]</sup> However, as observed by Cheng et al.<sup>[20]</sup> and Sharafi et al.,<sup>[21]</sup> pressure-assisted densification often produces samples with smaller grain sizes due to their shorter processing time, and therefore increased GB area—a feature that is in some cases believed to affect lithium dendrite growth.<sup>[37]</sup> Besides the effect of pressure, the type of pressure-assisted methods applied is also a variable.<sup>[19a,28c]</sup>

Temperature and time are two other major factors in processing that can have significant effects on the resulting microstructure. If the temperature is low and the heating time is short, lithium loss is minimized, but densification can be incomplete. If the temperature is high and heating time is long, densification increases, grain boundary resistance can

decrease, but lithium loss resulting in impurities can be significant.<sup>[19a,28c,d]</sup>

The particle size also plays a role in determining the microstructure. Generally, smaller particles sinter and densify at lower temperatures compared to larger particles.<sup>[19a,20,28a]</sup> During sintering the smaller particles often grow to larger grains, due to their increased curvature. Therefore, smaller particles potentially allow for both a decrease in lithium loss and a reduction of GB area. However, it is important to note that all these studies observed conventional sintering. In pressure-assisted methods, smaller starting particles lead to smaller grains, e.g., comparison between works by Jeff et al.<sup>[38]</sup> and by Wolfenstine et al.<sup>[15]</sup> This difference could be due to the pressure that leads to near immediate densification compared to conventional sintering or to the decreased sintering/densification times used in pressure-assisted methods compared to conventional sintering. This shows that sintering and densification processing parameters are intricately connected.

In order to better understand the influence of mass transport mechanisms on the evolution of LLZO particle microstructure observed at elevated temperatures, multiple-phase field based computational models were developed, where the sintering was assumed to consist of interparticle boundary formation, neck growth, and internal pore shrinkage.<sup>[8,39]</sup> Not only diffusion induced flow of matter, but also advective mass transport due to rigid body motion was taken into account. Wood et al.<sup>[39]</sup> concluded that smaller particles tend to densify quickly, which was well corroborated by experimental observations. Particle size distribution also influences the extent of densification, where bimodal size distributions, containing small-sized particles and large size ratios between the larger and smaller particles, led to better elimination of internal porosity.<sup>[8]</sup> Similar conclusions were drawn in another recent phase-field ceramic sintering study that also incorporated an experimentally informed particle size distribution.<sup>[40]</sup> The authors also investigated the influence of interface properties on sintering kinetics, suggesting a faster densification kinetics for larger surface energies and larger diffusivities for surface and GB diffusion, and a slower densification kinetics for larger GB energy. Although the study used generalized parameters, such sensitivity analysis may guide the selection of dopants for reducing sintering temperature of LLZO.

It has also been computationally observed that adoption of graded particle morphology, with large particles at the center and smaller ones near the periphery, can help to better densify the LLZO samples.<sup>[8]</sup> Increase in grain size during the densification process depends substantially on the initial powder particle sizes. For relatively larger micron-sized particles, no major grain growth occurs.<sup>[41]</sup> However, small cubic-LLZO particles can experience substantial grain growth, which can be easily captured using the existing phase field-based computational methodologies.<sup>[8]</sup>

While the sintering process directly determines the microstructure of the electrolyte, the calcination process influences the microstructure by determining the initial morphology of LLZO particles. Therefore, investigation on the calcination process would be beneficial for understanding the microstructure evolution of the sintered body. Detailed computational modeling of the reaction-sintering that occur during calcination

has not been attempted yet. Comparison with the experimental results reveals that the activation energy during calcination is smaller than the activation energy barrier observed during densification, which alludes to the faster mass transport observed during the reaction-sintering (or calcination) process.<sup>[8]</sup>

#### 2.2.4. Chemical Effects

The cubic garnet *Ia3d* space group can accommodate a broad range of elemental compositions and interstitial site occupancies, many providing fast Li-ion conductivity. Some of the most common compositions differ from LLZO by substituting the zirconium or 16c Wyckoff position with tantalum<sup>[42]</sup> or niobium,<sup>[43]</sup> or substituting interstitial lithium with aluminum<sup>[44]</sup> or gallium.<sup>[45]</sup> Typically, the substitution on the 16c site does not lead to large grains compared to formulas consisting of lithium substitutions, as is the case with aluminum and gallium. Owing to the high bond energy of metal oxides, doping with Ta<sub>2</sub>O<sub>5</sub> and Nb<sub>2</sub>O<sub>5</sub> may not form melt phases at typical densification temperatures (<1250 °C), while Al<sub>2</sub>O<sub>3</sub> and Ga<sub>2</sub>O<sub>3</sub> may react with Li-ions to form liquid phases during sintering. The presence of the melt phase during densification may be the cause for abnormal grain growth as liquid phase sintering is enabled. For example, Jin et al.<sup>[44b]</sup> observed that in aluminum-doped LLZO, a liquid phase fills and conforms to the pores within a network of grains. Moreover, dilatometry measurements showed that accelerated densification occurred at 1055 °C, which is similar to the eutectic temperature of lithia-alumina. It was suggested that the aluminum dopant reacted with oxygen and lithia to make a liquid phase that was expelled or present at GBs. Building upon this notion, Cheng et al.<sup>[46]</sup> analyzed aluminum segregation at GBs using a variety of analytical techniques. It was suggested that the aluminum present at GBs during densification accelerated grain growth to the extent that relatively large grains formed. Similar behavior was observed in the gallium-doped LLZO system. Li et al.<sup>[19a]</sup> and Su et al.<sup>[45d]</sup> studied abnormal grain growth in gallium-doped LLZO and determined that >100 μm grains formed regularly during sintering. Similar to aluminum-doped LLZO, it was proposed by Shinawi and Jaanek<sup>[45b]</sup> that lithia reacts with gallia to form a molten phase that enhances grain growth kinetics.

Another experimentally observed phenomenon that substantially limits the conductivity of sintered LLZO is a lithium loss due to evaporation of lithia from the surface at higher temperature with the formation of a passivating lanthanum-zirconate phase.<sup>[47]</sup> Usually, the pellets or tapes being sintered are covered with extra LLZO or Li<sub>2</sub>CO<sub>3</sub> powder to avoid the lithium loss from the surface. In an attempt to mitigate the impact of lithium loss and avoid the use of valuable material as mother powder, dopants have also been used to stabilize the structure and compensate for lithium loss during sintering,<sup>[44e,48]</sup> but with limited success. Not only does lithium loss change the chemical composition, but volatile lithium compounds (mainly Li<sub>2</sub>O vapor) also have an influence on the LLZO sintering mechanism: a vapor–liquid–solid sintering mechanism was proposed, where Li<sub>2</sub>O gas condenses to liquids on the surfaces of LLZO grains to promote the solid material transport.<sup>[49]</sup>



### 3. Solid Electrolyte/CAM Interface during Processing

Due to their rigid nature, sintering is generally required to establish intimate contact between the garnet-type SEs and CAMs.<sup>[55]</sup> Therefore, understanding the chemical stability and thermomechanical compatibility between these materials at elevated temperatures is essential.

#### 3.1. Diffusion and Phase Formation during Sintering

The thermodynamic stability of combinations of LLZO and various CAM phases has been studied both theoretically using DFT calculations<sup>[56]</sup> and experimentally (Table 1). Generally, the theoretical predictions on the stability trend of the CAM toward LLZO are consistent with experimental observations. For example, the driving force for LLZO reacting with LiCoO<sub>2</sub> (LCO) and LiNi<sub>1/3</sub>Mn<sub>1/3</sub>Co<sub>1/3</sub>O<sub>2</sub> (NMC) is calculated to be 1–2 meV per atom at 0 K, much lower than those for reactions with LiFePO<sub>4</sub> (LFP) (94 meV per atom) and LiMn<sub>2</sub>O<sub>4</sub> (LMO) (63 meV per atom),<sup>[56a–c]</sup> indicating that the interfaces of LLZO with LMO and LFP CAMs are less stable than with LCO and NMC. In a notable experimental study,<sup>[57]</sup> Ren et al. used surface-sensitive techniques such as Raman spectroscopy and XPS to detect minor reactions between Ta-doped LLZO and LCO or NMC when the powder mixture was cosintered at/above 700 °C. In contrast, LMO and garnet decompose completely when cosintered above 500 °C forming various ternary La and Li metal oxides (La<sub>1-x</sub>MnO<sub>3</sub>, La<sub>2</sub>Zr<sub>2</sub>O<sub>7</sub>, Li<sub>2</sub>Mn<sub>2</sub>O<sub>3</sub>), and LFP and LLZO decompose when cosintered above 500 °C also forming various products (iron oxides, Li<sub>3</sub>PO<sub>4</sub>, La<sub>2</sub>Zr<sub>2</sub>O<sub>7</sub>). Miara et al.<sup>[56d]</sup> performed DFT calculations on Ta-doped LLZO and high-voltage spinel cathodes such as Li<sub>2</sub>NiMn<sub>3</sub>O<sub>8</sub> (LNMO), Li<sub>2</sub>FeMn<sub>3</sub>O<sub>8</sub> (LFMO), and LiCoMnO<sub>4</sub> (LCMO) and found mixing energies between 25 and 60 meV per atom at 800 °C, suggesting reactions are favorable at high temperatures. These results corroborated their experimental observations that garnet/spinel powder mixtures decomposed even at 600 °C, with formation of such products as LiCoO<sub>2</sub>, LiFeO<sub>2</sub>, and NiO in LCMO, LFMO and LNMO, respectively. The formation of LCO as a stable product is consistent with previous studies, further suggesting that LCO is more stable for a co-sintered CAM than spinels when used with LLZO. With regard to the reactions initiated by Li loss, elevated temperatures above 1000 °C have been shown to induce Li loss in LLZO,<sup>[58]</sup> leading to the formation of resistive phases such as La<sub>2</sub>Zr<sub>2</sub>O<sub>7</sub> and La<sub>2</sub>O<sub>3</sub>. These decomposition products were also computationally predicted to form when LLZO is in contact with delithiated LCO (Li<sub>0.5</sub>CoO<sub>2</sub>),<sup>[56a]</sup> suggesting that minimizing Li loss from LLZO is critical in preventing the formation of resistive interfaces.

To date, LCO has been indicated as the most thermally stable CAM to cosinter with cubic LLZO. Generally, the intrinsic reaction between LCO and cubic LLZO relies on the cross diffusion of Co into LLZO and La/Zr into LCO (e.g., Figure 3a). Though this reaction can be visually distinguished by the color change of the garnet, i.e., from white to blue or green (Figure 3b),<sup>[57,60]</sup> it is superficial and sluggish/self-limiting within the temperature range associated with co-sintering of LCO and LLZO. The reaction can only be identified by surface/interface-sensitive

characterization techniques such as Raman spectroscopy and XPS,<sup>[57]</sup> TEM-EDS<sup>[60]</sup> and TOF-SIMS<sup>[62]</sup> after treatment at lower temperatures, e.g., 700 °C. Even upon sintering at 900 °C for 10 h<sup>[57]</sup> or 1050 °C for 2 h,<sup>[72]</sup> no impurity phases were detected by XRD. Wakasugi et al.<sup>[63]</sup> found that XRD showed no change in the lattice parameter for both LCO and Al-LLZO after the powder mixture was annealed up to 800 °C (Figure 3c), and the electrochemical performance of LCO showed no essential difference compared to nonannealed LCO in an organic electrolyte, suggesting no change of the bulk structure of the materials.

However, while a general trend of the chemical compatibility between LCO and LLZO is outlined above, reports differ on the specific reaction products and the reaction onset temperature (Table 1). For example, Park et al.<sup>[62]</sup> observed that the major resistive phase formed by annealing powder mixtures of LCO and Al-doped LLZO at 700 °C was the tetragonal LLZO phase, which was created by diffusion of the Al dopant from Al-LLZO into LCO (Figure 3d). Zhang et al.<sup>[56e]</sup> detected significant amounts of La<sub>2</sub>Zr<sub>2</sub>O<sub>7</sub> and LaCoO<sub>3</sub> by XRD in the powder mixture of LCO and Ta-LLZO after sintering at 600 °C. Using Al-doped LLZO and LCO thin films, Vardar et al.<sup>[64]</sup> found interdiffusion of Co and La and structural changes at the interface started at temperatures as low as 300 °C, forming LaCoO<sub>3</sub>, La<sub>2</sub>Zr<sub>2</sub>O<sub>7</sub> and Li<sub>2</sub>CO<sub>3</sub> at 500 °C as identified by synchrotron XRD and XAS (Figure 3e). Computational models have helped to elucidate the nature of the LLZO/LCO interface, where previous studies have mostly focused on constructing interface models based on specific orientations of the solids, notably the low-energy surfaces. For example, Jand and Kaghazchi<sup>[73]</sup> reported a DFT evaluation of the electronic and atomic structure of the cubic-LLZO/LCO interface based on the LLZO(001) and LCO(10-14) orientations. It was concluded that Li ion accumulation at these interfaces is energetically favorable, and that large biaxial compressive strain associated with lattice mismatch between the electrolyte and cathode led to reconstruction of the LLZO surface. These models indicate the cross diffusion of Co into LLZO and La/Zr into LCO. To the contrary, DFT calculations of the LCO(104)/LLZO(001) interface by Okuno et al.<sup>[56f]</sup> showed that all cation exchanges between LCO and LLZO were endothermic, indicating a thermodynamically stable interface.

Though further investigations are needed to clarify the reasons behind these various discrepancies, insights can still be gained by analyzing the literature experimental results and identification of subtle differences in sample compositions and processing conditions. In the study by Park et al.,<sup>[62]</sup> the formation of tetragonal LLZO phase was caused by the loss of the cubic-phase-stabilizing element, aluminum, a side reaction that was essentially independent to the intrinsic reaction between LCO and LLZO. Putting aside this side reaction, the elemental interdiffusion between LCO and LLZO was still minor as confirmed by TOF-SIMS, a result consistent with the general trend summarized above. In the studies by Zhang et al.<sup>[56e]</sup> and Vardar et al.,<sup>[64]</sup> the lower onset temperature for the reaction between LCO and LLZO compared to 700 °C reported by Ren et al.<sup>[57]</sup> and other researchers suggested a higher reactivity. Note that the powder mixture in Zhang's work was prepared by vigorous ball milling, which may have changed the surface structure of the LCO and LLZO particles and consequently caused the

**Table 1.** Summary of experimental investigations on the thermal stability of garnet-type SEs and cathode active materials.

Cathode active material (CAM)	Garnet composition	Interface formation method	Onset reaction temperature	Detection method	Reaction products (secondary phases)	Refs.
LiCoO <sub>2</sub>	Li <sub>6</sub> BaLa <sub>2</sub> Ta <sub>2</sub> O <sub>12</sub>	Powder mixing	Stable up to 900 °C	XRD	Not detected	[59]
LiNiO <sub>2</sub>			400–600 °C		La <sub>2</sub> LiTaO <sub>6</sub> , La <sub>2</sub> O <sub>3</sub> , Ta <sub>2</sub> O <sub>5</sub> , Li <sub>1-x</sub> NiO <sub>2-δ</sub>	
LiMn <sub>2</sub> O <sub>4</sub>					La <sub>2</sub> LiTaO <sub>6</sub>	
Li <sub>2</sub> MMn <sub>3</sub> O <sub>8</sub> (M = Fe, Co)					La <sub>2</sub> LiTaO <sub>6</sub>	
LiCoO <sub>2</sub>	Li <sub>7</sub> La <sub>3</sub> Zr <sub>2</sub> O <sub>12</sub>	PLD cathode thin film on garnet pellet	700 °C <sup>a)</sup>	TEM/EDS/NBD	La <sub>2</sub> CoO <sub>4</sub>	[60]
LiCoO <sub>2</sub>	Li <sub>6.75</sub> La <sub>3</sub> Zr <sub>1.75</sub> Nb <sub>0.25</sub> O <sub>12</sub>	PLD cathode thin film on garnet pellet	Stable at 600 °C <sup>a)</sup>	SEM/EDS mapping	Not detected	[43a]
LiCoO <sub>2</sub>	Al <sub>2</sub> O <sub>3</sub> -added Li <sub>7</sub> La <sub>3</sub> Zr <sub>2</sub> O <sub>12</sub>	Sputtered cathode thin film on garnet pellet	Stable at 500 °C <sup>a)</sup>	XRD, Raman	Not detected	[61]
LiCoO <sub>2</sub>	Li <sub>6.75</sub> La <sub>3</sub> Zr <sub>1.75</sub> Ta <sub>0.25</sub> O <sub>12</sub>	Powder mixing	600–700 °C	XRD, optical microscopy, Raman, XPS	LaCoO <sub>3</sub>	[57]
Li(NiCoMn) <sub>1/3</sub> O <sub>2</sub>					LaCo <sub>1-x</sub> Mn <sub>x</sub> O <sub>3</sub> (x < 0.4)	
LiMn <sub>2</sub> O <sub>4</sub>			400–500 °C	XRD	Li <sub>0.89</sub> Mn <sub>1.78</sub> O <sub>4</sub> , Li <sub>2</sub> MnO <sub>3</sub> , La <sub>x</sub> Zr <sub>1-x</sub> O <sub>2-x/2</sub> , La <sub>1-x</sub> MnO <sub>3 ± δ</sub> , La <sub>2</sub> Zr <sub>2</sub> O <sub>7</sub>	
LiFePO <sub>4</sub>					Li <sub>3</sub> PO <sub>4</sub> , La <sub>2</sub> Zr <sub>2</sub> O <sub>7</sub> , Fe, La <sub>x</sub> Zr <sub>1-x</sub> O <sub>2-x/2</sub>	
LiCoO <sub>2</sub>	Al-doped Li <sub>7</sub> La <sub>3</sub> Zr <sub>2</sub> O <sub>12</sub>	Powder mixing or cathode powder on garnet pellet	700 °C <sup>a)</sup>	XRD, ToF-SIMS, TEM/EDS mapping, electrochemical (de)lithiation	Tetragonal Li <sub>7</sub> La <sub>3</sub> Zr <sub>2</sub> O <sub>12</sub> , interdiffusion of Al, Co, La and Zr	[62]
LiCoO <sub>2</sub>	Li <sub>6.25</sub> Al <sub>0.25</sub> La <sub>3</sub> Zr <sub>2</sub> O <sub>12</sub>	Powder mixing	Stable up to 800 °C	XRD, electrochemical (de)lithiation	Not detected	[63]
LiMn <sub>2</sub> O <sub>4</sub>			500-600 °C		Li <sub>2</sub> MnO <sub>3</sub> , La <sub>2</sub> Zr <sub>2</sub> O <sub>7</sub> , LaMn <sub>0.8</sub> O <sub>3</sub>	
LiFePO <sub>4</sub>			300-400 °C		Li <sub>3</sub> PO <sub>4</sub> , La <sub>2</sub> Zr <sub>2</sub> O <sub>7</sub> , Fe, LaPO <sub>3</sub>	
LiCoO <sub>2</sub>	Al-doped Li <sub>7</sub> La <sub>3</sub> Zr <sub>2</sub> O <sub>12</sub>	Sputtered cathode thin film on garnet pellet	<300 °C	XRD, SEM, XRR, TEM, XPS, SIMS, EDS, HAXPES, XAS, EIS	LaCoO <sub>3</sub> , La <sub>2</sub> Zr <sub>2</sub> O <sub>7</sub> , Li <sub>2</sub> CO <sub>3</sub>	[64]
LiNi <sub>0.6</sub> Co <sub>0.2</sub> Mn <sub>0.2</sub> O <sub>2</sub>	Al-doped Li <sub>7</sub> La <sub>3</sub> Zr <sub>2</sub> O <sub>12</sub>	Sputtered cathode thin film on garnet pellet	500 °C	XANES, EXAFS, XRD, EIS	La(Ni,Co)O <sub>3</sub> , La <sub>2</sub> Zr <sub>2</sub> O <sub>7</sub> , Li <sub>2</sub> CO <sub>3</sub>	[65]
LiNi <sub>0.6</sub> Co <sub>0.2</sub> Mn <sub>0.2</sub> O <sub>2</sub>	Al-doped Li <sub>7</sub> La <sub>3</sub> Zr <sub>2</sub> O <sub>12</sub>	Sputtered cathode thin film on garnet pellet	Stable up to 700 °C in oxygen	XAS, XRD, EIS	Not detected	[66]
LiCoO <sub>2</sub>	Li <sub>6.75</sub> La <sub>3</sub> Zr <sub>1.75</sub> Ta <sub>0.25</sub> O <sub>12</sub>	Powder mixing by ball milling	500–600 °C	XRD	La <sub>2</sub> Zr <sub>2</sub> O <sub>7</sub>	[56e]
Li(NiCoMn) <sub>1/3</sub> O <sub>2</sub>					La <sub>2</sub> Zr <sub>2</sub> O <sub>7</sub> , LaNiO <sub>3</sub>	
LiNi <sub>0.6</sub> Co <sub>0.2</sub> Mn <sub>0.2</sub> O <sub>2</sub>	Li <sub>6.4</sub> La <sub>3</sub> Zr <sub>1.4</sub> Ta <sub>0.6</sub> O <sub>12</sub>	Powder mixing	700–750 °C	In situ HT-XRD	LaNi <sub>0.5</sub> Mn <sub>0.5</sub> O <sub>3</sub>	[67]
LiCoO <sub>2</sub>	Li <sub>6.25</sub> Ga <sub>0.25</sub> La <sub>3</sub> Zr <sub>2</sub> O <sub>12</sub>	Sputtered garnet-cathode thin film stack	700 °C	XRD	La <sub>2</sub> Zr <sub>2</sub> O <sub>7</sub>	[68]
LiCoO <sub>2</sub>	Li <sub>7</sub> La <sub>2.75</sub> Ca <sub>0.25</sub> Zr <sub>1.75</sub> Ta <sub>0.25</sub> O <sub>12</sub>	Sputter cathode thin film on garnet pellet	800 °C	XRD, ToF-SIMS	Tetragonal Li <sub>7</sub> La <sub>3</sub> Zr <sub>2</sub> O <sub>12</sub>	[69]
Li <sub>2</sub> CoMn <sub>3</sub> O <sub>8</sub>	Li <sub>6</sub> La <sub>3</sub> Nb <sub>1.5</sub> Y <sub>0.5</sub> O <sub>12</sub>	Powder mixing	400–600 °C	XRD	LiLaNb <sub>2</sub> O <sub>7</sub> , LiLa <sub>2</sub> NbO <sub>6</sub>	[70]
Li <sub>2</sub> FeMn <sub>3</sub> O <sub>8</sub>						
Li <sub>2</sub> NiMn <sub>3</sub> O <sub>8</sub>	Li <sub>6.6</sub> La <sub>3</sub> Zr <sub>1.6</sub> Ta <sub>0.4</sub> O <sub>12</sub>	Powder mixing	400–600 °C	XRD, TG/DTA	Li <sub>2</sub> MnO <sub>3</sub> , La <sub>2</sub> Zr <sub>2</sub> O <sub>7</sub> , LaMnO <sub>3</sub> , NiO	[56d] <sup>b)</sup>
Li <sub>2</sub> FeMn <sub>3</sub> O <sub>8</sub>					Li <sub>2</sub> MnO <sub>3</sub> , La <sub>2</sub> Zr <sub>2</sub> O <sub>7</sub> , LaMnO <sub>3</sub> , LiFe <sub>5</sub> O <sub>8</sub> , LiFeO <sub>2</sub>	
LiCoMnO <sub>4</sub>					Li <sub>2</sub> MnO <sub>3</sub> , La <sub>2</sub> Zr <sub>2</sub> O <sub>7</sub> , LiCoO <sub>2</sub>	
LiCoMnO <sub>4</sub>	Li <sub>5</sub> La <sub>3</sub> Ta <sub>2</sub> O <sub>12</sub>	Powder mixing	600–650 °C	XRD	Li <sub>2</sub> MnO <sub>3</sub>	[71a]
LiCoO <sub>4</sub>	Tetragonal Li <sub>7</sub> La <sub>3</sub> Zr <sub>2</sub> O <sub>12</sub>	Powder mixing	600 °C	XRD	La <sub>2</sub> Li <sub>0.5</sub> Co <sub>0.5</sub> O <sub>4</sub>	[71b]

<sup>a)</sup>The only temperature used in the study; <sup>b)</sup>Only the reaction products after annealing at 800 °C are shown here. The reaction products after annealing at 600 °C are secondary garnet phases and Li<sub>2</sub>MnO<sub>3</sub> for all three cathode active materials.



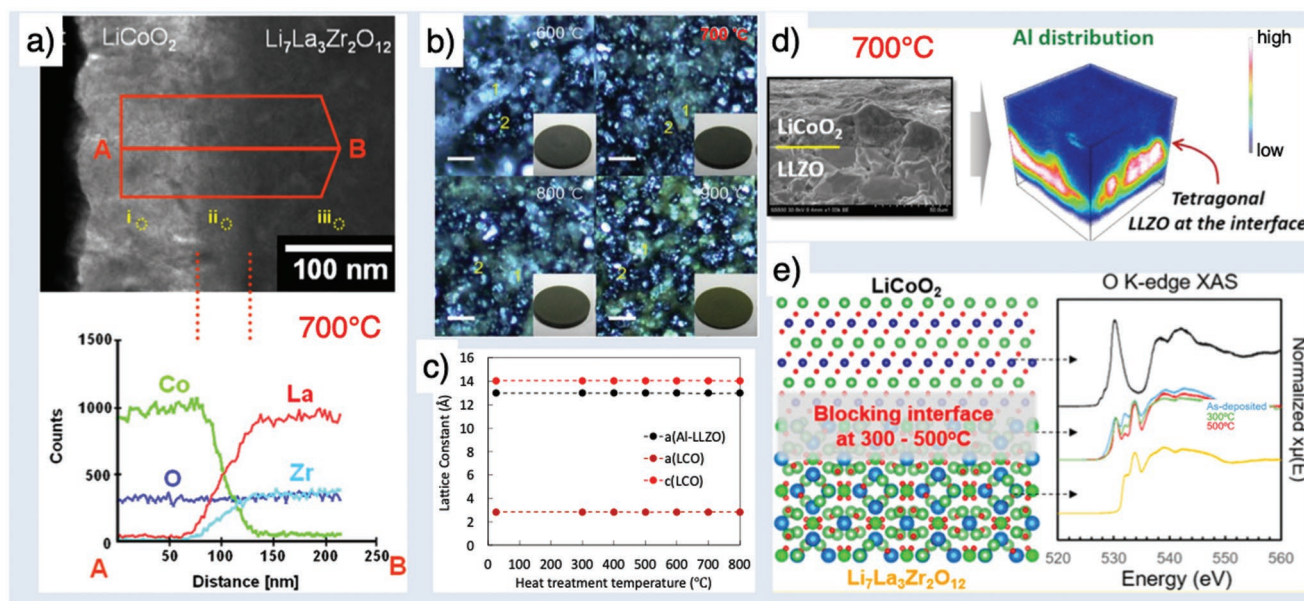


**Figure 3.** a) Cross-sectional TEM image of an LLZO/LCO thin film interface and the EDS line profile obtained from the region indicated by the red arrow in the direction A–B. The broken red lines indicate the reaction layer at the LLZO/LCO interface. Reproduced with permission.<sup>[60]</sup> Copyright 2011, Elsevier. b) Optical micrographs and photos (inset) of LLZTO(1)+LCO(2) powder mixture pellets annealed at different temperatures. Reproduced with permission.<sup>[57]</sup> Copyright 2011, Elsevier. (c) Variation of the lattice constants of Al-LLZO and LCO in the powder mixtures after annealing at different temperatures, plotted based on the data in Table 1 of the reference.<sup>[63]</sup> d) TOF-SIMS-enabled 3D Al elemental mapping of the 700 °C annealed LCO/LLZO interface that is shown in the SEM image. Reproduced with permission.<sup>[62]</sup> Copyright 2016, American Chemical Society. (e) Illustration of the crystal structures in the vicinity of the LCO/LLZO interface (left) and the corresponding O K-edge X-ray absorption spectroscopy data (partial fluorescence yield mode) for LLZO, LCO, and 60 nm thick LCO film on LLZO in the as-deposited state and after annealing at 300 °C and 500 °C (right). Reproduced with permission.<sup>[64]</sup> Copyright 2018, American Chemical Society.

higher reactivity. Ball-milling has recently been reported to be detrimental to the layered structure of NMC442.<sup>[74]</sup> Moreover, the reduced particle size and increased contact area between LCO and LLZO after ball milling could also amplify the reaction by generating more superficial reaction products. In Vardar's work,<sup>[64]</sup> the as-deposited LCO at room temperature showed low crystallinity in TEM/SAED analyses, which could also exhibit higher reactivity with LLZO similar to the LCO particles with mechanically damaged surfaces. Park et al.<sup>[62]</sup> demonstrated that in situ synthesis of LCO via the solid-state reaction of Li<sub>2</sub>CO<sub>3</sub> and cobalt acetate on the LLZO surface could more easily degrade the LCO/LLZO interface compared to co-sintering with crystalline LCO. The higher reactivity between LCO and LLZO was also observed in other studies of in situ forming LLZO on LCO.<sup>[72,75]</sup> Uhlenbruck et al.<sup>[72]</sup> investigated the interaction between LCO and in situ formed Ta-LLZO using sputtering or water-based microemulsion mediated synthesis. Their results generally suggest that a higher apparent reactivity between LCO and LLZO is due to premature lithium loss during LLZO formation, either via evaporation or diffusion into the substrate. In either case, the resulting lithium loss would change the stoichiometry of the reactants, driving the reaction to form other competing phases such as La<sub>2</sub>Zr<sub>2</sub>O<sub>7</sub> and LaCoO<sub>3</sub>. Sputtering species or chemical precursors are also known to have higher kinetic energy or reactivity. These species and precursors enable the formation of targeted phases at lower temperature, but may also be more affected by the thermodynamic stabilities of competing phases and instead form resistive phases. It is interesting

to note that Li<sub>2</sub>CO<sub>3</sub>, a form of Li loss from the bulk phase, was observed to form at the LCO/LLZO interface prior the high-temperature treatment in the studies by Park et al.,<sup>[62]</sup> Zhang et al.,<sup>[56e]</sup> and Vardar et al.<sup>[64]</sup> Consequently, La<sub>2</sub>Zr<sub>2</sub>O<sub>7</sub> and LaCoO<sub>3</sub> were detected as the main reaction products in these studies. The results obtained in these studies corroborate the work by Uhlenbruck et al. and show that the higher reactivity between LCO and LLZO is directly related to the higher interfacial energy.

Indeed, if the surface energy of the precursors for synthesizing the LCO/LLZO interface is reduced, less reaction would occur. Wakayama and Kawai<sup>[76]</sup> successfully synthesized an LCO/LLZO composite with nanoscale microstructure using a self-assembled block copolymer structure as a template. The composite with LCO content of 90% and above exhibited no impurities in XRD and HR-TEM/EDS, indicating that reactions between the LCO and LLZO precursors condensed in different polymer blocks were suppressed. The SSBs with composite cathode containing 90% LCO and PEO-based electrolyte operated at 50 °C exhibited clear cathodic and anodic peaks in cyclic voltammograms and a near theoretical discharge capacity of 134 mAh g<sup>-1</sup> in the first cycle at 0.05 C with a 99% Coulombic efficiency for 20 cycles.<sup>[76a]</sup> Ren and Wachsman<sup>[69]</sup> demonstrated that a thin alumina interlayer can effectively prevent reaction between the sputtered LCO film and LLZO garnet. The alumina interlayer was believed to have reduced the interfacial energy as indicated by the change of the film growth mechanism upon interlayer insertion from interfacial energy dominated to volume strain energy dominated.

Given the numerous concerns over the use of cobalt, NMCs can drastically reduce cobalt use and facilitate higher energy densities than LCO, hence demonstrating its chemical compatibility with LLZO is of more practical interest. Yet this topic is poorly studied and is usually associated with comparison with LCO.<sup>[56e,g,57,65]</sup> As a layered structure analogous to LCO, NMC generally exhibits a similar reaction mechanism when interfacing with LLZO, except that the reaction product between NMC and LLZO could be La(Mn, Co)O<sub>3</sub>,<sup>[57]</sup> LaNiO<sub>3</sub>,<sup>[56e]</sup> or La(Ni, Co)O<sub>3</sub>.<sup>[65]</sup> DFT calculations of the NMC(10-10)/LLZO(100) interface by Zhang et al.<sup>[56e]</sup> with a considerable lattice mismatch of  $\approx 8.3\%$  revealed that the Ni-La/Li (in LiO<sub>6</sub>) exchange near the interface were favorable, while the Mn/Co-La/Li exchange is much less likely. However, the specific compound has yet to be directly confirmed because of the limitations of solid/solid interface analysis (Table 1). Besides the unexplained reaction products, there are also differences in reactivity between NMC and LLZO in the published reports, with discrepancies likely having similar causes to the reported discrepancies in reactivity between LCO and LLZO. In addition, there is also disagreement in the same reports as to whether NMC or LCO has higher reactivity with LLZO. For example, studies by Ren et al.<sup>[57]</sup> and Zhang et al.<sup>[56e]</sup> on powder mixtures of NMC111 and Ta-LLZO suggested a slightly lower NMC stability than LCO. Conversely, the study by Yildiz's group on in-situ formed NMC622 thin films on Al-LLZO found a distinctly higher NMC stability than LCO based on the reaction onset temperature.<sup>[64,65]</sup> Clearly, more experimental work is needed to elucidate the discrepancy. A more recent study by Yildiz's group<sup>[66]</sup> on the NMC622/Al-LLZO system found that the annealing atmosphere could be a factor affecting the thermal stability between NMC622 and Al-LLZO, with O<sub>2</sub> being most favorable for achieving high stability, followed by N<sub>2</sub>, while CO<sub>2</sub> and H<sub>2</sub>O should be avoided. Besides the effect of the fabrication approach used to create the electrode/electrolyte interface, another potential focus could be the effects of composition, i.e., ratio of transition metals (TMs) in NMC and dopant in LLZO, on interface reactivity. Additionally, mismatch in the coefficients of thermal expansion (CTE) between the cathode and electrolyte materials will induce interface strain during co-sintering, which may also play a role in the reactivity.<sup>[73]</sup>

The disagreement on the reaction products and the onset temperature between different studies suggest that the practical stability between CAMs and LLZO SEs depends on the specific processing conditions and thus cannot be accurately predicted solely by thermodynamic calculations; kinetics studies are therefore necessary. Current computational models do not typically incorporate the interdiffusion of ions and formation of the passivation layer between cathode and LLZO at high temperatures. During co-sintering, to capture the necking, void removal and densification of the cathode composites, detailed phase field based models are needed that take into account the bulk, grain-boundary and surface diffusion.<sup>[77]</sup> Different diffusion coefficients are needed to understand homogeneous and heterogeneous reactions at interfaces, which should also depend on the interface energy between the CAM and LLZO. GB mobility must also be modeled to capture grain growth phenomena, which is influenced by the presence of dissimilar phases.<sup>[78]</sup> The relative location of the cathode and LLZO particles and their

size distribution can influence contact at the CAM/SE interface.<sup>[33,79]</sup> Simulation of the interdiffusion process at elevated temperatures also requires prediction of the ionic mobility as a function of the Gibbs free energy of the mixture, defined as a combination of the ideal and non-ideal interactions between the CAM and SE.<sup>[80]</sup>

### 3.2. Mechanical Stability during Sintering and Cooling

As mentioned in Section 3.1, the high-temperature cosintering process will lead to interfacial strains due to the CTE mismatch of the CAM and LLZO particles.<sup>[81]</sup> More specifically, the CTE mismatch leads to differential volume change and subsequent evolution of interfacial stress. During the heating ramp of the cosintering process, the developed interfacial stresses dissipate because of the viscoplastic deformation and annealing that occur at high temperature. Thermomechanical equilibrium can be expected at the end of the high temperature cosintering step just prior to the cooling process. However, upon cooling interfacial stresses can arise.<sup>[82]</sup> These thermal stresses either remain as residual stresses in the composite cathode or dissipate through the formation of interfacial cracks when the strain energy exceeds the fracture threshold of the interface. Such cracks at the interface between the CAM and LLZO can lead to a reduction in electrochemically active surface area and increased interfacial resistance. Hence, adoption of CAMs that demonstrate CTE similar to LLZO can help minimize stress generation during the cooling process.<sup>[83]</sup>

Prediction of stresses in composite LLZO cathodes requires accurate estimation of CTEs for both CAM and LLZO. In computational modeling, there exist methodologies to estimate the CTE of bulk materials using DFT based atomistic simulation techniques.<sup>[84]</sup> The CTE for LCO-type CAMs, as predicted by atomistic simulations, demonstrates a strong dependence on the temperature of operation as well as the amount of Li present within the layered CAM phase.<sup>[85]</sup> However, such low length scale approaches have not yet been adopted for estimating the CTE for LLZO SEs. Typically, the CTE is measured at the atomic scale using XRD as a function of temperature and dilatometry, which measures macroscale deformation versus temperature. The two techniques are complementary, especially when measuring anisotropic crystal symmetries. A few studies using XRD<sup>[86]</sup> have determined the CTE of LLZO to be approximately  $1.5 \times 10^{-5} \text{ K}^{-1}$ . Similarly, there have been reports that include the CTE of active materials such as LCO, NMC, and LMNO.<sup>[81,87]</sup> There is some disagreement between CTEs estimated through XRD and dilatometry, which could be associated with anisotropy, especially for LCO and NMC. In general, the CTEs of LCO and NMC are  $1.25 \times 10^{-5} \text{ K}^{-1}$  and  $1.3 \times 10^{-5} \text{ K}^{-1}$ , respectively.<sup>[81,82,86b,87a]</sup> Acknowledging that LCO and NMC are anisotropic and the CTEs measured through dilatometry are "effective" CTEs, there is a  $\approx 0.2 \times 10^{-5} \text{ K}^{-1}$  difference compared to LLZO.

Owing to the relatively high elastic modulus of the above-mentioned materials ( $\approx 150\text{--}185 \text{ GPa}$ ), combined with the relatively high processing temperature ( $>1000 \text{ }^\circ\text{C}$ ),<sup>[83]</sup> relatively large thermal mismatch stresses upon cooling after densification are expected. Yu et al.<sup>[82]</sup> analyzed the effect of thermal mismatch

stress during the cooling process on the mechanical stresses of LCO–LLZO and NMC–LLZO composites using continuum level simulations and calculated that stresses approaching 1 GPa were generated. Appropriate CAM and SE particle sizes were considered for the accurate estimation of residual interfacial stresses during the cooling process. It is known that the fracture strength of LLZO is approximately 100–150 MPa,<sup>[88]</sup> thus fracture of LLZO composite electrodes is possible during the cooling.

If GBs can be engineered to enable viscoelastic/viscoplastic flow, fracture could be avoided. This approach is shared with efforts to engineer microstructures to mitigate stresses associated with the expansion and contraction of active particles during cycling. There is clear motivation to engineer electrode/electrolyte interfaces to maintain stress below the material fracture stresses during processing and cycling. Moreover, systematic multiscale studies for estimating the CTE, level of interfacial stress generation, and the extent of fracture evolution must be studied to allow numerical optimization of cathode microstructures that will maximize cell performance.

Another mechanism that can lead to interfacial stresses during the sintering process is the molar volume mismatch between the pristine CAM/LLZO interface and the interface formed by the interdiffusion of ions, which has been sparsely studied so far.<sup>[89]</sup> It has been thoroughly argued that during the high-temperature sintering process, interdiffusion occurs between cathode and LLZO, which can lead to the formation of various reaction products.<sup>[56a]</sup> The molar volumes of the pristine CAM and LLZO SEs are generally different from the molar volumes of the reaction products.<sup>[90]</sup> For example,  $\text{La}_2\text{O}_3$  and  $\text{La}_2\text{Zr}_2\text{O}_7$  obtained through the decomposition of LLZO occupy a much smaller volume than the parent material. This mismatch in molar volume can lead to the formation of interfacial stresses.<sup>[82]</sup> Dissipation of some of these stresses is possible at higher temperatures due to the enhanced viscoplastic deformation and annealing processes. However, their actual influence on the interfacial stability will depend not only on the mismatch in molar volume, but also on the CTE of the reaction products as compared to the parent electrode and electrolyte materials, as all these phases experience thermal contraction during cooling.

### 3.3. Mitigating Interfacial Challenges during Processing

Given the inherent chemical instabilities of LLZO with commercial CAMs, methods are needed that enable sintering of the grains without the formation of resistive decomposition products and possible crack formation due to a mismatch in CTE of LLZO and CAMs. One such method is the use of a sintering additive (sintering aid) with reasonable Li-ion conductivity to lower the temperature to create CAM/LLZO interfaces. Sintering aids melt at high temperature and form a protective interphase between the CAM and LLZO, which blocks interdiffusion and improves interparticle contact. Sintering aids reported for this purpose include  $\text{Li}_3\text{BO}_3$  and  $\text{LiBO}_2$  that can effectively melt below 700 °C,<sup>[91]</sup>  $\text{Li}_2\text{SiO}_3$  that can be in situ synthesized by a low temperature liquid phase process,<sup>[92]</sup> and  $\text{Li}_3\text{PO}_4$  that can be in situ synthesized by calcination at

750 °C.<sup>[93]</sup> This method has shown some success in improving the active material utilization and rate capability of garnet SSBs with LCO and NMC as the only examples of CAMs investigated so far,<sup>[91–94]</sup> however, the performance required for commercial cells is still not attained. Han et al.<sup>[95]</sup> utilized the native formation of  $\text{Li}_2\text{CO}_3$  on the surface of LLZO and LCO with  $\text{Li}_3\text{BO}_3$  to create a more conformal coating of  $\text{Li}_{2.3-x}\text{C}_{0.7+x}\text{B}_{0.3-x}\text{O}_3$  (LCBO). Rather than causing sintering between LCO and LLZO, the LCBO melt densified the mixed cathode without direct contact between LCO and LLZO, preventing secondary phase formation. This method produced 20 μm thick cathode composites with an areal capacity of 0.1 mAh cm<sup>-2</sup> (or 106 mAh g<sup>-1</sup> in specific capacity) at 100 °C. However, since the measured ionic conductivity of LCBO in this study was still low, i.e.,  $\approx 10^{-5}$  S cm<sup>-1</sup> at 100 °C,<sup>[95]</sup> further increasing the cathode thickness did not increase the cell capacity due to cathode kinetic limitations. Interestingly, the capacity fade depended strongly on the operating temperature, with approximately 50% drop in capacity after 40 cycles for cells operated at 100 °C compared to merely 15% drop in capacity after 100 cycles for a cell operated at 25 °C. This suggests a strong electrochemo-mechanical effect and will be discussed in Section 4.

An alternative method used to reduce the interfacial resistivity is the incorporation of an interface layer into the SE/CAM interface, as will be discussed in Section 7.2.

In parallel, the sluggish reaction kinetics in LCO–LLZO mixtures, especially when using phase pure, crystalline materials, enabled the production of cathode composites consisting only of LLZO and LCO, without the use of sintering additives. First reported by Finsterbusch and Danner et al. in 2018, a relatively short 30 min sintering step at 1050 °C lead to relatively porous cathodes with approximately 80% of the theoretical value, but showed an exceptionally high areal capacity of 0.84 mAh cm<sup>-2</sup> in the first discharge cycle.<sup>[12]</sup> Even though the utilization was around 81% or 110 mAh g<sup>-1</sup>, the cell also required an operating temperature of 100 °C, which was most likely due to resistive secondary phases at the LCO–LLZO interface, as the applied 3D continuum model ruled out the ionic conductivity of the LLZO as origin of the low room temperature performance. Later, the ASR of the LLZO–LCO interface could be reduced further by tailoring the materials, especially the phase purity and crystallinity of the used LLZO. The resulting cell showed twice the areal capacity (1.62 mAh cm<sup>-2</sup>) at 50 °C, while the utilization stayed at approximately 80% (113 mAh g<sup>-1</sup>).<sup>[83]</sup> Unfortunately, both cell types suffered from a high cycling degradation of about 50–60% after 50 cycles. Similar to mechanical stresses from the sintering described above, mechanical failure due to the chemomechanical stresses during cycling was identified as origin of this rather large degradation (see Section 4.2).

To obtain an interface free of secondary phases, advanced sintering methods were explored to achieve densification below 700 °C without the need of additives. Using mechanical pressure and fast Joule heating, the “field assisted sintering technique” (FAST/SPS) was able to produce LCO–LLZO cathode composites as well as cathode composite/LLZO separator half cells with up to 95% theoretical density after only 10 min dwell time at 650 °C to 700 °C in Ar.<sup>[11,96]</sup> Due to the sluggish reactions described above, the very short processing



time with heating rates up to  $100 \text{ K min}^{-1}$  resulted in interfaces that were virtually free of secondary phases, as verified via TEM. However, the cells still showed a rather high interface resistance between LCO and LLZO, stemming from amorphization of the particle surface during powder preparation or the interfaces during processing. A second, short annealing in air improved the crystallinity and thus the ASR, enabling a rather high areal capacity of up to  $1.2 \text{ mAh cm}^{-2}$  ( $75 \text{ mAh g}^{-1}$ ) at an operating temperature of  $80 \text{ }^\circ\text{C}$ .

However, even though clean interfaces in an almost fully dense mixed LLZO–LCO cathode composite were achieved via FAST/SPS, the areal capacity could not be increased above  $2 \text{ mAh cm}^{-2}$  due to the limitation imposed by the Li-ion pathways in the 3D structured electrode (see Section 4.3). Even more surprisingly, the dense cathode composite still showed a fast degradation of cell performance, often losing up to 10% capacity per cycle. Since cracking of the cathode, as observed for free sintered cathodes with 80% density, was ruled out as cause for the degradation, the results provided the first evidence of an electrochemical degradation of the LCO–LLZO interface due to cell operation and will be discussed in Section 4 in detail.

There does not exist any continuum level model that captures the interdiffusion of ions and formation of the passivation layers between CAM and LLZO at higher voltages. Research activities on LEs attempted to predict the formation of the resistive cathode electrolyte interphase (CEI) layer using cell level continuum models,<sup>[97]</sup> which can also be adapted for SEs with appropriate modifications. Experimental research, supported by atomistic calculations,<sup>[56b,98]</sup> have implemented interfacial protective layers, either in the form of sintering aids<sup>[95,99]</sup> or externally applied coatings,<sup>[68]</sup> that can help to minimize the interdiffusion of ions between CAM and LLZO. However, mechanical degradation is still expected to occur even with the presently available coating layers, which can eventually be minimized by better design of the CAM/LLZO interphase material.

## 4. Solid Electrolyte/CAM Interfaces during Operation

Depending on the type of interface, current across it can lead to kinetically driven solid-state reactions and degradation—adding to thermodynamically driven reactions described in the previous sections. These electrochemical reactions are spontaneous, once the transport properties of the neighboring phases differ—examples can be found in the literature.<sup>[100]</sup> In the following sections, we consider different types of interfaces and discuss their behavior during operation, i.e., during current load.

### 4.1. Lithium Transfer across the LLZO/CAM Interface

The interfacial kinetics of the LLZO/CAM interface is poorly understood and in general the properties of chemically and structurally defined interfaces are unknown due to the lack of suitable model systems. Moreover, the low thermal stability of the components during the required high temperature

treatment and instability towards high energy ion and electron beams prevent the analysis of ideal interfaces. For example, the charge transfer resistance for LCO/LLZO interfaces is experimentally observed to be in the range of  $1\text{--}5 \text{ k}\Omega \text{ cm}^2$ . This value strongly depends on the synthesis process and very likely includes contributions of processing-induced secondary phases and their interfaces as described in Section 3, implying that the resistance of a chemically and structurally well-defined LCO/LLZO interface can be significantly lower. Clearly, the lack of experimental information requires greater systematic studies of oxide SE/CAM interfaces.

Few theoretical studies on LLZO/CAM interfaces address the effect of SCLs on the Li-ion conductivity, similar to the LLZO/LLZO homointerfaces described in Section 2.1.5. De Klerk et al.<sup>[101]</sup> calculated the interface resistances due to SCLs for different SEs on electrodes including LLZO on LCO, and found that the interface resistances are negligible assuming no kinetic term at the interface and no electron accumulation in the cathode. Furthermore, they found that a Coulombic interaction term may significantly reduce the SCL.

Theoretical calculations imply that the formation of SCLs can be accompanied by the evolution of mechanical stress at the LLZO/CAM interface, which can be attributed to the following aspects: 1) SCLs consist of concentration gradients, and depending on their partial molar volume can significantly modify the atomic volume; 2) due to the relatively high elastic modulus of LLZO, small variations in atomic volume can lead to the generation of stresses in the range of hundreds MPa; 3) as the SCLs are not electrically neutral, the resulting strong electric field can lead to the evolution of a Lorentz force within the SCLs, which acts on the electrodes and electrolytes; and 4) these electric field-induced forces can also lead to stresses in the range of GPa. A more detailed discussion of the mechanical effects is provided in Section 4.2.2.

In contrast to LiPON electrolyte, where the cycling performance and interface evolution are well understood, very few data exist for LLZO/CAM interfaces. The high cycling stability of the LiPON/CAM interface is, however, encouraging and is one reason for the high expectations concerning the stability of the solid-solid interfaces in SSBs. Specifically, thin-film batteries with LiPON electrolyte and LCO or LNMO as single-phase cathode have demonstrated extremely high cycle life of up to 10000 cycles at 100% depth of discharge (DOD) with only 10% capacity loss,<sup>[102]</sup> far exceeding the cycling performance of classical organic LE-based Li-ion batteries, albeit with low areal loading and capacity.

As discussed in Section 3, the low thermodynamic stability of LLZO/CAM interfaces during processing has been an issue of major concern for the development of LLZO-based all-solid-state batteries. Three major causes for the high LLZO/CAM interface resistances can be discerned: 1) the direct reaction of the two materials, forming resistive or even ion blocking secondary phases during processing; 2) the loss of crystallinity and formation of interfacial regions with lower ionic conductivity, e.g. tetragonal LLZO due to diffusion of Al into LCO; and 3) artificially introduced secondary phases with low conductivity, e.g. sintering aids to lower the processing temperature (LCBO) or unsuitable powder preparation (e.g., air exposure prior to sintering). But even for well-defined, impurity-free LCO



and LLZO interfaces, severe degradation was observed during cycling, demonstrating the need to investigate the stability of the interfaces during operation.

#### 4.2. Electrochemical Stability of the Solid Electrolyte/CAM Interface

In general, while cycling layered oxide CAM particles in a rigid LLZO matrix, the experimentally observed capacity fade can be divided into two subdomains:<sup>[83,103]</sup> 1) the first charge/discharge cycle shows a large capacity fade in combination with a low Coulombic efficiency and 2) the subsequent cycles show a capacity fade at a slower, but substantial rate, while the Coulombic efficiency is rather high. For example, Tsai et al. reported the loss of most of the initial capacity (1.8 to 0.4 mAh cm<sup>-2</sup>) within 100 cycles at 50 μA cm<sup>-2</sup> for the LCO/LLZO electrodes fabricated via screen printing and conventional sintering of respective crystalline powders.<sup>[83]</sup> Much higher initial capacities and higher CAM loadings have been obtained for mixed cathodes fabricated via tape casting with optimized CAM distribution (gradient cathode composites) showing initial discharge capacities of 2.75 mAh cm<sup>-2</sup>, which drop to 1.3 mAh cm<sup>-2</sup> after only 10 cycles (see Figure 7d).<sup>[104]</sup> Although the residual capacity value after cycling the cathode tapes is still higher than that of the screen printed cathodes, the capacity fading in both cases is still unacceptably high and most likely due to the loss of mechanical integrity, which will be described in Section 4.2.2. In contrast, cathode composites

produced by the novel FAST/SPS method showed high density and no sign of mechanical degradation, excluding this failure mechanism, but also exhibited rather large capacity losses within the first 5 cycles, dropping from 1.2 to 0.8 mAh cm<sup>-2</sup> (Figure 4a).<sup>[105]</sup>

Although a complete spectrum of SE/CAM cathode degradation mechanisms during operation does not exist, the degradation processes can be divided into two major categories:

1. Electrochemical degradation: oxidation of the SE, CAM or both at higher voltages accompanied by an interdiffusion of metal ions;<sup>[106]</sup>
2. Mechanical degradation associated with CAM shrinkage/expansion during the delithiation/lithiation steps.<sup>[83,107]</sup>

The majority of reports indicate that the rapid capacity fade during the first charge/discharge step can be attributed to the electrochemical oxidation of the interface (often attributed to the oxidation of LLZO by the CAMs at higher voltages<sup>[56a,103]</sup>), whereas the slower subsequent decay is due to fatigue failure of the CAM/SE interface and loss of electrochemically active surface area. Thus, more detailed discussion of these processes is presented in Sections 4.2.1 and 4.2.2.

##### 4.2.1. Electrochemical Degradation

Among the processes that can occur at the LLZO/CAM interface during operation, the following reactions are envisioned: the electrochemical decomposition of individual LLZO or CAM

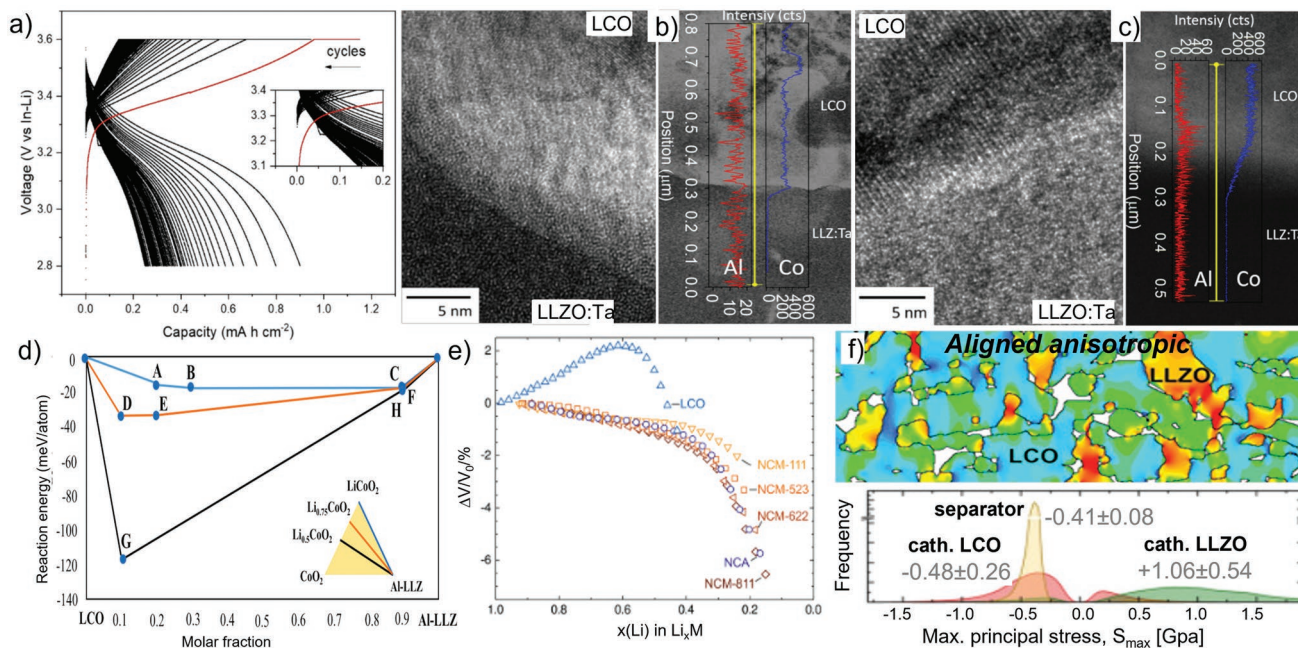


**Figure 4.** a) Galvanostatic charge/discharge curves (first 60 cycles) of an all inorganic cell made via FAST/SPS featuring a LCO+LLZO cathode composite|LLZO separator and Li metal anode, and TEM images with EDX profiles of the LCO/LLZO interface before cycling b) and after cycling c) showing the interfacial degradation. Reproduced with permission.<sup>[11]</sup> Copyright 2022, American Chemical Society. d) Pseudo-binary phase diagram of the possible decomposition products of LLZO for various degrees of lithiation in LCO (state of charge). Reproduced with permission.<sup>[11]</sup> Copyright 2022, American Chemical Society. e) Volume change as function of SOC for various cathode active materials; Reproduced with permission.<sup>[107]</sup> Royal Society of Chemistry. f) calculated stresses for the expected volume expansion of LCO in a cathode composite based on LLZO, taking the anisotropic expansion into account. Reproduced with permission.<sup>[108]</sup> Copyright 2022, Elsevier.

phases beyond their oxidation potential; the oxidation of LLZO by the CAM; simultaneous electrochemical decomposition of LLZO and CAM at higher voltages, or chemical reactions between the LLZO and CAM. Each of these processes can be accompanied by an interdiffusion of ions at the interface.

Initially, LLZO was thought to be stable up to 6 V,<sup>[52,109]</sup> which was mostly deduced from CV tests with blocking electrodes. In actual cells featuring LLZO as electrolyte, possible electrochemical degradation was typically buried under the chemical degradation, i.e., the secondary phase formation at the interface discussed above, resulting in large interface resistances. However, similar to the calculation of thermodynamic stability between LLZO and CAMs at different temperatures described in Section 3.1, the electrochemical stability of LLZO/CAM can be estimated in the same way. Ceder et al.<sup>[56c,110]</sup> reported the computational thermodynamic stability of the electrolyte/cathode interphase under an applied potential and suggested that, for LLZO, the LLZO/LCO interface is the most stable, showing only a small driving force for decomposition in the charged state.<sup>[56c]</sup> Okuno et al.<sup>[56f]</sup> reported a comparative analysis using DFT of the characteristics of sulfide SE ( $\text{Li}_3\text{PS}_4$ ) and oxide SE ( $\text{Li}_3\text{PO}_4$  and  $\text{Li}_7\text{La}_3\text{Zr}_2\text{O}_{12}$ ) interfaces with a typical oxide CAM (LCO). They considered the Li-vacancy formation associated with the Li chemical potential and the cation exchange related to the reaction layer formation. They found that—compared to the case of sulfide SE interfaces—the oxide SE interfaces have fewer Li sites with lower vacancy formation energy and are stable against the mutual cation exchange with the oxide cathode. These results indicate that the oxide SEs show less dynamical Li-ion depletion upon initial charging and less formation of a reaction layer compared to those of sulfide SEs. In all cases, the calculated stability was much lower than the one observed experimentally using blocking electrodes, typically in the 3.0–3.8 V range.<sup>[56a,c]</sup> Such atomistic simulations allude to the oxidation of LLZO and propensity for formation of an interphase layer between LCO and LLZO at operating potentials above 4.0 V.<sup>[56a]</sup> This is partially attributed to the delithiation of the LLZO by the highly delithiated CAM particles at higher voltages.

The first experimental proof was given by the Wagemaker group, using LLZO-C composites and showing an oxidative decomposition at 3.5 V versus  $\text{Li}^+/\text{Li}$ .<sup>[111]</sup> Their studies verified that the decomposition pathway determining the electrochemical stability window is mediated by a delithiated state of the LLZO, instead of a direct path to the decomposition products. Interestingly, this implies that intermediate products can contribute to the capacity of LLZO-based SSBs, which might explain the observed irreversible losses in the first cycle.

The first proof of electrochemical degradation in an LLZO/LCO composite cathode was provided by Ihrig et al.,<sup>[111]</sup> enabled by a highly dense cathode with secondary phase-free interfaces after FAST/SPS processing. Without the contribution of high impedance secondary phases and the high structural stability preventing mechanical failure, it was possible to clearly investigate the electrochemically induced degradation. Two main factors were identified: cation diffusion between LCO and LLZO, especially at high states of charge, and a loss of crystallinity for LLZO close to the interface. While Al diffused into LCO, Co was diffusing into LLZO, both aiding in the amorphization of LLZO. As the ionic conductivity of LLZO

is especially sensitive to changes in the crystal structure, this ultimately led to highly resistive interfacial layers and thus degradation of the cell performance (Figure 4a–d).<sup>[11]</sup>

Presently, continuum level modeling cannot capture the formation of the passivation layers during operation at high voltages. It would involve transfer of electrons and  $\text{Li}^+$  ions and could possibly be simulated using techniques reported by Newman and co-workers for capturing the evolution of solid electrolyte interphase (SEI) and metal oxide films on anode surfaces.<sup>[112]</sup> A smaller magnitude of lithium ionic conductivity through these interphase layers, and subsequent potential drop during operation, is the largest bottleneck associated with the formation of these cathode electrolyte interphases.<sup>[62,83]</sup> Application of protective interphase layers in between the CAM and LLZO is an effective pathway for minimizing the interdiffusion of ions during both high temperature cosintering as well as high voltage cycling.<sup>[56a,95,98]</sup>

#### 4.2.2. Mechanical Degradation

Mechanical degradation is a key issue in ceramic solid-state batteries. The CAM changes volume as function of state-of-charge, and this can cause high local stress.<sup>[107,113]</sup> Since the fracture strength of garnet oxides is  $>100$  MPa, the stress that evolves within the cathode composite during operation due to the volume changes of the CAM can eventually lead to mechanical failure of various interfaces. The resulting cracks can hinder the transport of Li ions in the bulk of LLZO by detaching one grain from the other, or reduce the electrochemically active surface area by delaminating the electrode from the LLZO electrolyte.

During charge–discharge operation of an oxide composite cathode there exists the possibility of fracture evolution at three different interfaces:<sup>[6e,114]</sup> 1) along or through the grain boundaries of LLZO; 2) along or through the grain boundaries within the CAM; and 3) at the LLZO/CAM heterointerface.

The fracture within grain boundaries of LLZO during the growth of Li dendrites on the anodes side has been briefly discussed in Section 2. Experimental studies reveal that rupture of LLZO pellets along the GB region is possible under tensile stresses in the range of hundreds of MPa.<sup>[21,88]</sup> Continuum and phase field-based computational modeling reveals that nucleation of lithium at the junction of GBs (or triple points) can create sufficient Poiseuille pressure, to cause fracture along the LLZO GBs.<sup>[34,115]</sup> Similar computational analysis has also revealed that increasing the elastic modulus of LLZO GBs, through some type of GB engineering techniques, can effectively help to minimize fracture within LLZO.<sup>[116]</sup>

Generation of lithiation/delithiation induced mechanical stress and subsequent evolution of cracks within oxide based CAM particles (LCO, NMC, LMO, NCA) have been studied in detail using both experimental and computational techniques.<sup>[114,117]</sup> The fracture strength of layered oxide CAM particles ranges around hundreds of MPa, which is similar in magnitude to that of the LLZO,<sup>[118]</sup> i.e., both the LLZO and oxide CAM exhibit typical ceramic mechanical behavior. FIB-SEM revealed that cracks evolve within the GBs of the CAM particles during operation, which becomes more prominent for larger secondary particles.<sup>[119]</sup> Computational modeling

reveals that along with the depth of charge/discharge, the rate also influences the extent of mechanical degradation within the CAM particles.<sup>[117,120]</sup> The impact of mechanical degradation on the increase in impedance and decay in cyclable capacity of the CAM particles is captured by mathematical models.<sup>[120]</sup> Note that most of these studies assumed battery operation with LEs, so far only one of them compared operation in LEs with SEs (though with sulfide SE).<sup>[121]</sup> There always exists a chance of inflow of liquid electrolytes through the surface connected cracks to the interior of the cathode; this positively affects the cell performance by increasing the electrochemically active surface area, but has a negative influence on the cell lifetime through the formation of detrimental surface layers.<sup>[114]</sup> Due to the nonconformability of the SEs, they cannot flow through the cracks on the surface of the CAM particles, and the mechanical degradation within the cathode negatively affects the internal diffusion of ions as well as leads to isolation of particles, with subsequent capacity fade.<sup>[122]</sup> An appropriate computational model needs to be developed that takes into account the ionic and electronic transport through these SE/CAM composites and study the influence of mechanical degradation within the cathode particles on the overall capacity fade. There is yet no experimental study that incorporates percolation theory and its influence on mechanical degradation. However, there are a growing number of detailed studies on ionic and electronic transport in SSB composite cathodes with sulfide SEs.<sup>[123]</sup>

The third kind of mechanical degradation observed within the CAM/LLZO composites is the formation and propagation of interfacial cracks between the CAM and SE.<sup>[99,103]</sup> Stresses evolve at the interface between layered oxide CAM particles and LLZO due to the mismatch in CTEs during cooling after the high temperature cosintering step,<sup>[82]</sup> or due to the shrinkage/expansion of the CAM during lithiation/delithiation.<sup>[108]</sup> Due to the larger elastic modulus of LLZO and layered oxide CAM particles,<sup>[87a,88]</sup> tensile stresses in the range of hundreds of MPa to a few GPa can be generated at the CAM/LLZO interface.<sup>[108,124]</sup> Whether such stresses lead to the evolution of interface cracks depends on the fracture toughness at the location in the cathode. Due to the difficulties associated with measuring the mechanical properties of the CAM/LLZO interface, no experimental technique has successfully estimated the fracture strength between the CAM and SE particles. Techniques such as nanoindentation can perhaps measure the mechanical properties of GBs.<sup>[125]</sup> By modeling the CAM/solid-electrolyte interface using cohesive zone methodology, continuum level analysis revealed that LLZO should delaminate from the CAM particles if the active materials shrink by more than 7.5% during operation.<sup>[126]</sup> Such a degradation was shown for LLZO/LCO based cells and unambiguously pinpointed the increase in ASR stemming from the electrodes, with the mixed cathode being the most likely origin.<sup>[83]</sup> As predicted by Koerver et al. (Figure 4e),<sup>[107]</sup> microcracks appeared in the mixed LLZO/LCO cathode as both trans-granular cracks in LCO and LLZO particles, especially close to macropores, and as cracks between LCO and LLZO particles.

Such microcracks can occur when the strain and stress induced by the volume change of LCO during cycling exceeds the threshold value. In addition, 3D microstructure resolved modeling for the above mentioned LLZO/LCO system was recently published by Mücke et al.<sup>[108]</sup> It was found that LLZO is subjected to significant tensile stresses, which may lead to

microcracking and ionic isolation of regions of the mixed cathode (Figure 4f). For LCO, the compressive stresses are similar to the flexural strength. Depending on the cell design and preferred crystallographic orientation, the stresses can also be reduced to values lower than the flexural strength of the cathode components. This again demonstrates the need for advanced fabrication techniques, as discussed in Section 3.3, that can achieve high density mixed cathodes while suppressing the formation of secondary phase. Furthermore, it has also been argued that electrochemical reaction between the CAM and SEs at higher potentials can lead to the formation of new species at the CAM/SE interface (see Section 4.2.1).<sup>[56a]</sup> The resulting mismatch in molar volume between these new phases and the pre-existing combination of CAM and SEs can lead to stress generation at the CAM/SE interface and can result in further mechanical degradation and interfacial delamination, which has already been demonstrated both computationally and experimentally for LCO and LiPON SEs.<sup>[89]</sup> Loss of contact between CAM and SE leads to a decrease in electrochemically active surface area, which can substantially increase the charge transfer resistance and cause voltage and capacity fade.<sup>[32]</sup>

Computational modeling of the interfacial delamination between the CAM and LLZO during charge/discharge reveals that the capacity fade cause by mechanical detachment persists for ten cycles without showing saturation.<sup>[127]</sup> Theoretical analysis also revealed that LLZO with smaller grains, softer electrolytes (e.g., sulfides), or better interfacial adhesion between the CAM and SE may help to minimize interfacial de-bonding or fracture and subsequent capacity fade.<sup>[127]</sup> Thus, softer electrolytes may be able to accommodate a greater change in the cathode volume to reduce interfacial delamination (see Section 5).<sup>[126,127]</sup>

## 5. Contrast with Soft and Glassy Solid Electrolytes

### 5.1. Grain Boundaries

Within this review, soft and glassy SEs such as sulfides (thiophosphates) or salt-in-polymer electrolytes are distinguished from oxide-type SEs based on their electrochemical and mechanical properties.<sup>[6k]</sup> The most consequential advantage of soft and glassy SEs is that powders can be densified at room temperature or below 100 °C to form a low resistance pellets, sheets, or films. This enables the use of conventional casting and calendaring techniques used for Li-ion batteries.<sup>[128]</sup> Scalable tape casting and calendaring processes have also been successfully applied to oxides such as LLZO,<sup>[4,129]</sup> but this requires an additional sintering step at high temperature (>500 °C) for grain-to-grain ion transfer to occur. The second difference between soft and glassy SEs and oxide SE is that unlike sintered oxides, sulfide and polymer SEs show only one frequency-dependent transport process (in a Nyquist plot), even at low temperature. In contrast to oxides, grain and GB contributions cannot be clearly distinguished in impedance measurement. It is commonly assumed that there is no significant GB resistance contribution in thiophosphates or polymer solid electrolytes as shown for  $\beta$ -Li<sub>3</sub>PS<sub>4</sub> with pulsed field gradient NMR.<sup>[130]</sup> In contrast to this assumption, in a recent combined



**Table 2.** List of mechanical properties as well as ionic conductivity of selected battery materials.

Material	Young's modulus E[GPa]	Bulk modulus K [GPa]	Shear modulus S [GPa]	Conductivity $\sigma_{\text{ion}}$ [S cm <sup>-1</sup> ]	Refs.
NCM111	199	78	132	–	[81]
LLZO:Al	163	65	112	$\approx 10^{-4}$	[136]
Li <sub>6</sub> PS <sub>5</sub> Cl	22	8	28	$\approx 10^{-2}$	[137]
LiPON	77	31	51	$\approx 10^{-6}$	[138]

theoretical-experimental study of  $\beta$ -Li<sub>3</sub>PS<sub>4</sub> in which the microstructure (porosity, particle size and shape) was varied, a large contribution of the grain boundary resistance to the overall resistance was found.<sup>[131]</sup>

The mechanical properties (quasi-malleability) of sulfides at ambient temperature likely eliminate the GB resistance between particles. Additionally, there appears to be little evidence that crystalline domains have a significant resistance contribution for charge transfer across GBs.<sup>[132]</sup> Recently, Wang et al.<sup>[133]</sup> investigated the influence of thiophosphate-type electrolyte crystallinity on the solid-state battery performance. Notably, it was found that larger volume changes and more severe decomposition in the cathode are obtained with crystalline SEs. Higher electronic conductivity and higher elastic moduli of the crystalline SEs may explain this difference.

For salt-in-polymer electrolytes, conduction predominantly occurs via segmental motion of the polymer chains through the amorphous phase.<sup>[134]</sup> Therefore, rather than reducing GB resistance as in oxides, the preparation of polymer electrolytes focuses on minimizing the presence of crystalline domains, which have much lower ionic conductivity.

## 5.2. Solid Electrolyte/CAM Interface

In contrast to the previously discussed LLZO/LLZO and LLZO/CAM interfaces in oxide-based SSBs, this subsection summarizes

the two main degradation phenomena during operation for soft and glassy SEs, being morphological degradation and chemical reactions leading to interfacial degradation.

Regarding the morphological degradation, sulfides (thiophosphates) and polymers generally are softer and have a lower fracture toughness than their oxide counterparts.<sup>[107]</sup> As an overview, **Table 2** lists the mechanical properties of a subset of commonly used SSB materials. Comparing Young's, bulk and shear moduli of Li<sub>6</sub>PS<sub>5</sub>Cl and LLZO:Al, this evident disparity enables the simpler assembly of 3D composite cathodes with soft SEs, which drastically increases the predicted energy and power density in comparison to planar continuous cathode designs. Composite cathodes are generally easier to manufacture using thiophosphates and is demonstrated using different types of thiophosphate SE via cold-pressing,<sup>[103,123,135]</sup> whereas for oxides a high-temperature step is needed.<sup>[12,105]</sup>

However, during the operation, composite electrodes can exhibit morphological changes, e.g., contact loss leading to high impedances. While this can be compensated with a LE,<sup>[139]</sup> contact loss can be induced by volume changes of CAM during (de)intercalation of lithium in combination with SEs. **Figure 5a** depicts SEM images of a cycled cathode consisting of  $\beta$ -Li<sub>3</sub>PS<sub>4</sub> and NCM811 in which contact loss between the materials is evident.

Koerver et al. link this phenomenon to an irreversible resistance increase in the first cycle,<sup>[103]</sup> lowering the Coulombic efficiency to 70.5 %. An approach to overcome this issue, in the

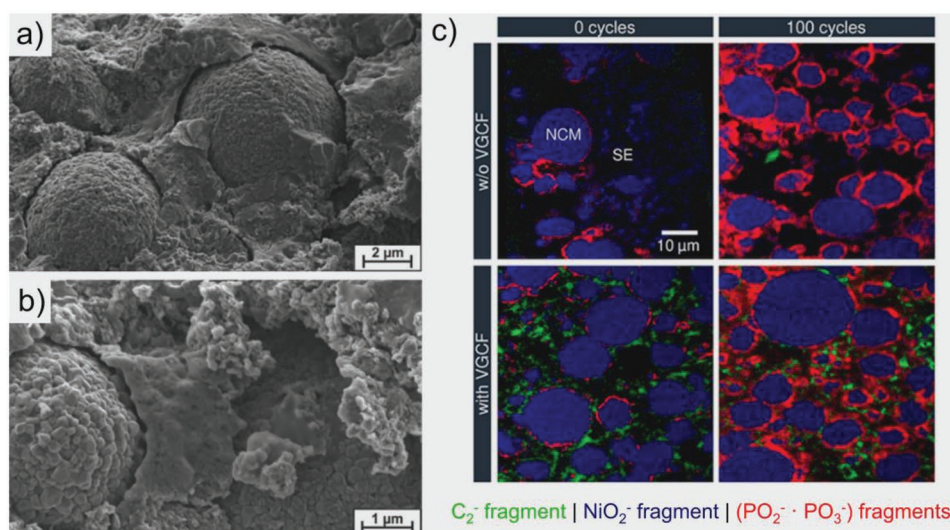


**Figure 5.** a,b) SEM images in different magnifications of the contact loss between  $\beta$ -Li<sub>3</sub>PS<sub>4</sub> and NCM811 after 50 cycles. Reaction byproducts formed between CAM, SE and a carbon fiber additive are mapped using ToF-SIMS as shown in (c). Reproduced with permission.<sup>[103,142b]</sup> Copyright 2017, ACS. Copyright 2020, ACS.



case of thiophosphate electrolytes, is to use substantial pressure (>10 MPa) during operation or by tuning of the cathode composition to avoid deleterious volume changes.<sup>[107]</sup> However, both solutions are considered to be impractical for large-scale applications. Furthermore, phase transitions of CAMs, like the formation of rock-salt and spinel-structures, can also lead to stress-induced cracking of electrode materials.<sup>[140]</sup> While this may not be an issue for traditional LIBs, cracking in SSBs leads to diminished electrode kinetics.<sup>[121a]</sup> Since there are few cycling studies using oxide SEs, it is not understood yet if the aforementioned effects are also present in sintered oxide-oxide cathodes. This is subject of ongoing research.

With respect to the chemical reactions leading to interfacial degradation, oxide SEs are often reported to be stable within a 4 V regime, whereas thiophosphates are thermodynamically unstable beyond 2–3 V versus Li<sup>+</sup>/Li.<sup>[56a,141]</sup> Several studies have shown an increased interphase formation during operation of composite cathodes beyond 3–4 V versus Li<sup>+</sup>/Li.<sup>[103,142]</sup> Recently, Walther et al. identified three different degradation zones in composite electrolytes, being the CAM/SE, CC/SE, and carbon/SE interfaces with a high degree in similarity between the reaction products.<sup>[142b]</sup> The electrochemically formed products during high potentials (oxidation) are predominantly Li-S-P phases with phosphate, sulfate and S<sub>0</sub>-polysulfide species as the thermodynamic byproducts.<sup>[142b]</sup> These reaction products were mapped via ToF-SIMS in cathode composites (Figure 5b). Interestingly, the formation of TM species such as TMS<sup>-</sup>, TMP<sup>-</sup> is negligible in comparison to the aforementioned compounds in electrodes employing NCM622.<sup>[142a]</sup> While this degradation can be partially reversible,<sup>[143]</sup> it still increases the cathode impedance and thus drastically degrades the SSB performance.

While it is a priori difficult to separate chemical and electrochemical degradation due to the similar nature and difficult interface accessibility in composite electrodes, in principal chemical reactions can occur at every interface in composite electrodes. Although these reactions strongly differ between materials, potentials and cell configurations, Sakuda et al. showed cation interdiffusion when combining LCO and Li<sub>2</sub>S-P<sub>2</sub>S<sub>5</sub>-based SE,<sup>[144]</sup> which was confirmed by computational studies.<sup>[145]</sup>

Coating of CAMs is frequently investigated as a way to suppress (electro)chemical reactions between CAMs and SE. For thiophosphate SEs, coatings are considered a necessity to fabricate SSBs with high cyclability.<sup>[142c]</sup> Recently, halides such as Li<sub>3</sub>MX<sub>6</sub> (M<sup>3+</sup>, X = Cl, Br, I) have gained attention for use in SSBs.<sup>[146]</sup> They are stable at high electrode potentials,<sup>[147]</sup> are easily to process, and may have sufficient ionic conductivity for use in composite electrodes. Halides can play a crucial role in enabling SSBs by bridging the gap between soft but degradation-prone thiophosphates and stable but less ionically conductive oxide SEs.

From the modeling point of view, atomistic models reveal that sulfide and phosphate based soft and glassy SEs are generally less stable than LLZO against high voltage CAMs.<sup>[56a]</sup> As a result, severe electrochemical reaction may occur between high voltage CAMs and these soft/glassy electrolytes leading to substantial interdiffusion of ions at the interface, which can be mitigated to a large extent by some form of interfacial coat-

ings.<sup>[145,148]</sup> 1D impedance modeling of a sulfide electrolyte-based solid-state lithium ion cell revealed that the resistance associated with charge transfer at the electrode/electrolyte interface, ion transport through the electrolyte, and solid-state diffusion contributes to the large polarization observed in all-solid-state lithium batteries.<sup>[149]</sup> Decreasing the separator thickness can help to improve the energy and power density of these all-solid-state energy storage devices. Cell level computational modeling of Li<sub>3</sub>PO<sub>4</sub> indicates that lower ionic conductivity of the glassy SEs at room temperature and limited rate performance are major challenges for their commercialization.<sup>[150]</sup> More detailed modeling of the cathode composite electrode 3D structure including sulfide (thiophosphate) electrolyte, NMC CAM, binders, and void spaces showed that distribution of the conductive binder phase has a significant influence on the electrochemically active surface area and ion transport through the tortuous SEs.<sup>[151]</sup> Discrete element method (DEM) based detailed computational modeling of the 3D microstructures of composite cathodes with SEs clarify that high active material loading with large electrochemically active surface area can be achieved by the adoption of fine SE particles.<sup>[33]</sup> Note that even though these analyses were conducted on sulfide based SEs, the general conclusions are applicable to composite cathodes with other SEs as well, such as phosphates and garnets. Computational modeling of the LiPON/LCO interface at both the atomistic and continuum level showed that interfacial delamination can occur between the cathode and SEs due not only to the volume change of the cathode particles, but also to the interfacial reactions that lead to the formation of a cathode/electrolyte interphase whose volume is less than that of the parent materials.<sup>[89]</sup> Implementation of interfacial coatings is a possible pathway to mitigate these interfacial reactions and their detrimental effect on cell performance.<sup>[56b]</sup>

## 6. Hybrid Approach to the SE/CAM Interface

Currently the most common approach to accommodate the limited solid-solid contact area and electro-chemo-mechanical-expansion mismatch at the SE/CAM interface is to utilize an interfacial “soft” liquid, gel, or polymer Li-ion electrolyte (Figure 6a,b). Prior to the incorporation of the soft interphase materials, the cathode active particles are either inserted within the LLZO scaffold,<sup>[4,152]</sup> or mixed with LLZO particles and cast on top of the Al current collector to form the cathode composite.<sup>[153]</sup> Polymer-type soft interphase materials are usually dissolved within the cathode slurry prior to casting,<sup>[154]</sup> whereas the liquid type interphase materials are poured into the porous composite cathode to fill the voids.<sup>[155]</sup> Using this approach enables the use of conventional cathode formulations leveraging the existing Li-ion supply chain. However, by removing direct contact between the cathode and SE, two new interfaces are introduced, i.e., CAM/soft electrolyte and soft electrolyte/SE. Therefore, this soft electrolyte should be chemically and electrochemically stable against both the cathode and the SE as a function of operating temperature and voltage. Otherwise, additional interphases may be necessary to achieve sufficient cycle life.

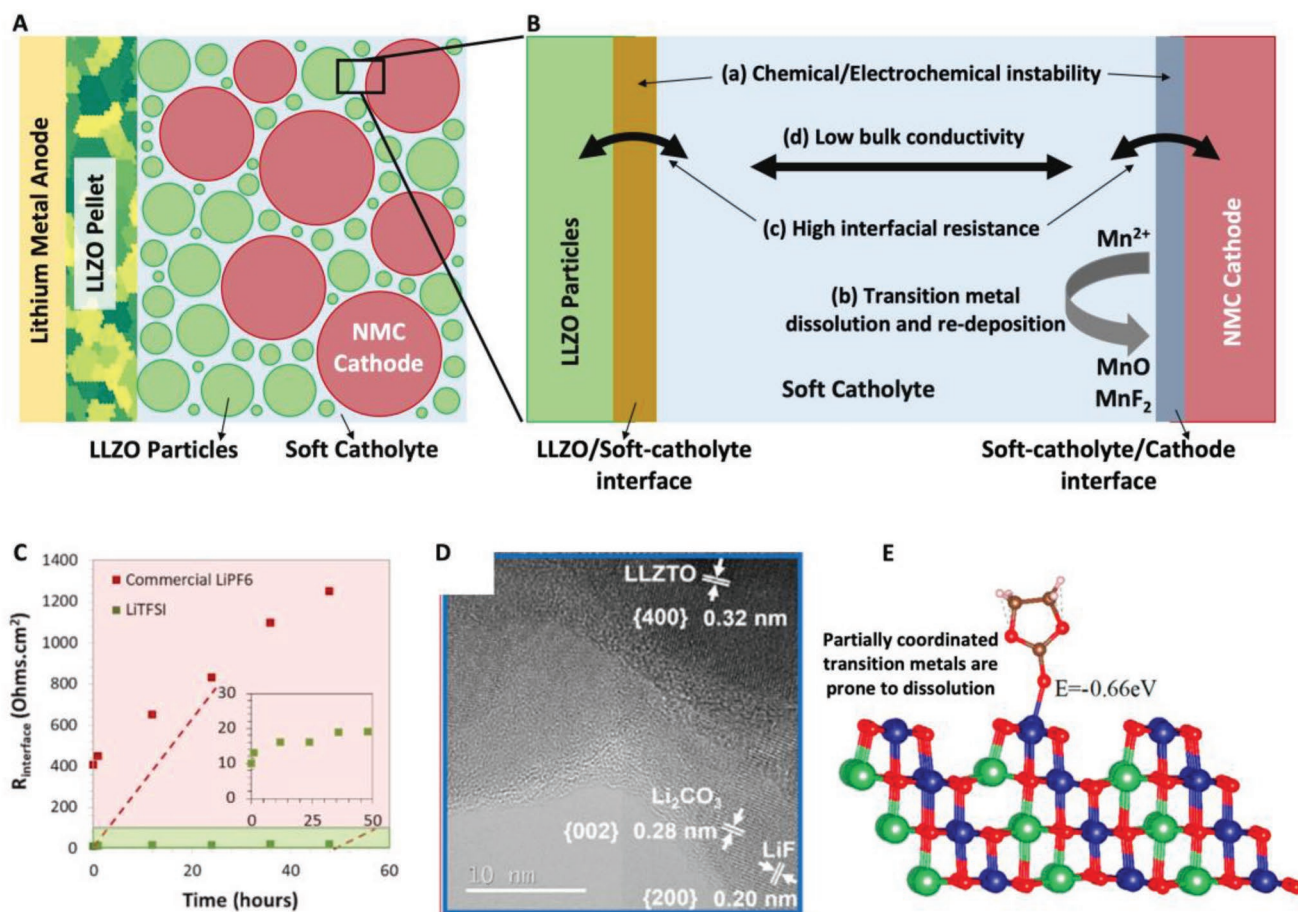


**Figure 6.** a) Schematic representation of a Li metal anode and NMC cathode cell, which consists of a soft catholyte in the cathode composite to enable contact between the LLZO and NMC. b) Schematic representation of a portion of the LLZO/NMC interface with soft catholyte in between. Also highlighted are the various chemical, electrochemical and transport limitations that can occur within the LLZO/catholyte/NMC interfaces. c) Comparison between the increase in interfacial resistance at LLZTO/LiPF<sub>6</sub> and LLZTO/LiTFSI interface. It is evident that LiTFSI salt is more compatible with LLZTO. Reproduced with permission.<sup>[156]</sup> Copyright 2022, Elsevier. d) High-resolution TEM image of Li<sub>2</sub>CO<sub>3</sub> and LiF layer on top of LLZTO while operating with liquid electrolytes containing EC/DMC solvent and LiPF<sub>6</sub> salt. Reproduced with permission.<sup>[157]</sup> Copyright 2020, Elsevier. e) DFT calculations demonstrating the ease of partially coordinate transition metal dissolution in liquid electrolytes. Reproduced with permission.<sup>[158]</sup> Copyright 2019, American Chemical Society.

### 6.1. Challenges with Liquid Electrolyte, Ionic Liquid, and Polymer Interfaces with LLZO

Incorporation of soft interphase layers is associated with interfacial and bulk issues, which can be categorized as follows:

- Interfacial chemical and electrochemical stability of the soft material with cathode and LLZO under high voltage conditions;<sup>[56a]</sup>
- Dissolution of transition metals from cathode (Ni, Mn, Co) into the soft electrolyte;<sup>[159]</sup>
- High interfacial charge transfer resistance between the soft electrolyte and LLZO;<sup>[160]</sup>
- Low bulk conductivity of the interphase material under room temperature conditions;<sup>[161]</sup>
- Uniform distribution of particles and liquid electrolyte within the cathode composite.

These drawbacks and the potential pathways to mitigate them are discussed in this section.

Maintaining good chemical and electrochemical stability at the soft electrolyte/LLZO and CAM/soft electrolyte interfaces is important to minimize the formation of passivation layers. Recently, the interest in protecting Li anodes with ceramic electrolytes for use with state-of-the-art LEs and CAMs motivated studies to analyze the stability between LLZO and state-of-the-art LE.<sup>[156,157,162]</sup> It was found that LiPF<sub>6</sub> salt and carbonate solvents react with LLZO to form resistive interphases (Figure 6c).<sup>[157]</sup> In addition, the use of LiPF<sub>6</sub> may result in HF formation when water is present, which can passivate the LLZO surface. Thus, future work should investigate the use of alternative salts and solvents to improve the compatibility between LLZO and LEs. As for polymer electrolytes, the most commonly used PEO-based soft polymers tend to oxidize at higher voltages, making it very difficult to use high voltage CAMs (NMC, LCO).<sup>[163]</sup> Hence, poly(ethylene glycol) methyl ether acrylate (PEGMEA) or poly(ethylene carbonate) based soft polymer materials that demonstrate stability against high voltage conditions are potential interphase materials between the CAM and

LLZO.<sup>[153a,154a]</sup> Computational modeling studies can help to estimate the HOMO and LUMO levels of these polymer electrolytes and their oxidative stability against high voltage CAMs.<sup>[164]</sup> Atomistic calculations also indicate that ionic liquids (ILs) are stable at high voltage conditions based on the estimations of HOMO and LUMO levels.<sup>[165]</sup> MD analysis further revealed that addition of extra Li salt within ILs can improve their stability against high voltage CAMs.<sup>[166]</sup> In spite of their high voltage stability, some polymer electrolytes as well as ILs tend to react with the Ni-rich CAMs.<sup>[164,167]</sup> However, computational studies to understand the reactivity between these high voltage-stable soft electrolytes and Ni-rich CAMs are lacking.

TM dissolution from the CAM to the soft electrolytes has been extensively studied in the context of Li-ion batteries with LEs.<sup>[168]</sup> In the present context, if a LE is used to improve contact at the CAM/LLZO interface, there always exists some propensity of TM dissolution from the CAM particles to the electrolyte.<sup>[169]</sup> Even though maximum amount of dissolution has been observed for Mn<sup>2+</sup> cations, Ni<sup>2+</sup> and Co<sup>2+</sup> also tends to dissolve from NMC cathode particles into the LE.<sup>[159,168]</sup> TM dissolution leads to a decrease in the active sites for hosting Li-ions, which results in capacity fade.<sup>[97]</sup> Also, redeposition of the TM ions on the surface of the CAM particles as oxides and/or fluorides can lead to the formation of resistive passivation layers and subsequent impedance growth.<sup>[170]</sup> TM dissolution has been observed in both organic as well as IL electrolytes.<sup>[166,168]</sup> Disproportionation reactions experienced by the TMs at lower states of charge, and acid attacks are the major reasons behind the dissolution of CAMs.<sup>[171]</sup> Computational modeling activities at atomistic length scales reveal that partially coordinated TM atoms are more prone to reaction with the solvent molecules and subsequent dissolution within the LEs (Figure 6e).<sup>[158,159]</sup> Continuum level modeling of LE-based LIBs can capture the TM dissolution from the cathode.<sup>[97]</sup> Increase in interfacial and charge transfer resistances due to the metal dissolution and deposition processes can also be successfully captured by cell level models.<sup>[172]</sup> In the present context of CAM/LLZO composites, the tendency for TM to dissolve is much lower due to the use of a very small amount of soft/liquid electrolyte. Moreover, it should be pointed out that the dissolved TMs cannot migrate to the Li anode due to the LLZO separator,<sup>[155]</sup> blocking one of the major degradation mechanisms in conventional LIBs.

Interfacial charge transfer resistance between the soft electrolyte and ceramic electrolyte, such as LLZO, intrinsically originates from two contributions: the resistive interphase layer and the solvation of Li-ion in the soft electrolyte. A resistive interphase layer may form at the interface of two different electrolytes due to their chemical and/or electrochemical incompatibility, which eventually forms an ohmic resistance for the transport of Li-ions across the interface.<sup>[23a]</sup> Unlike in oxide ceramic electrolytes, where the Li-ions are coordinated by oxide ions, the Li-ions in soft electrolytes are surrounded by solvent molecules. Due to the removal of the solvation shell around the lithium cations prior to their insertion into the ceramics, a high charge transfer resistance is observed.<sup>[173]</sup> Sagane et al.<sup>[174]</sup> found in a model system using Li<sub>0.55</sub>La<sub>0.35</sub>TiO<sub>3</sub> (LLTO) as the ceramic electrolyte that polymer/ceramic electrolyte interfaces generally have higher activation energies and room temperature interfacial

resistance than liquid/ceramic electrolyte interfaces. By comparing with the Na-electrolyte system, they hypothesized that the Lewis acidity affects the strength of the interactions with the solvation shell and thus the solvation. In a related study, Abe et al.<sup>[175]</sup> investigated the effect of solvent type on the solvation kinetics at the LE/SE interface. It was shown that the activation energy of solvation/de-solvation at the LE/SE interface positively correlated with the heat of reaction of the solvent and the solvent donor number.

High interfacial charge transfer resistance can also be caused extrinsically by the formation of the resistive Li<sub>2</sub>CO<sub>3</sub> layer on the surface of LLZO (Figure 6d). For example, pre-heating LLZO particles at 400–500 °C can remove the resistive Li<sub>2</sub>CO<sub>3</sub> layer and the charge transfer resistance between PEO and LLZO can be lowered to hundreds of Ω·cm<sup>2</sup>.<sup>[160]</sup> Strategies involving rapid acid treatment of LLZO can also be adopted for removing the resistive Li<sub>2</sub>CO<sub>3</sub> layer.<sup>[176]</sup> Continuum level computational modeling efforts shed light on the overpotential associated with charge transfer across the heterogeneous interface.<sup>[177]</sup>

Apart from the electrochemical stability at soft electrolyte/CAM interface and the high charge transfer resistances between the soft electrolyte and the LLZO, the ionic conductivity of these soft interphase materials under room temperature conditions must also be studied to effectively estimate the potential drop within the electrolyte during cycling.<sup>[6c]</sup> Unfortunately, although several ILs exhibit good electrochemical stability to CAMs, their room temperature conductivity is about one order of magnitude lower than that of organic LEs.<sup>[178]</sup> The viscosity of the IL, the number of charge carriers, the size of the individual ions, and the density all affect their conductivity.<sup>[165]</sup> Using DFT-based atomistic calculations, it is possible to predict the conductivity of ILs as a function of ion volume, ion mass, ion moment of inertia, and ion-ion interaction energy.<sup>[179]</sup> The lithium salt concentration and solvation shell structure around the Li-ions not only have a major impact on the ionic conductivity of ILs, but also on their stability to high-voltage CAMs.<sup>[161,166,180]</sup> Similar to ILs, polymers also demonstrate poor room temperature conductivity unless they are plasticized and converted to a gel form by adding LEs.<sup>[181]</sup> Some standard polymers such as PAN and PVDF show good stability to high-voltage CAMs when used as polymer/ceramic composites with Ta-doped LLZO as the ceramic fillers.<sup>[182]</sup> However, their ionic conductivity at room temperature is orders of magnitude lower than that of LEs, and plasticizers are necessary to achieve reasonable low-temperature performance.<sup>[182b]</sup> The total potential drop during ion transport across the soft interphase layer depends on both ionic conductivity and thickness.<sup>[183]</sup> Computational models should make it possible to estimate the competition between the conductivity and thickness of the interphase layers and determine the optimal conditions for the best cell performance with minimal potential drop across the interphase.

An advantage of hybrid cathode/electrolyte is that no high-temperature cosintering is required for these cathode microstructures. The active particles are infused within the LLZO scaffolds, and the voids between the solid CAM (NMC, LCO, S) and the LLZO electrolyte are filled with LEs to ensure intimate contact.<sup>[155,184]</sup> To fully utilize the lithium stored in the CAMs, the CAM particles should be uniformly distributed in the SE scaffold. In addition, sufficient LE must be incorporated



to fill the pores in the composite cathode layer to avoid incomplete wetting and loss of the electrochemically active surface. Infiltration of the cathode slurry and LE within the LLZO scaffold can be simulated to better understand the distribution of particles and the efficiency of the process, including modeling the surface tension-driven flow of the fluid within the desired porous media.

Problems related to TM dissolution and impedance growth at the CAM/LE interface or the formation of a high-impedance interface between PEO and LLZO during operation can be prevented by the proper adoption of electrolyte additives and/or synthesis techniques.<sup>[155]</sup> For example, the addition of fluoroethylene carbonate (FEC) in the organic LE can help form a stable electrode-electrolyte interface and minimize the dissolution of TM ions.<sup>[159,169]</sup> Computational modeling at the atomistic level revealed that the addition of tris(trimethylsilyl) phosphite (TMSPi) forms a protective layer on the NMC particles and substantially minimizes the dissolution of Ni, Mn, and Co from the CAM particles in the LE.<sup>[186]</sup> MD-based computational models have shown that increasing the lithium salt concentration in the ILEs or saturating the LE with Li salt can help minimize TM dissolution from the CAM particles, either by forming a strong solvation shell<sup>[187]</sup> or by decreasing the acid concentration near the CAMs.<sup>[166]</sup> Applying TiO<sub>2</sub> on a Ni-rich cathode minimizes the side reaction between Ni and high voltage-stable polyoxalate-based polymer electrolytes.<sup>[164]</sup> Similarly, the application of a LATP protective layer on NMC622 minimizes the side reactions between CAM particles and poly(ether-acrylate) based SEs.<sup>[167]</sup> To minimize the interfacial resistance between the ceramic particles and the soft electrolytes, very careful synthesis techniques must be used that effectively result in extremely low ( $\approx 2 \Omega \text{ cm}^2$ ) interfacial resistance between the argyrodite-type SE and PEO.<sup>[188]</sup> Grafting polymer chains onto the surface of the LLZO particles can also help to alter the interfacial resistances between the polymer and ceramic phases.<sup>[189]</sup> In an experimental study on the interface between a ceramic LAGP electrolyte and DOL/DME based LEs, Busche et al.<sup>[190]</sup> found evidence for a solid/liquid electrolyte interphase (SLEI) in which organic and inorganic components form the interphase. They demonstrated that the formation of a SLEI at a liquid/solid electrolyte interface results in a stable and low interphase resistance ( $\approx 25 \Omega \text{ cm}^2$ ). From these studies, it is evident that, depending on the interphase material, there may be various issues at the LLZO/soft electrolyte or CAM/soft electrolyte interface that need to be solved, and computational modeling should help to strategize the optimal pathway.

## 7. Toward All-Solid-State Batteries

Ultimately, it would be desirable to develop an all-solid-state battery that is entirely devoid of flammable liquid and organic components. This not only improves safety and extends operating temperature capabilities, but could also eliminate the self-discharge and capacity fade associated with LEs (e.g., shuttle mechanism in lithium-sulfur batteries, leaching of manganese in high-voltage CAMs, and the reaction between LE and SE).<sup>[157,190,191]</sup> However, LLZO-based cells still face many challenges to achieve competitive energy and power density. High energy density requires high CAM loading, which can only

be realized in cell designs with thick electrode layers and thin ceramic separators. At the same time, fast ion and electron transport through these layers are required to achieve practical power density. Optimizing the composition and structure of LLZO/CAM composite cathodes and separators, minimizing the LLZO GB and CAM/LLZO interfacial resistance, and mitigating the capacity fade during operation, as described in the previous sections, are therefore essential for the successful development of LLZO-based SSBs.

### 7.1. Microstructure and Architecture of Full Cells

The majority of reported LLZO-based cell architectures utilize thick ( $\approx 1 \text{ mm}$ ) sintered dense ceramic separators as a mechanical backbone of the cell, followed by an application of cathode layers and lithium (or indium metal) anodes. The popularity of this separator-supported cell design is explained by relative processing simplicity, enabling fabrication of dense separators with high ionic conductivity via conventional ceramic approaches. However, a thick layer of high-density oxide separator adds to the battery's mass and volume without adding to the storage capacity, severely decreasing energy and power densities on the cell level.<sup>[6]</sup> To create a high-performance SSB, it is clear that the relative fraction of the SE in the cell should be minimized while simultaneously increasing the CAM loading, resulting in cathode-dominated cell concepts. To enable sufficiently fast charge transport through the thick cathodes, the electrochemically active surface area between the CAM and LLZO should be maximized to minimize the total cathode resistance, resulting in an extended 3D CAM/LLZO network analogous to the 3D network of conventional LE cells.<sup>[26c]</sup> The major challenge of these cell concepts is the practical realization of mixed cathodes layers without the processing-induced degradation discussed in Section 3. So far, two main routes have been reported to fabricate fully inorganic LLZO-based composite cathodes. The first route relies on the fabrication of a porous LLZO scaffold, which is subsequently filled with CAM. The second route is based on a cosintering of CAM and LLZO powders combined with a suitable (and ideally scalable) processing approach to form a cathode layer.

As an example of the first route, Hitz et al.<sup>[4]</sup> utilized tape casting to create a porous-dense-porous LLZO "trilayer", where a  $\approx 15 \mu\text{m}$  thick dense layer was mechanically supported by  $\approx 60\%$  porosity extended SE layers that had more than  $40\times$  the interfacial area of a planar electrolyte. Porous morphology of the LLZO scaffold in contact with the lithium metal anode was shown to be beneficial in eliminating lithium dendrites typical for the planar surface of an electrolyte pellet via improving the Li-electrolyte contact and eliminating "hot spots" responsible for inhomogeneous Li-plating.<sup>[192]</sup> Combined with atomic layer deposition (ALD) to improve LLZO-Li metal wetting, lithium metal symmetric cells had extremely low area-specific resistances (ASRs) of  $2\text{--}10 \Omega \text{ cm}^2$  (compared to  $19\text{--}40 \Omega \text{ cm}^2$  for thick pellets) and stable cycling up to  $10 \text{ mA cm}^{-2}$  at room temperature with no applied pressure.<sup>[193]</sup> On the cathode side, infiltration of sulfur in the porous LLZO scaffold provided a thick cathode layer with a high electrode loading and cell energy/power density. A Li-S battery using the same microstructure



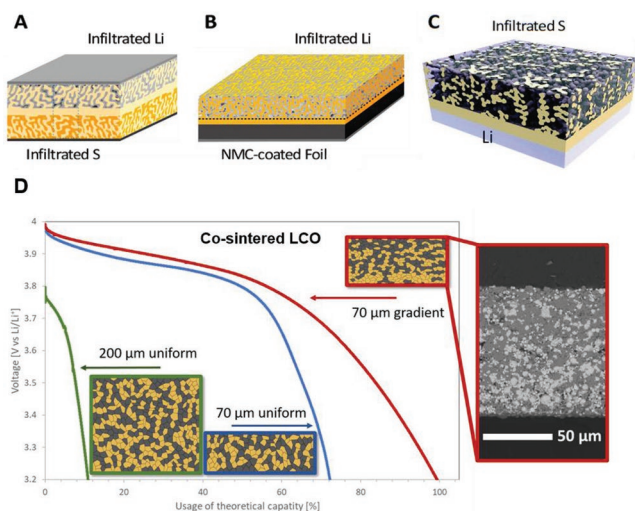


**Figure 7.** a) Trilayer LLZO structure with Li-metal and sulfur electrodes infiltrated into the porous layers. Bilayer structures with b) Li-metal infiltrated into the porous layer and NMC-coated foil attached to the dense layer; Reproduced with permission.<sup>[194]</sup> Copyright 2022, Elsevier. or c) Sulfur infiltrated into the porous layer and Li-metal deposited on the dense layer; Reproduced with permission.<sup>[129a]</sup> Royal Society of Chemistry. d) Electrochemical performance of free-standing, dense, co sintered LLZO+LCO mixed cathodes with uniform distribution (thick and thin) and with a gradient, transitioning from a 2:1 ratio of LLZO:LCO at the separator to an 1:2 ratio at the current collector. (LLZO: white/yellow, LCO: dark gray). Reproduced with permission.<sup>[104]</sup> Royal Society of Chemistry.

had an initial discharge capacity of  $1200 \text{ mAh g}^{-1}$ , corresponding to a cell energy density of  $272 \text{ Wh kg}^{-1}$ , and  $>99\%$  Coulombic efficiency for 50 cycles (Figure 7a).<sup>[129b]</sup> Porous-dense “bilayers” were also fabricated to be compatible with commercial cathode-coated foils while maintaining the enhanced interfacial contact of the anode-infiltrated porous layer, resulting in an NMC-Li battery with stable discharge capacities of  $175 \text{ mAh g}^{-1}$  and  $97\%$  Coulombic efficiency for 25 cycles (Figure 7b).<sup>[194]</sup> The cathode and anode could also be switched to have the cathode infiltrated into the porous LLZO and the anode applied to the planar LLZO surface<sup>[129a,195]</sup> (Figure 7c). This configuration eliminates the inert components (i.e., PVDF binders) in commercial cathode foils, allowing more active material to be used in the same battery volume and thus increasing cell energy density. The tradeoff is that the adoption of a planar LLZO-negative electrode interface will increase the interfacial impedance relative to structured anodes. However, if the issues related to the high current densities at the Li metal/planar LLZO interface can be appropriately addressed, the maximum cell performance can eventually be achieved using this configuration (see Section 7.4).

As testament to the potential of this multilayered approach, several research groups have synthesized extended LLZO microstructures with a variety of methods, including carbon template method,<sup>[196]</sup> 3D printing,<sup>[197]</sup> freeze tape casting,<sup>[198]</sup> drop casting,<sup>[199]</sup> and LLZO-electrode cosintering.<sup>[94a]</sup> The range of electrolyte feature sizes and anisotropy produced by these different methods results in unique internal and interfacial current densities that impact battery performance yet are difficult

to probe experimentally. Continuum scale simulation models can recreate these internal/interfacial current density distributions and thus provide a methodological and systematic basis to evaluate, design, and optimize the extended electrolyte microstructure. For example, a pore-scale model has been successfully developed by Neumann et al.<sup>[27]</sup> to demonstrate the benefit of using Li-infiltrated porous electrolyte layers to reduce local current densities in a “trilayer” garnet configuration. The study further suggested that designing an extended electrolyte layer with porosity gradients would allow additional optimization of cell performance by reducing bottle necks for ion transport in the “trilayer.”

With respect to the second fabrication route, Rosen et al. demonstrated dense, freestanding, cosintered mixed cathodes that were produced via tape casting.<sup>[104]</sup> The advantage of this approach is that the mechanical support is provided by the CAM, which allows reduction of the SE (e.g., LLZO) volume fraction and enables extremely thin separators, e.g., applied via PLD or sol-gel methods.<sup>[200]</sup> However, as reported by Finsterbusch and Danner et al., the effective ionic conductivity of the LLZO limits the extractable capacity for cathode thickness above  $50 \mu\text{m}$ <sup>[12]</sup> and strategies are needed to either improve the total conductivity of the SE itself or the effective conductivity via microstructure optimization. Similar to the advantages of porosity gradients mentioned above, electrochemical performance can be boosted by introducing compositional gradients to change the effective transport parameters. Rosen et al. also demonstrated a microstructurally optimized mixed cathode, featuring opposing gradients for the volume fractions of LCO and LLZO (Figure 7d, SEM cross section). Close to the current collector side, a ratio of 2:1 for LCO:LLZO ensured a high electronic conductivity while a ratio of 1:2 LCO:LLZO at the separator side ensured a high effective ionic conductivity. Compared to nongradient cells using the same materials (Figure 7d green and blue), electrode utilization improved by a factor of 2, reaching almost 100% of the theoretical capacity ( $3 \text{ mAh cm}^{-2}$ , Figure 7d red). Such optimized, free-standing cathodes can then be used as mechanical support for application of thin ( $10 \mu\text{m}$ ) or ultrathin ( $<1 \mu\text{m}$ ) separators. With respect to the former, cosintering of mixed cathodes and thin separators (e.g., via sequential tape casting or screen printing) or hybrid approaches featuring the application of thin ceramic+polymer separators seem promising options and are currently heavily researched. With respect to the application of ultrathin separators, often on the order of  $100 \text{ nm}$ , various concepts using physical vapor deposition,<sup>[201]</sup> pulsed laser deposition,<sup>[200]</sup> or sol-gel application techniques<sup>[202]</sup> sometimes in combination with advanced sintering techniques like flash lamp annealing are also known and investigated. These facile ways to improve battery electrochemical performance by tailoring the composite cathode microstructure and improved processing for separator thickness reduction show that the optimization of ceramic SSBs is still in its infancy.

### 7.1.1. Impact of Cathode Microstructure on Full Cell Performance

For good electrochemical performance, the microstructure of the cathode composite needs to be optimized to maximize the

practical performance of SSB, namely maximizing the electrochemical contact between the SE and the CAM particles; percolating SE network with low tortuosity for ion flow from the separator to the current collector; percolating electron conducting network to maximize electron flow from CAM to current collector; maximizing cathode thickness consistent with ASR transport constraints; maximizing the volume fraction of solid CAM particles to minimize inactive mass, and minimizing voids that reduce electrochemically active surface area and energy density.<sup>[26c,33]</sup>

As discussed in Section 4.2.2, volume changes of CAMs during cell operation cause a significant stress in composite cathodes that can also affect SE transport pathways. More importantly, the volume changes cause mechanical damage to CAM particles as well as delamination and contact loss with SE. Mechanical simulations have been used to calculate deformation and stress in extended SE and CAM networks.<sup>[82,108]</sup> Yu et al.<sup>[82]</sup> reported that NMC composites were less prone to showing mechanical degradation than LCO or LMO electrodes. The anisotropic properties of the LCO crystal and the tendency of LCO particles to align their c-axes perpendicular to the SE surface during cathode processing results in a less pronounced stress distribution at the electrode level.<sup>[108]</sup> However, this orientation is unfavorable for Li-ion transport within the CAMs and deteriorates the electrochemical properties. These are some of the factors that need to be considered when designing and processing the extended SE and CAM networks.

The aim of electrochemical models is to correlate both the overall charge–discharge curves and spatial patterns in current distributions to macroscopic electrochemical measurements. Simulation studies relying on FIB-SEM reconstructions of LCO composite electrodes indicate that cell performance in room temperature experiments still lags behind the simulation predictions, hinting at unaccounted secondary reactions at the CAM/SE interface and further demonstrating the need for protective CAM coatings.<sup>[12]</sup> Recent studies have also indicated that the size distribution of CAM and SE particles, along with Li-ion concentration-dependent changes in reaction kinetics and transport properties, have profound effects on overall cell performance.<sup>[203]</sup> During the sintering step of the cell fabrication process, mechanical simulations have demonstrated that the formation of porous domains at the cathode/electrolyte interface creates stress concentrators that can nucleate cracks and adversely impact cell performance.<sup>[204]</sup>

The Li-ion transport mechanism in CAM/SE composites is highly sensitive to the ion conduction pathways, such as bulk grains, GBs, and structural domains, as well as their respective network. Computational approaches that account for microstructural inhomogeneities can play key roles in analyzing and optimizing microstructural features to maximize ionic transport properties. Both DFT and MD based atomistic computations have revealed that the ionic transport properties at the grain interiors can be very different from that observed in the GB domains and particle surfaces, which is true for all types of SEs (oxides, sulfides, anti-perovskites, etc.).<sup>[13,205]</sup> By solving continuum equations at the mesoscale level, the impact of the microstructural heterogeneity on the effective ionic transport properties have also been investigated.<sup>[13,34,205b,206]</sup> This approach accounts for complex conduction pathways by incor-

porating a realistic representation of the electrolyte microstructure into the modeling framework. For LCO/LLZO composite cathodes, a microstructure-resolved computational modeling approach was used to identify the limitations and obtain design guidelines for improving the electrochemical performance of the cells at the materials and microstructural level.<sup>[12]</sup> Additionally, it has also been computationally demonstrated that specially architected SEs can increase the electroactive area and minimize the reaction current density at the Li/LLZO interface, while decreasing the chances of lithium dendrite growth.<sup>[27]</sup>

For predictive simulations enabling a virtual design of extended SE and CAM networks in LLZO-based SSBs, all aspects described above need to be coupled in the models. Promising studies for other classes of SEs have already been reported and are pointing the direction for future model developments.<sup>[32,204,207]</sup> In addition, close linkage with atomistic-scale simulations is essential to incorporate appropriate material properties that enable the prediction of optimal extended 3D SE-CAM networks for new material combinations. By comparing the simulation predictions with corresponding experiments, improved cell architectures and extended SE-CAM networks can be identified. Further experimental and theoretical work is required to identify the key microstructural parameters that will provide strategies for the engineering of LLZO-based SSB cell architectures.

## 7.2. Solid Electrolyte/CAM Interfacial Coatings

As discussed in Section 3.3, the development of chemically stable interlayer compounds to enable LLZO/CAM combinations during processing is needed. Moreover, as pointed out in Section 4, these interlayers must also be electrochemically stable, not only in terms of Li<sup>+</sup> cycling and SOC, but also in terms of chemo-mechanical expansion mismatch between the CAM and LLZO. In summary, the properties that an ideal interphase layer should meet are as follows:

1. Low melting point to reduce required temperature/time for the co-sintering process;
2. Low surface energy with respect to the CAM and LLZO, so that the interphase material can easily wet both surfaces during high temperature sintering;
3. Chemical stability at the CAM/coating and coating/LLZO interface during sintering;
4. Negligible diffusivity of transition metals (Co, Ni, Mn, La, Zr, Al, etc.) across the interphase layer, preventing interdiffusion and formation of non-conducting passivation layers;
5. Electrochemical stability at CAM/coating and coating/LLZO interface during cycling;
6. High fracture energy between CAM/coating and coating/LLZO interface to minimize interfacial delamination and loss of electrochemically active surface;
7. Low modulus of elasticity of the interphase layer to minimize the stress generation;
8. High Li-ion conductivity and/or low thickness to minimize the overpotential associated with ion transfer across the interphase layer (potential drop);
9. Low charge transfer resistance at the CAM/coating and coating/LLZO interfaces.

So far, chemical and electrochemical stability (including chemomechanical mismatch) could only be achieved in hybrid cell configurations by avoiding cosintering steps and using soft organic interlayers (Section 6). However, for true SSBs, chemically and electrochemically stable interfaces with inorganic interlayers are required. To achieve the required 3D microstructures (Section 7.1), the method used to deposit the interlayer depends directly on the process used to fabricate the structure. In particular, for coating sintered 3D LLZO structures prior to filling with CAM particles, or for coating CAM and LLZO particles prior to co-sintering, gas (e.g., ALD<sup>[69]</sup>) or liquid (e.g., solution infiltration) processes are required to obtain fully conformal coatings, while line-of-sight processes (e.g., sputtering<sup>[68,183]</sup>) would be impractical. Therefore, future computational models should investigate not only cell performance in the presence of the interphase layers, but also the synthesis of cathode microstructures that facilitate the formation of these interphase layers to protect CAMs and SEs.

### 7.3. Need for Advanced Mixed Ionic-Electronic Conducting (MIEC) Cathodes

High temperature sintering of oxide SSBs prevents the use of carbonaceous conductive additives to improve the electron conductivity of the cosintered CAM/SE layer. Any carbon added prior to sintering will burn out if sintered under oxidizing atmosphere or will reduce the oxide ingredients if sintered under inert or reducing atmospheres. Alternatively, infiltration of carbon after sintering is challenging due to the intentionally small inter-particle pore size in dense ceramic cathodes. Instead of carbon, other conductive additives, such as the more expensive indium tin oxide,<sup>[94b]</sup> can be considered as a means to improve the electron conductivity of the cathode layers. However, apart from the higher cost, the addition of non-CAM additives will inevitably compromise battery energy density, which is contrary to the goal of developing SSBs. Clearly, the preferred solution to overcome these challenges is to remove the conductive additives completely. This can be accomplished either by increasing the ionic and electronic conductivity of the CAM or by developing mixed ionic-electronic conducting (MIEC) solid oxide electrolytes. The latter has been practiced extensively in the development of solid oxide ionic conductors for fuel cells and gas separation membranes.<sup>[208]</sup>

In terms of increasing CAM conductivity, promising cell performance has recently been reported for sulfide-based all-solid-state cells with NMC622 (electronic conductivity  $\approx 0.01 \text{ S cm}^{-1}$ ) as the CAM.<sup>[123]</sup> Initial attempts on oxide-based SSBs have been conducted using LCO (electronic conductivity:  $10^{-3}$ – $10 \text{ S cm}^{-1}$  depending on lithium deficiency<sup>[209]</sup>) as the CAM,<sup>[83,105]</sup> although practical performance at room temperature has not yet been achieved. Even for LE cells with high ionic conductivities, insufficient ionic conduction through the cathode layer is the primary challenge to achieving high rate capabilities with CAMs with reasonably high electronic conductivity,<sup>[210]</sup> especially as cathode layer thickness increases. Electronic conductivity is also important, especially when thicker cathode layers are used to achieve higher areal specific capacity.<sup>[211]</sup> Recent efforts with SSBs indicate similar trends,<sup>[212]</sup>

but SEs, by definition, do not infiltrate like LEs into the CAM pores to provide an ion-conducting path and so only part of the CAM surface may interface with the SE. Therefore, the maximum CAM particle size will be limited by the Li-ion diffusion distances between the (potentially limited) CAM/SE interfaces and the CAM particle interiors.

Conversion-type cathodes have great potential to increase the specific energy of cells due to their high specific capacities. Unfortunately, they are extremely poor electrical conductors, e.g.,  $\text{FeF}_3$ , S, and  $\text{O}_2$ . Therefore, to use such conversion materials in SSBs without an additional electron-conducting phase, the electronic conductivity of the solid cathode composite would need to be increased.<sup>[213]</sup> However, the development of MIEC capability for garnet-type electrolytes is still in its infancy, with only a handful of published studies.<sup>[214]</sup>

### 7.4. Projection of SSB Energy Density and Rate Capability

Calculations of cell-level performance provide projections for potential energy and power densities that can be achieved with a particular design and chemistry of anode, cathode, and electrolyte, as well as insight into the factors that limit cell voltage and capacity.<sup>[61,7]</sup> Since this paper focuses on cathode architectures, we modeled the potential performance based on LLZO bilayer cells using the design shown in Figure 7c, where lithium metal anodes were attached to a  $10 \mu\text{m}$  LLZO dense layer and various CAMs were envisioned as infiltrated/cosintered into the porous LLZO layer.

#### 7.4.1. Assessment of Theoretical Energy Density

Figures 8c and 8d show the theoretical thermodynamic energy densities attainable for LLZO-based bilayer cells, assuming a CAM content of 75 vol.% in the 3D CAM/LLZO layer with a thickness up to  $100 \mu\text{m}$ . It should be noted that the Wachsman group has prepared 3D LLZO scaffolds with porosities up to 85%.<sup>[196]</sup>

The upper bounds in **Figure 8c,d** represent the maximum energy density attainable for each cathode chemistry, where the cathode layers are comprised of only LLZO and CAM (Figure 8a). The parameters used for each cathode chemistry are detailed in Table S1 (Supporting Information). The maximum theoretical cell energy densities increase linearly at low cathode thickness due to the LLZO separator mass/volume contributing significantly to the total cell mass/volume, and then cell energy densities approach a horizontal asymptote at high cathode thicknesses as the LLZO separator mass/volume becomes insignificant in comparison to the cathode/anode mass/volume. The higher specific energies of the conversion cathodes (i.e., Li-air, sulfur,  $\text{FeF}_3$ ) result in theoretical gravimetric energy densities of  $660 \text{ Wh kg}^{-1}$  to  $>1000 \text{ Wh kg}^{-1}$  for a cathode thickness of  $\approx 50 \mu\text{m}$ ; whereas the lower specific energy intercalation cathodes (i.e., LCO, NMC622, NMC811) achieve theoretical energy densities of up to  $519 \text{ Wh kg}^{-1}$  for the same thickness and  $567 \text{ Wh kg}^{-1}$  for a  $100 \mu\text{m}$  NMC811 thick cathode. In contrast, the volumetric cell energy densities of some cells with conversion cathodes and intercalation cathodes overlap because cells with conversion cathodes must have an empty



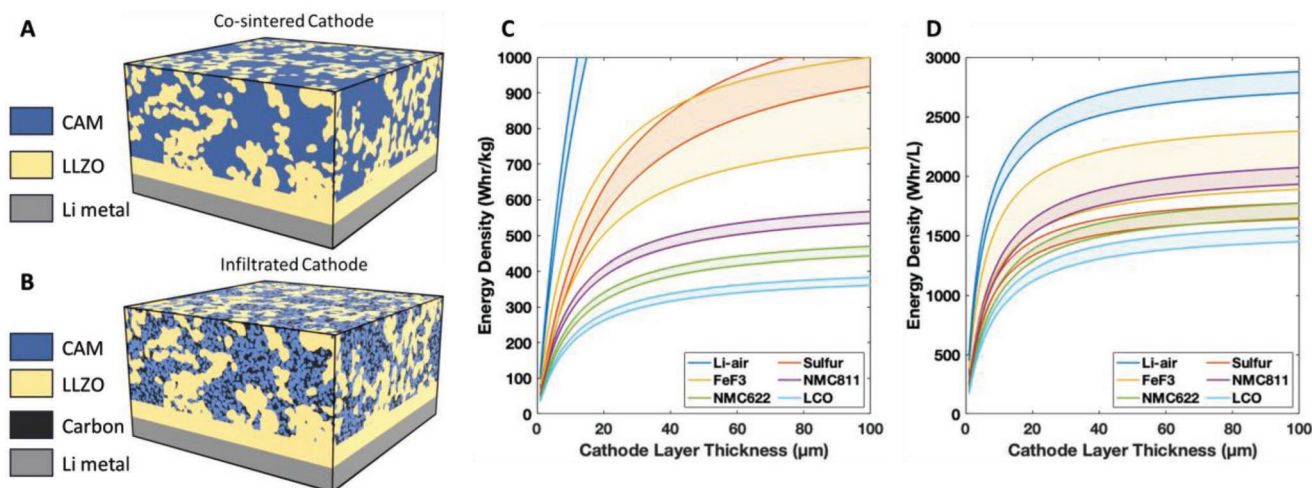


**Figure 8.** Cell designs with lithium metal anodes attached to the LLZO dense layer and cathodes co-sintered (A) or infiltrated (B) into the porous LLZO layer. C) Gravimetric cell energy densities and D) volumetric cell energy densities calculated for LLZO bilayer cell designs. The upper bounds represent cells with only electrolyte and active electrode materials (Figure 8A).<sup>[216]</sup> The lower bounds represent cells with the active cathode materials partially replaced by electronically conductive additives (Figure 8B).

pore volume to allow for cathode expansion during lithiation (e.g., 78.7% volume expansion for S and 14.1% volume expansion for  $\text{FeF}_3$ ).

However, neither laboratory nor commercial cells have achieved energy densities near these maximum values, largely because the CAM has been replaced with inert components. For example, the lower limits in Figure 8c,d represent cells that contain electronically conductive additives to compensate for the low CAM electronic conductivity (Figure 8b).<sup>[215]</sup> Even small amounts of this critical additive significantly reduce cell energy density, and cells often contain additional inert components such as binders to ensure full CAM utilization. Clearly, optimizing the cell design to minimize the use of inert components as well as the remaining porosity is a key requirement for creating the cells with high energy density. Furthermore, if the ionically conducting/electronically insulating 3D SE network in the cathode structure can be replaced by a MIEC, then even the critical electronically conductive additives can be removed, and cell performance can approach the maximum energy density limits shown in Figure 8c,d.

It should also be noted that processing/yield issues may require a thicker dense separator layer than modeled here. However, a majority of the LLZO mass and total cell mass in the bilayer structure is in the composite cathode layer rather than the dense separator layer. For example, if the dense layer was tripled in thickness to 30  $\mu\text{m}$  for a 100  $\mu\text{m}$  thick cathode comprised volumetrically by 75% NMC 811 and 25% LLZO (the design parameters used above) this would be a 57% increase in LLZO mass, but only an 18% increase in total cell mass for cell with no other cathode components that would otherwise reduce this mass % increase further.

#### 7.4.2. Prediction of Kinetically Limited Energy Density during Operation

While the theoretical thermodynamic specific energies presented in the Section 7.4.1 are extremely encouraging and would

in fact be game changing for conversion cathode materials, real batteries are also kinetically limited by the accessible cathode thickness for a desired current density/C-rate. During operation, transport losses and kinetic losses will reduce the attainable capacity of the cathode and the overall specific energy of the cell. The challenges of LLZO-type SSBs and strategies to mitigate them are discussed in detail in this paper, with a focus on commercially available lower energy density intercalation cathodes (e.g., LCO and NMC). Although conversion cathodes offer much higher theoretical energy densities, we focus here on the commercially available CAM with the highest demonstrated specific energy (NMC811) and use continuum-scale computational models to quantify the effects of NMC811 and LLZO bulk properties and NMC811/LLZO interfacial processes on cell performance for the cell architecture shown in Figure 8a.

**Model Description:** The calculations of specific energy under operation conditions are based on simulations with a pseudo-2D model following the formulation presented in ref. [217] for state-of-the-art LIBs. This model was then specifically adopted for the simulation of LLZO-type SSBs. A schematic representation of the continuum model in the form of a representative equivalent circuit is shown in Figure 9c. The calculations can be considered optimistic but realistic estimates of cell performance, assuming percolating transport pathways in both CAM and SE when neglecting electrochemical and mechanical degradation phenomena. The constitutive equations and model assumptions are described in detail in the Supporting information. An overview of the material properties used in this case study can be found in **Table 3**. It must also be emphasized that these calculations were performed for pure all-solid-state batteries without any additional electronically (e.g., carbon) or ionically (e.g., LE) conducting phase or phases to fill interparticle voids.

**Case Study:** The cell setup is illustrated in Figure 8a and corresponds to the setup used for the assessment of theoretical energy density in Section 7.4.1 (Figure 8a,b). The simulations predict the impact of improvements in material properties and

**Table 3.** Parameters and material properties in dynamic calculations.

Case	State-of-the-art	Improved materials
NMC811		
Density [g cm <sup>-3</sup> ]		4.87 <sup>[218]</sup>
Q <sub>theo</sub> [mAh g <sup>-1</sup> ]		218.66 <sup>[218]</sup>
Mol. weight [g mol <sup>-1</sup> ]		97.28
U <sub>nom</sub> [V]		3.86 <sup>[218]</sup>
d <sub>50</sub> [μm]	10 <sup>a)</sup>	0.1 <sup>b)</sup>
D [cm <sup>2</sup> s <sup>-1</sup> ]	2.54 × 10 <sup>-12</sup> <sup>[121a]</sup>	2.54 × 10 <sup>-11</sup> <sup>[219]</sup>
κ [S cm <sup>-1</sup> ]	4.54 × 10 <sup>-2</sup> <sup>[220]</sup>	3.15 <sup>[209]</sup>
R <sub>CT</sub> [Ω cm <sup>2</sup> ]	2600 <sup>[183]</sup>	150 <sup>[183]</sup>
R <sub>SP</sub> [Ω cm <sup>2</sup> ]	2600 <sup>[183]</sup>	0 <sup>b)</sup>
LLZO		
Density [g cm <sup>-3</sup> ]		5.077
σ [S cm <sup>-1</sup> ]	8 × 10 <sup>-4</sup> <sup>[27]</sup>	1.0 × 10 <sup>-2b)</sup>
β <sub>CB</sub> / -	1.39 <sup>[27]</sup>	0
β <sub>int</sub> / -	2.31 <sup>[27]</sup>	1.5 <sup>a)</sup>
Li		
Density [g cm <sup>-3</sup> ]		0.534
Q <sub>theo</sub> [mAh g <sup>-1</sup> ]		3861.3
Mol. weight [g mol <sup>-1</sup> ]		6.941

<sup>a)</sup>Design parameter; <sup>b)</sup>Desired parameter to reach close to theoretical specific energy; The nominal voltage U<sub>nom</sub>, CAM chemical diffusion coefficient D, and CAM conductivity κ are given as averaged value between 3 and 4.3 V. The corresponding correlations can be found in Figure S1 (Supporting Information).

material processing on the performance of garnet-based SSBs with a NMC811/LLZO composite cathode. The composites have a fixed CAM content of 75 vol% and a thickness of either 50 or 100 μm. For the dynamic calculations, we restrict the discussion to the specific energy E<sub>m</sub> as a characteristic performance indicator. The virtual cells were operated at two relevant current densities, namely 1 and 10 mA cm<sup>-2</sup>. The former is often reported as the critical current density for stable operation of lithium metal electrodes in a planar design. Suitable interface engineering or 3D design (see Section 7.1) could enable dendrite-free operation at current densities up to 10 mA cm<sup>-2</sup>. Both current densities are investigated in detail to predict the most relevant material developments. The specific energies for variations of different material properties are presented in **Figure 9**.

First, we perform a sensitivity analysis of the virtual cells to determine the limiting processes for the state-of-the-art materials. For the sensitivity analysis, all parameters are set to the values in the right-hand column of Table 3, which represents a set of parameters where none of the processes limits the cell performance at 1 and 10 mA cm<sup>-2</sup> and the cell specific energy is close to the theoretical values of 519 Wh kg<sup>-1</sup> and 567 Wh kg<sup>-1</sup> depending on electrode thickness. In a second step, individual parameters or groups of parameters related to ionic and electronic transport, interface processes, and Li-ion mobility in CAMs are set to the values in the left column of Table 3 representing in state-of-the-art parameters. The corresponding adjusted parameters are given in parentheses below each case name.

The simulated specific energies of the virtual cells are shown in Figure 9a,b, with the red and blue lines representing virtual cells operating at current densities of 1 and 10 mA cm<sup>-2</sup>, respectively. The corresponding gap between the lines and the outer perimeter of the coordinate system represents the loss in specific energy and visualizes the sensitivity of cell performance to each parameter. The simulations show that improvements to the ionic conductivity within the composite cathode (“LLZO Ionic Conductivity” and “LLZO Secondary Phases”) are most critical to improving the specific energy of LLZO-type SSBs, especially at high loadings and current densities. Interface processes, namely the effect of resistive interphases (“Resistive Interphases”) and charge transfer kinetics (“LLZO/CAM Charge Transfer”) also have a prominent effect, though primarily at high current densities due to the high specific interfacial area of the composite cathodes mitigating interface limitations at low current densities. The mobility of Li in the CAM (“CAM Li Diffusion Length”) is crucial to improving the utilization of the CAMs and will require the development of suitable materials to resolve current limitations, which will be discussed in more detail in the paragraphs below. Finally, the effective “Electronic Conductivity” of the composite was found to have a minor effect on the cell specific energy, indicating that the electronic conductivity is not limiting the cell performance in the current cell design with high CAM content.

The results of this sensitivity study suggest the optimal strategy for improving the practical specific energy of garnet-type SSBs is as follows: 1) improve the effective composite ionic conductivity by reducing secondary phases and grain boundaries, 2) improve interfacial resistance by reducing resistive interphases, 3) improve the mobility of Li in the CAM by reducing the CAM internal grain boundaries and overall particle size, 4) improve the effective electronic conductivity of the composite and ensure percolating 3D transport networks. Figure 9d shows the resulting gains in cell-specific energy made by following this development strategy, beginning with cells with state-of-the-art parameters (gray bar, left column in Table 3) and cumulatively adding individual improvements due to changing individual material properties or processing (right column in Table 3). Improvements related to interfaces within LLZO or between LLZO and NMC811 are indicated by the red bar, while improvements related to the electrode or NMC811 microstructure and morphology are indicated by the blue bar. The green bar depicts improvements of the ionic or electronic conductivity, allowing to access specific energies close to the thermodynamic limit shown by the purple bar. Note that in this procedure, in addition to the absolute improvements of the individual material properties, the order of the improvements is also crucial and has a significant influence on the practical achievable specific energy of the respective case. Therefore, the development strategy presented in this section first addresses the most pressing improvements needed to unlock the potential of oxide-based solid-state batteries.

*State-of-the-Art Materials and Processing:* To our knowledge, no additive-free LLZO-based SSBs with NMC811 composite cathodes have been reported in the literature so far. The gray bars in Figure 9d show the specific energy predicted by our calculations based on material-specific data published in the literature for LLZO and NMC811. Fabrication of NMC811 composite

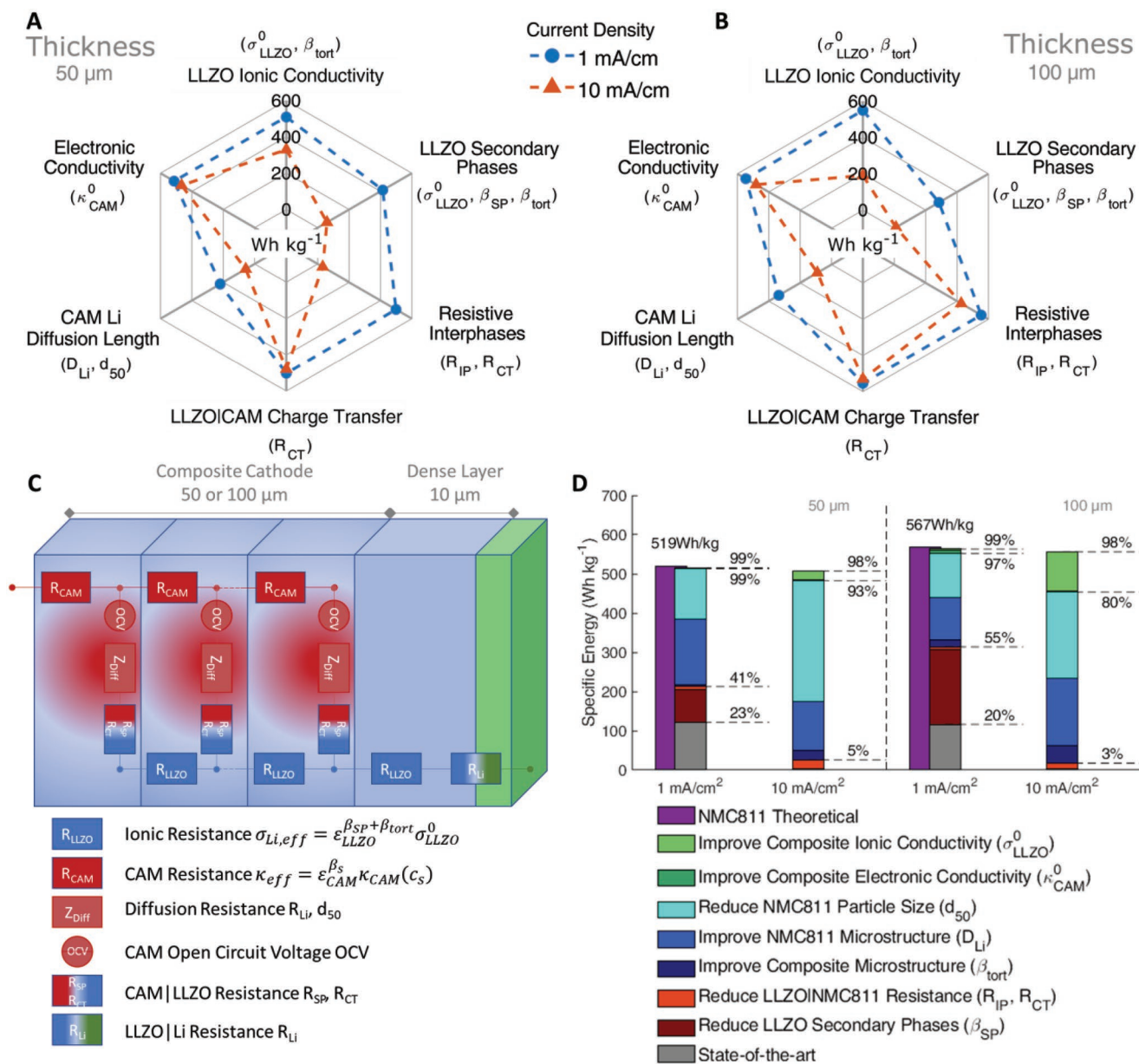


**Figure 9.** Case study predicting the development of specific energy for the cell design shown in Figure 8a. Spider plots in A,B) present the sensitivity of NMC811/LLZO/Li cells towards various material and design parameters indicated by the loss in specific energy compared to improved materials (see right column in Table 3). A) Composite electrode thickness of 50  $\mu\text{m}$  and B) composite electrode thickness of 100  $\mu\text{m}$ . Red and blue lines represent current densities of 1 and 10 mA  $\text{cm}^{-2}$ , respectively. The corresponding model parameters are shown next to each case and are set to the left column of Table 3 representing state-of-the-art materials. The continuum model setup is represented by the schematic equivalent circuit shown in C). The sensitivity provides the basis for the development strategy presented in Figure 9D). Gray bars indicate the specific energy of electrodes made of state-of-the-art materials. All other colors represent cases corresponding to improved material properties or processing conditions. Improvements related to interfaces within LLZO or to NMC811 are indicated by red color, and improvements related to the electrode or NMC811 microstructure and morphology are given in blue. The green bar depicts improvements of the ionic or electronic conductivity allowing to access specific energies close to the thermodynamic limit shown in the purple bar.

electrodes is an ongoing challenge and similar performance has to be demonstrated in future experimental work. Nonetheless, this case represents the parameter basis of our study and the upper limit that can be achieved with state-of-the-art processing methods and commercial materials.

The predicted state-of-the-art specific energy for a cell operated at a current density of 1 mA  $\text{cm}^{-2}$  is about 24 Wh  $\text{kg}^{-1}$

and 15 Wh  $\text{kg}^{-1}$  for a composite cathode thicknesses of 50 and 100  $\mu\text{m}$ , respectively. This corresponds to about 5% and 3% of the above thermodynamic values, respectively. Comparison of the theoretical specific energy with the dynamic calculations highlights the kinetic limitations observed with state-of-the-art materials and processing conditions. At 10 mA  $\text{cm}^{-2}$  this effect is even more pronounced, and the simulations predict



negligible specific energy for the state-of-the-art materials in the given cathode architecture. In the following sections, we discuss the material properties of the reference case and high-light relevant material, processing, and design developments to advance LLZO-based SSBs.

*Internal Electrolyte and Electrolyte/Cathode Interfaces:* A key aspect of this perspective is interfaced in oxide-based solid-state batteries. In particular, we discuss the role of internal electrolyte interfaces and interfaces between the SE and CAM. First, we focus our attention on the role of homo-interfaces and secondary phases in the SE. In a recent study, Neumann et al.<sup>[27]</sup> found that the GB resistance and secondary phases in highly porous samples contribute significantly to the overall resistance of SE. In combination with the geometrical tortuosity of the SE network, these effects reduce the effective ionic conductivity by more than two orders of magnitude from  $\sigma_{\text{LLZO}}^0 = 8 \times 10^{-4} \text{ S cm}^{-1}$  to  $\sigma_{\text{Li,eff}} = \epsilon_{\text{LLZO}}^{\beta} \sigma_{\text{LLZO}}^0 = 5 \times 10^{-6} \text{ S cm}^{-1}$  ( $\beta_e = \beta_{\text{ort}} + \beta_{\text{GB}} = 2.31 + 1.39 = 3.7$ ). Mitigation strategies aimed at reducing the contributions from secondary phases and GBs are outlined in detail in Section 2. By avoiding secondary phases and assuming GB contributions similar to those measured in dense pellets<sup>[27]</sup> ( $\sigma_{\text{LLZO}}^0 = 8 \times 10^{-4} \text{ S cm}^{-1}$ ,  $\beta_{\text{GB}} = 0$ ), one can boost the effective ionic conductivity to  $\sigma_{\text{Li,eff}} = 3.3 \times 10^{-5} \text{ S cm}^{-1}$ . This optimization results in a jump of the predicted specific energy to more than 200 Wh kg<sup>-1</sup> and 300 Wh kg<sup>-1</sup> for the electrodes with 50  $\mu\text{m}$  and 100  $\mu\text{m}$  thickness, respectively. In the latter case, this is already more than 50% of the theoretical specific energy. This demonstrates that optimization of the effective LLZO conductivity in the 3D network is of paramount importance. Despite the significant effect at 1 mA cm<sup>-2</sup>, only moderate improvements are predicted at 10 mA cm<sup>-2</sup>, indicating that additional limitations need to be resolved to enable operation at high current densities.

Section 3 addresses issues in the processing of LLZO/CAM interfaces. An interface impedance of about 2600  $\Omega \text{ cm}^2$  between LCO and LLZO has been reported in the literature. Ruess et al. measured a similar interfacial resistance for their NMC811-containing cells with an agyrodite-type SE.<sup>[121a]</sup> In the absence of data on NMC811/LLZO interfaces, we define this resistance as the state of the art for our virtual cells. In both systems mentioned above, the local interfacial resistance comprises contributions due to the charge transfer ( $R_{\text{CT}}$ ) and secondary phases resulting from electrolyte degradation during processing and operation ( $R_{\text{SP}}$ ). Deconvolution of the contributions in impedance data is challenging. In the state-of-the-art case, we assume that most of the interfacial impedance can be attributed to resistive secondary phases. Under these conditions, close to linear dependence of the overpotential on the current density is expected. Indeed, we see a significant drop of the cell voltage during simulated cycling already at 1 mA cm<sup>-2</sup>. At 10 mA cm<sup>-2</sup>, the cell voltage drops below the cutoff voltage almost immediately, despite the ionic transport improvements described in the previous paragraph. We assume that with appropriate processing procedures, the resistive interphases can be significantly reduced. In this case, the charge transfer across the SE/CAM interface is Faradaic in nature and can be described by the common Butler-Volmer equation. Note that in this case the overpotential depends logarithmically on the current, which promises significantly reduced overpotentials during operation

at high current densities. Strategies for improving stability and charge transfer resistance using different coating strategies have also been discussed in Section 7.2. For instance, coatings have been shown to effectively reduce the resistance of the LCO/LLZO interface by more than an order of magnitude.<sup>[183]</sup> An important consideration, discussed in detail in Section 4, is space charge layers that impede charge transfer and can be reduced by appropriate interface engineering.<sup>[221]</sup> Coating strategies have yet to be developed for NMC-type materials, but in general similar effects are anticipated. Corresponding simulations are shown by the light red bars in Figure 9d. At 1 mA cm<sup>-2</sup>, the simulations predict minor improvements in specific energy compared to the significant increase obtained by improving LLZO internal interfaces (dark red bar). However, at 10 mA cm<sup>-2</sup>, improvements in the NMC811/LLZO interface allow the virtual cell to demonstrate some specific energy, albeit only 3–5% of the theoretical specific energy depending on cathode thickness. This is a key step and demonstrates the importance of interface design for operation at high current densities. A major advantage of the 3D electrode design compared to planar interfaces is the orders of magnitude larger reactive surface area. It should be noted that chemo-mechanical effects at the interface due to volume changes during operation also play an important role in this context and can lead to loss of contact and active surface area. Strategies to mitigate these effects are described in Section 5. Nevertheless, the simulations indicate that a local charge transfer resistance of about 150  $\Omega \text{ cm}^2$  no longer limits the cell performance even at 10 mA cm<sup>-2</sup> once the secondary phases at the interface can be mitigated.

*Microstructure of Composite Electrodes and Cathode Active Materials:* Section 7.1 presented various design paradigms to improve the specific energy of LLZO-based SSBs. One important aspect is the microstructure of the composite cathode. Two key parameters determining the composite cathode architecture are the thickness and CAM content. The dependence of specific energy on CAM content is also illustrated in Figure S2 (Supporting Information). In the study presented here the CAM content of the composite cathode is fixed to 75 vol.%, which promises a very high thermodynamic specific energy. However, high CAM content increases the tortuosity of the 3D SE network and thus decreases the effective ionic conductivity, which is one of the major bottlenecks for practical SSBs. Therefore, optimization of the 3D ionic network is important to reduce the tortuosity of the transport pathways, and the benefit of improved cathode architectures is illustrated by the dark blue bars in Figure 9d. Reduction of electrode tortuosity ( $\sigma_{\text{LLZO}}^0 = 8 \times 10^{-4} \text{ S cm}^{-1}$ ,  $\beta_e = \beta_{\text{ort}} = 1.5$ ) provides an effective ionic conductivity as high as  $\sigma_{\text{Li,eff}} = 1 \times 10^{-4} \text{ S cm}^{-1}$ . The simulations indicate that optimization of the 3D SE transport network is particularly important for thick electrodes and high current densities. Optimized microstructures are predicted to double the specific energy of virtual cells with 100  $\mu\text{m}$  thick cathodes operating at 10 mA cm<sup>-2</sup>, reaching up to 11% of the theoretical specific energy. Although these numbers are promising, they also suggest that additional improvements in SE conductivity as well as CAM properties are critical to achieve competitive cell performance (as discussed later).

The mobility of Li-ion in the CAM determines the utilization of the active material. Ruess et al.<sup>[121a]</sup> measured the

chemical diffusion coefficients of Li-ions in polycrystalline NMC811 using both LEs and SEs. In particular, the effective or chemical diffusion coefficient in polycrystalline NMC811 measured with SEs was found to be about  $D = 2.5 \times 10^{-12} \text{ cm}^2 \text{ s}^{-1}$ , which is more than an order of magnitude lower than the value measured in the same material with an LE. This demonstrates the role of homo-interfaces for Li-ion mobility in CAMs for SSBs. Recently, single-crystal active materials have been proposed for SSBs with up to an order of magnitude higher chemical diffusion coefficient ( $D = 2.5 \times 10^{-11} \text{ cm}^2 \text{ s}^{-1}$ ).<sup>[219]</sup> Corresponding simulations with enhanced Li-ion mobility in NMC811 (light blue bar) predict a significant increase in specific energy, mainly due to much better utilization of NMC811. At  $1 \text{ mA cm}^{-2}$ , up to 78% of the theoretical specific energy can eventually be achieved. Internal CAM interfaces are also included in Figure 1, but their relevance has not yet been discussed in detail in this context. Nevertheless, the simulations demonstrate the importance of designing CAM particles with a defined microstructure. Another simple yet efficient strategy to reduce diffusion limitations is to reduce the effective diffusion length. The simulations predict that complete lithiation of the CAM particles requires a reduction of the particle diameter down to 100 nm. At  $1 \text{ mA cm}^{-2}$  virtual cells using these reduced CAM particles demonstrate specific energies already close to the theoretical limit. However, the processing of the materials and the design of the corresponding cathode architectures might prevent the application of small CAM particles.<sup>[33]</sup> Still, reducing the CAM particle diameter to  $2.5 \mu\text{m}$  was found to provide specific energies of more than 90% of the thermodynamic limit. At  $10 \text{ mA cm}^{-2}$  the effect of the Li chemical diffusion length is even more pronounced and the cell specific energy increases dramatically after reducing CAM particle diameter to 100 nm size, though it is still less than the specific capacity of identical cells operated at  $1 \text{ mA cm}^{-2}$ . The simulations indicate that additional improvements in material transport properties are required at high current densities for ultrahigh specific energies close to the theoretical limits.

**Composite Ionic and Electronic Conductivity:** Another critical parameter, discussed in Section 7.3, is the effective electronic conductivity and the connectivity of the CAM network in the cathode composite. Note that the formation of an interconnected network is one of the fundamental assumptions of the model and is intrinsically included in the calculations. The conductivity of NMC materials varies between  $10^{-1}$  and  $10^{-5} \text{ S cm}^{-1}$  depending on the lithium content.<sup>[220a]</sup> Even near the fully lithiated state, it is of the same order of magnitude as the LLZO conductivity, which means that the electronic conductivity does not limit the utilization of the active material during most of the discharge cycle. In the thick electrode, with an average effective conductivity of  $\kappa_{\text{eff}} = 2.3 \times 10^{-3} \text{ S cm}^{-1}$  ( $\kappa_{\text{CAM}}^{\text{av}} = 4.52 \times 10^{-2} \text{ S cm}^{-1}$ ,  $\beta_s = 2.3$ ), the ohmic loss is only around 50 mV at  $10 \text{ mA cm}^{-2}$ . Nevertheless, insufficient contact between the CAM particles could increase the electronic resistance and lead to larger ohmic losses, especially at high current densities. This indicates that the primary, yet very important, role of conductive additives or mixed ionic-electronic SEs discussed in Section 7.3 is to form a percolating network to maximize CAM utilization.<sup>[222]</sup> The electronic conductivity of these materials should then surpass the

NMC811 conductivity to improve performance at higher current densities.

Most of the green bar in Figure 9d can indeed be attributed to improvements in the SE ionic conductivity. Qin et al.<sup>[1]</sup> showed that self-textured growth of Ga-doped LLZO can provide improved conductivities of up to  $2 \text{ mS cm}^{-1}$ . The substantial increase in ionic conductivity to  $\sigma_{\text{Li,eff}} = 2.5 \times 10^{-4} \text{ S cm}^{-1}$  ( $\sigma_{\text{LLZO}}^0 = 2 \times 10^{-3} \text{ S cm}^{-1}$ ,  $\beta_e = \beta_{\text{tot}} = 1.5$ ) eventually allows to access more than 97% of the specific energy at  $10 \text{ mA cm}^{-2}$ . Yet, to gain the last few remaining percent of specific energy, considerable improvements in the bulk SE ionic conductivity up to  $\sigma_{\text{LLZO}}^0 = 1 \times 10^{-2} \text{ S cm}^{-1}$  are required. These simulations suggest that full CAM utilization at high current densities in 3D composite electrodes is likely to be virtually impossible at room temperature for practical batteries. Nevertheless, our case study provides guidelines for the development of new materials that could go beyond NMC811 and oxide-based SEs.

Summarizing the results of our calculations, we can conclude that the main limiting kinetic factors are as follows: 1) the low effective ionic conductivity in the SE matrix for composite cathodes with low SE mass/volume ratio;<sup>[27]</sup> 2) the resistance at the CAM/SE interface;<sup>[183]</sup> and 3) the low Li-ion chemical diffusion coefficient and long diffusion length in polycrystalline CAM particles.<sup>[121a]</sup> This study demonstrates that the material and processing optimization strategies outlined in this perspective eventually might pave the way to stable, safe LLZO-based SSBs with high specific energy at commercially relevant current densities.

## 8. Conclusions and Future Challenges

In conclusion, detailed understanding and manipulation of both homo- and heterointerfaces and electrode microstructure in oxide-based SSBs is key to unlocking the full potential of this promising class of materials at the full-cell level. Significant research efforts in material synthesis and processing, as well as advanced analysis tools and modeling, are required.

At the materials level, there are still myriad gaps in our knowledge of homointerfaces (e.g., the grain boundaries discussed in Section 2) that limit the correlation between the processing, structure, and properties of the LLZO SE. In-depth knowledge of the microstructural evolution of LLZO during sintering, including pressure-assisted sintering, could enable the tailoring of grain sizes and GB properties to specific functionality in the cell, e.g., dendrite resistance in the case of the separator and low GB resistance in the mixed cathode. For heterointerfaces, advanced processing techniques or routes to obtain crystalline, clean interfaces with low Li-transfer resistances need to be further explored. While the formation of secondary phases can be suppressed to a significant extent, the evolution of the SE/CAM interface during operation needs to be studied in terms of electro-chemo-mechanically induced degradation. The knowledge gained here can lead to remedial strategies, either at the materials level, e.g., via coatings or bulk dopants, or at the operational level of the cell, e.g., by limiting it to upper or lower cutoff potentials for charging and discharging.

In terms of advanced analytical tools, it is of paramount importance to gain direct insight into the electrochemical

degradation phenomena via in situ or even operando studies. While techniques that are sensitive to the chemical environment, such as XPS, Raman spectroscopy, and NMR, are extremely powerful, adequate model systems need to be developed that limit the complexity of the system and allow the relevant dependencies to be extracted under operating conditions. While thin film cells can be fabricated using PLD, PVD, or CVD techniques, the challenge here is to avoid undesirable side reactions and to ensure that the model interfaces are sufficiently similar to those actually fabricated using industrially relevant techniques. Techniques that are insensitive to the chemical environment, such as ion beam (SIMS, NRA, PIXE, PIGE) or neutron (depth profiling) based techniques, often have significant advantages, such as quantification of Li and 2D or even 3D mapping capabilities, and can be applied directly to working state-of-the-art cells. However, without the chemical information at a resolution above the interface dimensions, they need to be combined with chemically sensitive techniques and advanced modeling to obtain a comprehensive understanding of degradation phenomena during operation.

To tie experimental observations and fundamental degradation mechanisms together, complementary modeling across the full range of scales, from the atomic to the component level, is required. While simple DFT structural relaxation methods have dominated the computational landscape to date, a direct dynamical approach using MD or a combined MC-MD approach is required to access relevant time scales and heterogeneous complexity. In addition, interatomic potentials based on various machine-learning models could be an effective way to predict chemical reactions and complex phase diagrams. At the component level, the main challenge is to incorporate the complex microstructures of mixed cathodes and their effects on electrochemical and mechanical properties. By using reconstructed microstructures of real cells as input parameters for continuum modeling, electrochemical performance and electro-chemomechanical stress evolution can be assessed on the component scale.

Validation of the models both on the atomistic scale via interface-sensitive techniques and on the component scale via 2D and 3D mapping provides the necessary foundation for future material and processing development, paving the way for high-performance oxide-based SSBs.

Finally, oxide-based SSBs offer not only a dramatic increase in safety due to the nonflammable electrolyte, but also a dramatic increase in theoretical energy density (>500 Wh kg<sup>-1</sup> with commercial NMC811 and >1000 Wh kg<sup>-1</sup> with future conversion cathodes) compared to state-of-the-art commercial LIBs.

The challenge of practically achieving these energy densities in real cells under high applied current densities remains. As described above, these issues depend on reducing and stabilizing the CAM/LLZO interfacial impedance, optimizing the CAM/LLZO 3D microstructure, and increasing the ionic/electronic conductivity of the cathode composite to achieve higher current densities as the cathode becomes thicker. In addition, our modeling shows that the Li-ion diffusion length in intercalation cathodes is more critical in SSBs than in cells with LE, because the SE will not flow to fill the cracks formed in the CAM particles as is done with a LE. Therefore, smaller CAM particles and/or thin films are necessary to achieve

theoretical energy densities for intercalation cathodes. However, this problem can be circumvented for conversion cathodes with much higher theoretical energy densities.

## Supporting Information

Supporting Information is available from the Wiley Online Library or from the author.

## Acknowledgements

Y.R. and T.D. contributed equally to this work. This work was part of the US-German joint collaboration on "Interfaces and Interphases in Rechargeable Li-Metal Based Batteries: Cathode/Solid Electrolyte (CatSE and CatSE<sup>2</sup>)" supported by the US Department of Energy (DOE) and the German Federal Ministry of Education and Research (BMBF). Financial support from the BMBF under grant numbers 03XP0223 A to E, 3XP0510 A to E, and DOE under the grant numbers DE-ACO5-000R22275, DE-EE0008858 and DE-AC02-06CH11357 is acknowledged. The authors further acknowledge John O'Neill from Maryland Energy Innovation Institute (MEI<sup>2</sup>), University of Maryland (UMD) for creating the battery schematics used in Figure 8a,b. A portion of this work was performed under the auspices of the DOE by Lawrence Livermore National Laboratory under contract DE-AC52-07NA27344.

Open access funding enabled and organized by Projekt DEAL.

## Conflict of Interest

The authors declare no conflict of interest.

## Keywords

ceramic cathode/electrolyte interface, grain boundaries, oxide solid electrolyte, solid state battery

Received: June 8, 2022  
Revised: September 9, 2022  
Published online:

- [1] S. Qin, X. Zhu, Y. Jiang, M. e. Ling, Z. Hu, J. Zhu, *Appl. Phys. Lett.* **2018**, *112*, 113901.
- [2] M. J. Wang, E. Kazyak, N. P. Dasgupta, J. Sakamoto, *Joule* **2021**, *5*, 1371.
- [3] a) Y. Takeda, O. Yamamoto, N. Imanishi, *Electrochemistry* **2016**, *84*, 210; b) J. Lang, L. Qi, Y. Luo, H. Wu, *Energy Storage Mater.* **2017**, *7*, 115; c) D. Lin, Y. Liu, Y. Cui, *Nat. Nanotechnol.* **2017**, *12*, 194; d) S. S. Zhang, *ACS Appl. Energy Mater.* **2018**, *1*, 910; e) Z. A. Ghazi, Z. Sun, C. Sun, F. Qi, B. An, F. Li, H.-M. Cheng, *Small* **2019**, *15*, 1900687; f) T. Krauskopf, F. H. Richter, W. G. Zeier, J. Janek, *Chem. Rev.* **2020**, *120*, 7745; g) R. Wang, W. Cui, F. Chu, F. Wu, *J. Energy Chem.* **2020**, *48*, 145; h) P. Albertus, V. Anandan, C. Ban, N. Balsara, I. Belharouak, J. Buettner-Garrett, Z. Chen, C. Daniel, M. Doeff, N. J. Dudney, B. Dunn, S. J. Harris, S. Herle, E. Herbert, S. Kalnaus, J. A. Libera, D. Lu, S. Martin, B. D. McCloskey, M. T. McDowell, Y. S. Meng, J. Nanda, J. Sakamoto, E. C. Self, S. Tepavcevic, E. Wachsman, C. Wang, A. S. Westover, J. Xiao, T. Yersak, *ACS Energy Lett* **2021**, *6*, 1399.
- [4] G. T. Hitz, D. W. McOwen, L. Zhang, Z. Ma, Z. Fu, Y. Wen, Y. Gong, J. Dai, T. R. Hamann, L. Hu, E. D. Wachsman, *Mater. Today* **2019**, *22*, 50.



- [5] E. Kazyak, R. Garcia-Mendez, W. S. LePage, A. Sharafi, A. L. Davis, A. J. Sanchez, K.-H. Chen, C. Haslam, J. Sakamoto, N. P. Dasgupta, *Mater* **2020**, *2*, 1025.
- [6] a) A. Banerjee, X. Wang, C. Fang, E. A. Wu, Y. S. Meng, *Chem. Rev.* **2020**, *120*, 6878; b) C. Wang, K. Fu, S. P. Kammampata, D. W. McOwen, A. J. Samson, L. Zhang, G. T. Hitz, A. M. Nolan, E. D. Wachsman, Y. Mo, V. Thangadurai, L. Hu, *Chem. Rev.* **2020**, *120*, 4257; c) N. Zhao, W. Khokhar, Z. Bi, C. Shi, X. Guo, L.-Z. Fan, C.-W. Nan, *Joule* **2019**, *3*, 1190; d) Y. Gao, A. M. Nolan, P. Du, Y. Wu, C. Yang, Q. Chen, Y. Mo, S.-H. Bo, *Chem. Rev.* **2020**, *120*, 5954; e) T. Famprikis, P. Canepa, J. A. Dawson, M. S. Islam, C. Masquelier, *Nat. Mater.* **2019**, *18*, 1278; f) Y. Lu, L. Li, Q. Zhang, Z. Niu, J. Chen, *Joule* **2018**, *2*, 1747; g) F. Zheng, M. Kotobuki, S. Song, M. O. Lai, L. Lu, *J. Power Sources* **2018**, *389*, 198; h) S. Lobe, A. Bauer, S. Uhlenbruck, D. Fattakhova-Rohlfing, *Adv. Sci.* **2021**, *8*, 2002044; i) Y. Zhu, J. C. Gonzalez-Rosillo, M. Balaish, Z. D. Hood, K. J. Kim, J. L. M. Rupp, *Nat. Rev. Mater.* **2021**, *6*, 313; j) M. Balaish, J. C. Gonzalez-Rosillo, K. J. Kim, Y. Zhu, Z. D. Hood, J. L. M. Rupp, *Nat. Energy* **2021**, *6*, 227; k) K. J. Kim, M. Balaish, M. Wadaguchi, L. Kong, J. L. M. Rupp, *Adv. Energy Mater.* **2021**, *11*, 2002689; l) K. V. Kravchyk, F. Okur, M. V. Kovalenko, *ACS Energy Lett* **2021**, *6*, 2202; m) R. Ye, M. Ihrig, N. Imanishi, M. Finsterbusch, E. Figgemeier, *ChemSusChem* **2021**, *14*, 4397; n) K. V. Kravchyk, D. T. Karabay, M. V. Kovalenko, *Sci. Rep.* **2022**, *12*, 1177.
- [7] S. Randau, D. A. Weber, O. Kötz, R. Koerver, P. Braun, A. Weber, E. Ivers-Tiffée, T. Adermann, J. Kulisch, W. G. Zeier, F. H. Richter, J. Janek, *Nat. Energy* **2020**, *5*, 259.
- [8] P. Barai, T. Fister, Y. Liang, J. Libera, M. Wolfman, X. Wang, J. Garcia, H. Iddir, V. Srinivasan, *Chem. Mater.* **2021**, *33*, 4337.
- [9] J. G. Connell, T. Fuchs, H. Hartmann, T. Krauskopf, Y. Zhu, J. Sann, R. Garcia-Mendez, J. Sakamoto, S. Tepavcevic, J. Janek, *Chem. Mater.* **2020**, *32*, 10207.
- [10] X. Liu, R. Garcia-Mendez, A. R. Lupini, Y. Cheng, Z. D. Hood, F. Han, A. Sharafi, J. C. Idrobo, N. J. Dudney, C. Wang, C. Ma, J. Sakamoto, M. Chi, *Nat. Mater.* **2021**, *20*, 1485.
- [11] M. Ihrig, M. Finsterbusch, A. M. Laptev, C.-h. Tu, N. T. T. Tran, C.-a. Lin, L.-Y. Kuo, R. Ye, Y. J. Sohn, P. Kaghazchi, S.-k. Lin, D. Fattakhova-Rohlfing, O. Guillon, *ACS Appl. Mater. Interfaces* **2022**, *14*, 11288.
- [12] M. Finsterbusch, T. Danner, C.-L. Tsai, S. Uhlenbruck, A. Latz, O. Guillon, *ACS Appl. Mater. Interfaces* **2018**, *10*, 22329.
- [13] T. W. Heo, A. Grieder, B. Wang, M. Wood, T. Hsu, S. A. Akhade, L. F. Wan, L.-Q. Chen, N. Adelstein, B. C. Wood, *npj Comput. Mater.* **2021**, *7*, 214.
- [14] K. Kim, A. M. Dive, A. C. Grieder, N. Adelstein, S. Kang, L. F. Wan, B. C. Wood, *J. Chem. Phys.* **2022**, *156*, 221101.
- [15] J. Wolfenstine, J. Sakamoto, J. L. Allen, *J. Mater. Sci.* **2012**, *47*, 4428.
- [16] S. Kumazaki, Y. Iriyama, K.-H. Kim, R. Murugan, K. Tanabe, K. Yamamoto, T. Hirayama, Z. Ogumi, *Electrochem. Commun.* **2011**, *13*, 509.
- [17] R. Hongahally Basappa, T. Ito, T. Morimura, R. Bekarevich, K. Mitsuishi, H. Yamada, *J. Power Sources* **2017**, *363*, 145.
- [18] S. Yu, D. J. Siegel, *Chem. Mater.* **2017**, *29*, 9639.
- [19] a) C. Li, Y. Liu, J. He, K. S. Brinkman, *J. Alloys Compd.* **2017**, *695*, 3744; b) G. Han, B. Kinzer, R. Garcia-Mendez, H. Choe, J. Wolfenstine, J. Sakamoto, *J. Eur. Ceram. Soc.* **2020**, *40*, 1999.
- [20] L. Cheng, W. Chen, M. Kunz, K. Persson, N. Tamura, G. Chen, M. Doeff, *ACS Appl. Mater. Interfaces* **2015**, *7*, 2073.
- [21] A. Sharafi, C. G. Haslam, R. D. Kerns, J. Wolfenstine, J. Sakamoto, *J. Mater. Chem. A* **2017**, *5*, 21491.
- [22] H. Shiiba, N. Zettsu, M. Yamashita, H. Onodera, R. Jalem, M. Nakayama, K. Teshima, *J. Phys. Chem. C* **2018**, *122*, 21755.
- [23] a) S. Braun, C. Yada, A. Latz, *J. Phys. Chem. C* **2015**, *119*, 22281; b) C.-C. Chen, J. Maier, *Phys. Chem. Chem. Phys.* **2017**, *19*, 6379; c) G. Gregori, R. Merkle, J. Maier, *Prog. Mater. Sci.* **2017**, *89*, 252; d) M. Landstorfer, S. Funken, T. Jacob, *Phys. Chem. Chem. Phys.* **2011**, *13*, 12817.
- [24] a) B. J. Morgan, *R. Soc. Open Sci.* **2017**, *4*, 170824; b) T. H. Wan, F. Ciucci, *Electrochim. Acta* **2020**, *331*, 135355; c) K. Becker-Steinberger, S. Schardt, B. Horstmann, A. Latz, (Preprint) arXiv:2101.10294, v1, submitted: Jan 2021.
- [25] B. Kozinsky, S. A. Akhade, P. Hirel, A. Hashibon, C. Elsässer, P. Mehta, A. Logeat, U. Eisele, *Phys. Rev. Lett.* **2016**, *116*, 055901.
- [26] a) F. Shen, M. B. Dixit, X. Xiao, K. B. Hatzell, *ACS Energy Lett.* **2018**, *3*, 1056; b) M. B. Dixit, M. Regala, F. Shen, X. Xiao, K. B. Hatzell, *ACS Appl. Mater. Interfaces* **2019**, *11*, 2022; c) T. Hamann, L. Zhang, Y. Gong, G. Godbey, J. Gritton, D. McOwen, G. Hitz, E. Wachsman, *Adv. Funct. Mater.* **2020**, *30*, 1910362.
- [27] A. Neumann, T. R. Hamann, T. Danner, S. Hein, K. Becker-Steinberger, E. Wachsman, A. Latz, *ACS Appl. Energy Mater.* **2021**, *4*, 4786.
- [28] a) L. Cheng, J. S. Park, H. Hou, V. Zorba, G. Chen, T. Richardson, J. Cabana, R. Russo, M. Doeff, *J. Mater. Chem. A* **2014**, *2*, 172; b) I. N. David, T. Thompson, J. Wolfenstine, J. L. Allen, J. Sakamoto, *J. Am. Ceram. Soc.* **2015**, *98*, 1209; c) Y. Kim, H. Jo, J. L. Allen, H. Choe, J. Wolfenstine, J. Sakamoto, *J. Am. Ceram. Soc.* **2016**, *99*, 1367; d) B. Xu, H. Duan, W. Xia, Y. Guo, H. Kang, H. Li, H. Liu, *J. Power Sources* **2016**, *302*, 291.
- [29] A. N. Mistry, K. Smith, P. P. Mukherjee, *ACS Appl. Mater. Interfaces* **2018**, *10*, 6317.
- [30] F. L. E. Usseglio-Viretta, A. Colclasure, A. N. Mistry, K. P. Y. Claver, F. Pouraghajan, D. P. Finegan, T. M. M. Heenan, D. Abraham, P. P. Mukherjee, D. Wheeler, P. Shearing, S. J. Cooper, K. Smith, *J. Electrochem. Soc.* **2018**, *165*, A3403.
- [31] a) R. V. Rao, V. Patel, *Sci. Iran.* **2013**, *20*, 710; b) K. J. Harry, K. Higa, V. Srinivasan, N. P. Balsara, *J. Electrochem. Soc.* **2016**, *163*, A2216.
- [32] A. Neumann, S. Randau, K. Becker-Steinberger, T. Danner, S. Hein, Z. Ning, J. Marrow, F. H. Richter, J. Janek, A. Latz, *ACS Appl. Mater. Interfaces* **2020**, *12*, 9277.
- [33] T. Shi, Q. Tu, Y. Tian, Y. Xiao, L. J. Miara, O. Kononova, G. Ceder, *Adv. Energy Mater.* **2020**, *10*, 1902881.
- [34] H.-K. Tian, Z. Liu, Y. Ji, L.-Q. Chen, Y. Qi, *Chem. Mater.* **2019**, *31*, 7351.
- [35] a) P. Barai, K. Higa, A. T. Ngo, L. A. Curtiss, V. Srinivasan, *J. Electrochem. Soc.* **2019**, *166*, A1752; b) P. Barai, A. T. Ngo, B. Narayanan, K. Higa, L. A. Curtiss, V. Srinivasan, *J. Electrochem. Soc.* **2020**, *167*, 100537.
- [36] Y. Suzuki, K. Kami, K. Watanabe, A. Watanabe, N. Saito, T. Ohnishi, K. Takada, R. Sudo, N. Imanishi, *Solid State Ionics* **2015**, *278*, 172.
- [37] Y. Ren, Y. Shen, Y. Lin, C.-W. Nan, *Electrochem. Commun.* **2015**, *57*, 27.
- [38] S. Jeff, R. Ezhiylmurugan, K. Hyunjoong, K. Yunsung, W. Jeff, *Nanotechnology* **2013**, *24*, 424005.
- [39] M. Wood, X. Gao, R. Shi, T. W. Heo, J. A. Espitia, E. B. Duoss, B. C. Wood, J. Ye, *J. Power Sources* **2021**, *484*, 229252.
- [40] R. Shi, M. Wood, T. W. Heo, B. C. Wood, J. Ye, *J. Eur. Ceram. Soc.* **2021**, *41*, 211.
- [41] R.-H. Shin, S.-I. Son, S.-M. Lee, Y. S. Han, Y. D. Kim, S.-S. Ryu, *J. Korean Ceram. Soc* **2016**, *53*, 712.
- [42] a) A. Logeat, T. Köhler, U. Eisele, B. Stiaszny, A. Harzer, M. Tovar, A. Senyshyn, H. Ehrenberg, B. Kozinsky, *Solid State Ionics* **2012**, *206*, 33; b) T. Thompson, A. Sharafi, M. D. Johannes, A. Huq, J. L. Allen, J. Wolfenstine, J. Sakamoto, *Adv. Energy Mater.* **2015**, *5*, 1500096; c) M. Yi, T. Liu, X. Wang, J. Li, C. Wang, Y. Mo, *Ceram. Int.* **2019**, *45*, 786.
- [43] a) S. Ohta, T. Kobayashi, J. Seki, T. Asaoka, *J. Power Sources* **2012**, *202*, 332; b) X. Tong, V. Thangadurai, E. D. Wachsman, *Inorg. Chem.* **2015**, *54*, 3600.
- [44] a) C. A. Geiger, E. Alekseev, B. Lazic, M. Fisch, T. Armbruster, R. Langner, M. Fechtelkord, N. Kim, T. Pettke, W. Weppner,

- Inorg. Chem.* **2010**, *50*, 1089; b) Y. Jin, P. J. McGinn, *J. Power Sources* **2011**, *196*, 8683; c) Y. Shimonishi, A. Toda, T. Zhang, A. Hirano, N. Imanishi, O. Yamamoto, Y. Takeda, *Solid State Ionics* **2011**, *183*, 48; d) H. Buschmann, J. Dolle, S. Berendts, A. Kuhn, P. Bottke, M. Wilkening, P. Heitjans, A. Senyshyn, H. Ehrenberg, A. Lotnyk, V. Duppel, L. Kienle, J. Janek, *Phys. Chem. Chem. Phys.* **2011**, *13*, 19378; e) E. Rangasamy, J. Wolfenstine, J. Sakamoto, *Solid State Ionics* **2012**, *206*, 28.
- [45] a) J. L. Allen, J. Wolfenstine, E. Rangasamy, J. Sakamoto, *J. Power Sources* **2012**, *206*, 315; b) H. El Shinawi, J. Janek, *J. Power Sources* **2013**, *225*, 13; c) D. Rettenwander, J. Langer, W. Schmidt, C. Arner, K. J. Harris, V. Terskikh, G. R. Goward, M. Wilkening, G. Amthauer, *Chem. Mater.* **2015**, *27*, 3135; d) J. Su, X. Huang, Z. Song, T. Xiu, M. E. Badding, J. Jin, Z. Wen, *Ceram. Int.* **2019**, *45*, 14991.
- [46] L. Cheng, E. J. Crumlin, W. Chen, R. Qiao, H. Hou, S. F. Lux, V. Zorba, R. Russo, R. Kostecki, Z. Liu, K. Persson, W. Yang, J. Cabana, T. Richardson, G. Chen, M. Doeff, *Phys. Chem. Chem. Phys.* **2014**, *16*, 18294.
- [47] W. Xue, Y. Yang, Q. Yang, Y. Liu, L. Wang, C. Chen, R. Cheng, *RSC Adv.* **2018**, *8*, 13083.
- [48] A. Paoletta, W. Zhu, G. Bertoni, S. Savoie, Z. Feng, H. Demers, V. Gariepy, G. Girard, E. Rivard, N. Delaporte, A. Guerfi, H. Lorrmann, C. George, K. Zaghbi, *ACS Appl. Energy Mater.* **2020**, *3*, 3415.
- [49] X. Huang, Y. Lu, Z. Song, K. Rui, Q. Wang, T. Xiu, M. E. Badding, Z. Wen, *Energy Storage Mater.* **2019**, *22*, 207.
- [50] R. Murugan, V. Thangadurai, W. Weppner, *Angew. Chem., Int. Ed.* **2007**, *46*, 7778.
- [51] W. E. Tenhaeff, E. Rangasamy, Y. Wang, A. P. Sokolov, J. Wolfenstine, J. Sakamoto, N. J. Dudney, *ChemElectroChem* **2014**, *1*, 375.
- [52] S. Ohta, T. Kobayashi, T. Asaoka, *J. Power Sources* **2011**, *196*, 3342.
- [53] a) R. A. Huggins, *Ionics* **2002**, *8*, 300; b) J. T. S. Irvine, D. C. Sinclair, A. R. West, *Adv. Mater.* **1990**, *2*, 132; c) J. K. Eckhardt, S. Burkhardt, J. Zahnow, M. T. Elm, J. Janek, P. J. Klar, C. Heiliger, *J. Electrochem. Soc.* **2021**, *168*, 090516.
- [54] J. Haruyama, K. Sodeyama, L. Han, K. Takada, Y. Tateyama, *Chem. Mater.* **2014**, *26*, 4248.
- [55] V. Thangadurai, S. Narayanan, D. Pinzaru, *Chem. Soc. Rev.* **2014**, *43*, 4714.
- [56] a) Y. Zhu, X. He, Y. Mo, *J. Mater. Chem. A* **2016**, *4*, 3253; b) Y. Xiao, L. J. Miara, Y. Wang, G. Ceder, *Joule* **2019**, *3*, 1252; c) L. J. Miara, W. D. Richards, Y. E. Wang, G. Ceder, *Chem. Mater.* **2015**, *27*, 4040; d) L. Miara, A. Windmüller, C.-L. Tsai, W. D. Richards, Q. Ma, S. Uhlenbruck, O. Guillon, G. Ceder, *ACS Appl. Mater. Interfaces* **2016**, *8*, 26842; e) N. Zhang, X. Long, Z. Wang, P. Yu, F. Han, J. Fu, G. Ren, Y. Wu, S. Zheng, W. Huang, C. Wang, H. Li, X. Liu, *ACS Appl. Energy Mater.* **2018**, *1*, 5968; f) Y. Okuno, J. Haruyama, Y. Tateyama, *ACS Appl. Energy Mater.* **2020**, *3*, 11061; g) A. M. Nolan, E. D. Wachsman, Y. Mo, *Energy Storage Mater.* **2021**, *41*, 571.
- [57] Y. Ren, T. Liu, Y. Shen, Y. Lin, C.-W. Nan, *J. Materiomics* **2016**, *2*, 256.
- [58] S. Afyon, F. Krumeich, J. L. M. Rupp, *J. Mater. Chem. A* **2015**, *3*, 18636.
- [59] V. Thangadurai, W. Weppner, *J. Power Sources* **2005**, *142*, 339.
- [60] K. H. Kim, Y. Iriyama, K. Yamamoto, S. Kumazaki, T. Asaka, K. Tanabe, C. A. J. Fisher, T. Hirayama, R. Murugan, Z. Ogumi, *J. Power Sources* **2011**, *196*, 764.
- [61] M. Kotobuki, K. Kanamura, Y. Sato, T. Yoshida, *J. Power Sources* **2011**, *196*, 7750.
- [62] K. Park, B.-C. Yu, J.-W. Jung, Y. Li, W. Zhou, H. Gao, S. Son, J. B. Goodenough, *Chem. Mater.* **2016**, *28*, 8051.
- [63] J. Wakasugi, H. Munakata, K. Kanamura, *Electrochemistry* **2017**, *85*, 77.
- [64] G. Vardar, W. J. Bowman, Q. Lu, J. Wang, R. J. Chater, A. Aguadero, R. Seibert, J. Terry, A. Hunt, I. Waluyo, D. D. Fong, A. Jarry, E. J. Crumlin, S. L. Hellstrom, Y.-M. Chiang, B. Yildiz, *Chem. Mater.* **2018**, *30*, 6259.
- [65] Y. Kim, D. Kim, R. Bliem, G. Vardar, I. Waluyo, A. Hunt, J. T. Wright, J. P. Katsoudas, B. Yildiz, *Chem. Mater.* **2020**, *32*, 9531.
- [66] Y. Kim, I. Waluyo, A. Hunt, B. Yildiz, *Adv. Energy Mater.* **2022**, *12*, 2102741.
- [67] X. Guo, L. Hao, Y. Yang, Y. Wang, Y. Lu, H. Yu, *J. Mater. Chem. A* **2019**, *7*, 25915.
- [68] J. Sastre, X. Chen, A. Aribia, A. N. Tiwari, Y. E. Romanyuk, *ACS Appl. Mater. Interfaces* **2020**, *12*, 36196.
- [69] Y. Ren, E. D. Wachsman, *J. Electrochem. Soc.* **2022**, *169*, 040529.
- [70] S. Narayanan, F. Ramezanipour, V. Thangadurai, *J. Phys. Chem. C* **2012**, *116*, 20154.
- [71] a) S. Lobe, C. Dellen, A. Windmüller, C. L. Tsai, F. Vondahlen, S. Uhlenbruck, O. Guillon, *Ionics* **2018**, *24*, 2199; b) E. A. Il'ina, A. A. Raskovalov, *Electrochim. Acta* **2020**, *330*, 135220.
- [72] S. Uhlenbruck, J. Dornseiffer, S. Lobe, C. Dellen, C.-L. Tsai, B. Gotzen, D. Sebold, M. Finsterbusch, O. Guillon, *J. Electroceram.* **2017**, *38*, 197.
- [73] S. Panahian Jand, P. Kaghazchi, *MRS Commun.* **2018**, *8*, 591.
- [74] T. Pan, J. Alvarado, J. Zhu, Y. Yue, H. L. Xin, D. Nordlund, F. Lin, M. M. Doeff, *J. Electrochem. Soc.* **2019**, *166*, A1964.
- [75] M. Zarabian, M. Bartolini, P. Pereira-Almao, V. Thangadurai, *J. Electrochem. Soc.* **2017**, *164*, A1133.
- [76] a) H. Wakayama, H. Yonekura, Y. Kawai, *Chem. Mater.* **2016**, *28*, 4453; b) H. Wakayama, Y. Kawai, *J. Mater. Chem. A* **2017**, *5*, 18816.
- [77] Y. U. Wang, *Acta Mater.* **2006**, *54*, 953.
- [78] T. F. Flint, Y. L. Sun, Q. Xiong, M. C. Smith, J. A. Francis, *Sci. Rep.* **2019**, *9*, 18426.
- [79] C. Park, S. Lee, K. Kim, M. Kim, S. Choi, D. Shin, *J. Electrochem. Soc.* **2019**, *166*, A5318.
- [80] K. Wu, *Doctor Thesis*, The Ohio State University **2003**.
- [81] E. J. Cheng, K. Hong, N. J. Taylor, H. Choe, J. Wolfenstine, J. Sakamoto, *J. Eur. Ceram. Soc.* **2017**, *37*, 3213.
- [82] H.-C. Yu, D. Taha, T. Thompson, N. J. Taylor, A. Drews, J. Sakamoto, K. Thornton, *J. Power Sources* **2019**, *440*, 227116.
- [83] C.-L. Tsai, Q. Ma, C. Dellen, S. Lobe, F. Vondahlen, A. Windmüller, D. Grüner, H. Zheng, S. Uhlenbruck, M. Finsterbusch, F. Tietz, D. Fattakhova-Rohlfing, H. P. Buchkremer, O. Guillon, *Sustainable Energy Fuels* **2019**, *3*, 280.
- [84] a) S. Lamowski, S. Schmerler, J. Kutzner, J. Kortus, *Steel Res. Int.* **2011**, *82*, 1129; b) E. T. Ritz, S. J. Li, N. A. Benedek, *J. Appl. Phys.* **2019**, *126*, 171102.
- [85] S. O. Dang, *Doctor Thesis*, RWTH Aachen University **2015**.
- [86] a) A. A. Hubaud, D. J. Schroeder, B. J. Ingram, J. S. Okasinski, J. T. Vaughney, *J. Alloys Compd.* **2015**, *644*, 804; b) M. Bertrand, S. Rousselot, D. Aymé-Perrot, M. Dollé, *Mater. Adv.* **2021**, *2*, 2989.
- [87] a) E. J. Cheng, N. J. Taylor, J. Wolfenstine, J. Sakamoto, *J. Asian Ceram. Soc.* **2017**, *5*, 113; b) K. Mukai, Y. Kishida, H. Nozaki, K. Dohmae, *J. Power Sources* **2013**, *224*, 230.
- [88] J. Wolfenstine, J. L. Allen, J. Sakamoto, D. J. Siegel, H. Choe, *Ionics* **2018**, *24*, 1271.
- [89] H.-K. Tian, A. Chakraborty, A. A. Talin, P. Eisenlohr, Y. Qi, *J. Electrochem. Soc.* **2020**, *167*, 090541.
- [90] A. Jain, S. P. Ong, G. Hautier, W. Chen, W. D. Richards, S. Dacek, S. Cholia, D. Gunter, D. Skinner, G. Ceder, K. A. Persson, *APL Mater.* **2013**, *1*, 011002.
- [91] a) S. Ohta, S. Komagata, J. Seki, T. Saeki, S. Morishita, T. Asaoka, *J. Power Sources* **2013**, *238*, 53; b) B. Ramkumar, K. So-young, N. Chan-woo, V. Aravindan, L. Yun-Sung, *Electrochim. Acta* **2020**, *359*, 136955; c) R. Balasubramaniam, C.-W. Nam, V. Aravindan, D. Eum, K. Kang, Y.-S. Lee, *ChemElectroChem* **2021**, *8*, 570.
- [92] George V. Alexander, N. C. Rosero-Navarro, A. Miura, K. Tadanaga, R. Murugan, *J. Mater. Chem. A* **2018**, *6*, 21018.

- [93] Z. Zhao, Z. Wen, X. Liu, H. Yang, S. Chen, C. Li, H. Lv, F. Wu, B. Wu, D. Mu, *Chem. Eng. J.* **2021**, 405, 127031.
- [94] a) S. Ohta, J. Seki, Y. Yagi, Y. Kihira, T. Tani, T. Asaoka, *J. Power Sources* **2014**, 265, 40; b) T. Liu, Y. Ren, Y. Shen, S.-X. Zhao, Y. Lin, C.-W. Nan, *J. Power Sources* **2016**, 324, 349; c) C. Roitzheim, Y. J. Sohn, L.-Y. Kuo, G. Häuschen, M. Mann, D. Sebold, M. Finsterbusch, P. Kaghazchi, O. Guillon, D. Fattakhova-Rohlfing, *ACS Appl. Energy Mater.* **2022**, 5, 6913.
- [95] F. Han, J. Yue, C. Chen, N. Zhao, X. Fan, Z. Ma, T. Gao, F. Wang, X. Guo, C. Wang, *Joule* **2018**, 2, 497.
- [96] A. M. Laptev, H. Zheng, M. Bram, M. Finsterbusch, O. Guillon, *Mater. Lett.* **2019**, 247, 155.
- [97] Y. K. Lee, J. Park, W. Lu, *J. Electrochem. Soc.* **2019**, 166, A1340.
- [98] A. M. Nolan, Y. Liu, Y. Mo, *ACS Energy Lett.* **2019**, 4, 2444.
- [99] D. Wang, Q. Sun, J. Luo, J. Liang, Y. Sun, R. Li, K. Adair, L. Zhang, R. Yang, S. Lu, H. Huang, X. Sun, *ACS Appl. Mater. Interfaces* **2019**, 11, 4954.
- [100] a) H. Schmalzried, J. Janek, *Ber. Bunsen-Ges. Phys. Chem.* **1998**, 102, 127; b) J. Janek, *Nova Acta Leopold. NF* **2000**, 83, 175.
- [101] N. J. J. de Klerk, M. Wagemaker, *ACS Appl. Energy Mater.* **2018**, 1, 5609.
- [102] C. Ma, Y. Cheng, K. Chen, J. Li, B. G. Sumpter, C.-W. Nan, K. L. More, N. J. Dudley, M. Chi, *Adv. Energy Mater.* **2016**, 6, 1600053.
- [103] R. Koerver, I. Aygün, T. Leichtweiß, C. Dietrich, W. Zhang, J. O. Binder, P. Hartmann, W. G. Zeier, J. Janek, *Chem. Mater.* **2017**, 29, 5574.
- [104] M. Rosen, M. Finsterbusch, O. Guillon, D. Fattakhova-Rohlfing, *J. Mater. Chem. A* **2022**, 10, 2320.
- [105] M. Ihrig, M. Finsterbusch, C.-L. Tsai, A. M. Laptev, C.-h. Tu, M. Bram, Y. J. Sohn, R. Ye, S. Sevinc, S.-k. Lin, D. Fattakhova-Rohlfing, O. Guillon, *J. Power Sources* **2021**, 482, 228905.
- [106] A. A. Delluva, J. Dudoff, G. Teeter, A. Holewinski, *ACS Appl. Mater. Interfaces* **2020**, 12, 24992.
- [107] R. Koerver, W. Zhang, L. de Biasi, S. Schweidler, A. O. Kondrakov, S. Kolling, T. Brezesinski, P. Hartmann, W. G. Zeier, J. Janek, *Energy Environ. Sci.* **2018**, 11, 2142.
- [108] R. Mücke, M. Finsterbusch, P. Kaghazchi, D. Fattakhova-Rohlfing, O. Guillon, *J. Power Sources* **2021**, 489, 229430.
- [109] J. B. Goodenough, K.-S. Park, *J. Am. Chem. Soc.* **2013**, 135, 1167.
- [110] W. D. Richards, L. J. Miara, Y. Wang, J. C. Kim, G. Ceder, *Chem. Mater.* **2016**, 28, 266.
- [111] T. K. Schwietert, V. A. Arszewska, C. Wang, C. Yu, A. Vasileiadis, N. J. J. de Klerk, J. Hageman, T. Hupfer, I. Kerkamm, Y. Xu, E. van der Maas, E. M. Kelder, S. Ganapathy, M. Wagemaker, *Nat. Mater.* **2020**, 19, 428.
- [112] a) J. Christensen, J. Newman, *J. Electrochem. Soc.* **2004**, 151, A1977; b) V. Battaglia, J. Newman, *J. Electrochem. Soc.* **1995**, 142, 1423.
- [113] W. Zhang, D. Schröder, T. Arlt, I. Manke, R. Koerver, R. Pinedo, D. A. Weber, J. Sann, W. G. Zeier, J. Janek, *J. Mater. Chem. A* **2017**, 5, 9929.
- [114] P. Li, Y. Zhao, Y. Shen, S.-H. Bo, *J. Phys. Energy* **2020**, 2, 022002.
- [115] H.-K. Tian, B. Xu, Y. Qi, *J. Power Sources* **2018**, 392, 79.
- [116] K. Tantratian, H. Yan, K. Ellwood, E. T. Harrison, L. Chen, *Adv. Energy Mater.* **2021**, 11, 2003417.
- [117] H. Mendoza, S. A. Roberts, V. E. Brunini, A. M. Grillet, *Electrochim. Acta* **2016**, 190, 1.
- [118] R. Xu, H. Sun, L. S. de Vasconcelos, K. Zhao, *J. Electrochem. Soc.* **2017**, 164, A3333.
- [119] a) S. Xia, L. Mu, Z. Xu, J. Wang, C. Wei, L. Liu, P. Pianetta, K. Zhao, X. Yu, F. Lin, Y. Liu, *Nano Energy* **2018**, 53, 753; b) D. J. Miller, C. Proff, J. G. Wen, D. P. Abraham, J. Bareño, *Adv. Energy Mater.* **2013**, 3, 1098.
- [120] P. Liu, R. Xu, Y. Liu, F. Lin, K. Zhao, *J. Electrochem. Soc.* **2020**, 167, 040527.
- [121] a) R. Ruess, S. Schweidler, H. Hemmelmann, G. Conforto, A. Bielefeld, D. A. Weber, J. Sann, M. T. Elm, J. Janek, *J. Electrochem. Soc.* **2020**, 167, 100532; b) E. Trevisanello, R. Ruess, G. Conforto, F. H. Richter, J. Janek, *Adv. Energy Mater.* **2021**, 11, 2003400.
- [122] M. M. Besli, S. Xia, S. Kuppan, Y. Huang, M. Metzger, A. K. Shukla, G. Schneider, S. Hellstrom, J. Christensen, M. M. Doeff, Y. Liu, *Chem. Mater.* **2019**, 31, 491.
- [123] P. Minnmann, L. Quillman, S. Burkhardt, F. H. Richter, J. Janek, *J. Electrochem. Soc.* **2021**, 168, 040537.
- [124] F. Hao, P. P. Mukherjee, *J. Electrochem. Soc.* **2018**, 165, A1857.
- [125] J. Ast, M. Ghidelli, K. Durst, M. Göken, M. Sebastiani, A. M. Korsunsky, *Mater. Des.* **2019**, 173, 107762.
- [126] G. Bucci, B. Talamini, A. Renuka Balakrishna, Y.-M. Chiang, W. C. Carter, *Phys. Rev. Mater.* **2018**, 2, 105407.
- [127] P. Barai, T. Rojas, B. Narayanan, A. T. Ngo, L. A. Curtiss, V. Srinivasan, *Chem. Mater.* **2021**, 33, 5527.
- [128] F. Hippauf, B. Schumm, S. Doerfler, H. Althues, S. Fujiki, T. Shiratsuchi, T. Tsujimura, Y. Aihara, S. Kaskel, *Energy Storage Mater.* **2019**, 21, 390.
- [129] a) K. Fu, Y. Gong, G. T. Hitz, D. W. McOwen, Y. Li, S. Xu, Y. Wen, L. Zhang, C. Wang, G. Pastel, J. Dai, B. Liu, H. Xie, Y. Yao, E. D. Wachsman, L. Hu, *Energy Environ. Sci.* **2017**, 10, 1568; b) S. Xu, D. W. McOwen, L. Zhang, G. T. Hitz, C. Wang, Z. Ma, C. Chen, W. Luo, J. Dai, Y. Kuang, E. M. Hitz, K. Fu, Y. Gong, E. D. Wachsman, L. Hu, *Energy Storage Mater.* **2018**, 15, 458.
- [130] H. Stöffler, T. Zinkevich, M. Yavuz, A.-L. Hansen, M. Knapp, J. Bednarčík, S. Randau, F. H. Richter, J. Janek, H. Ehrenberg, S. Indris, *J. Phys. Chem. C* **2019**, 123, 10280.
- [131] T. Ates, A. Neumann, T. Danner, A. Latz, M. Zarrabeitia, D. Stepien, A. Varzi, S. Passerini, *Adv. Sci.* **2022**, 9, 2105234.
- [132] H. Stöffler, T. Zinkevich, M. Yavuz, A. Senyshyn, J. Kulisch, P. Hartmann, T. Adermann, S. Randau, F. H. Richter, J. Janek, S. Indris, H. Ehrenberg, *J. Phys. Chem. C* **2018**, 122, 15954.
- [133] S. Wang, W. Zhang, X. Chen, D. Das, R. Ruess, A. Gautam, F. Walther, S. Ohno, R. Koerver, Q. Zhang, W. G. Zeier, F. H. Richter, C.-W. Nan, J. Janek, *Adv. Energy Mater.* **2021**, 11, 2100654.
- [134] D. Devaux, R. Bouchet, D. Glé, R. Denoyel, *Solid State Ionics* **2012**, 227, 119.
- [135] M. A. Kraft, S. Ohno, T. Zinkevich, R. Koerver, S. P. Culver, T. Fuchs, A. Senyshyn, S. Indris, B. J. Morgan, W. G. Zeier, *J. Am. Chem. Soc.* **2018**, 140, 16330.
- [136] S. Yu, R. D. Schmidt, R. Garcia-Mendez, E. Herbert, N. J. Dudley, J. B. Wolfenstine, J. Sakamoto, D. J. Siegel, *Chem. Mater.* **2016**, 28, 197.
- [137] Z. Deng, Z. Wang, I.-H. Chu, J. Luo, S. P. Ong, *J. Electrochem. Soc.* **2015**, 163, A67.
- [138] E. G. Herbert, W. E. Tenhaeff, N. J. Dudley, G. M. Pharr, *Thin Solid Films* **2011**, 520, 413.
- [139] J. Janek, W. G. Zeier, *Nat. Energy* **2016**, 1, 16141.
- [140] S. H. Jung, U.-H. Kim, J.-H. Kim, S. Jun, C. S. Yoon, Y. S. Jung, Y.-K. Sun, *Adv. Energy Mater.* **2020**, 10, 1903360.
- [141] a) Y. Zhu, X. He, Y. Mo, *ACS Appl. Mater. Interfaces* **2015**, 7, 23685; b) G. F. Dewald, S. Ohno, M. A. Kraft, R. Koerver, P. Till, N. M. Vargas-Barbosa, J. Janek, W. G. Zeier, *Chem. Mater.* **2019**, 31, 8328.
- [142] a) F. Walther, R. Koerver, T. Fuchs, S. Ohno, J. Sann, M. Rohnke, W. G. Zeier, J. Janek, *Chem. Mater.* **2019**, 31, 3745; b) F. Walther, S. Randau, Y. Schneider, J. Sann, M. Rohnke, F. H. Richter, W. G. Zeier, J. Janek, *Chem. Mater.* **2020**, 32, 6123; c) F. Walther, F. Strauss, X. Wu, B. Mogwitz, J. Hertle, J. Sann, M. Rohnke, T. Brezesinski, J. Janek, *Chem. Mater.* **2021**, 33, 2110.
- [143] R. Koerver, F. Walther, I. Aygün, J. Sann, C. Dietrich, W. G. Zeier, J. Janek, *J. Mater. Chem. A* **2017**, 5, 22750.
- [144] A. Sakuda, A. Hayashi, M. Tatsumisago, *Chem. Mater.* **2010**, 22, 949.



- [145] J. Haruyama, K. Sodeyama, Y. Tateyama, *ACS Appl. Mater. Interfaces* **2017**, *9*, 286.
- [146] a) X. Li, J. Liang, J. Luo, M. Norouzi Banis, C. Wang, W. Li, S. Deng, C. Yu, F. Zhao, Y. Hu, T.-K. Sham, L. Zhang, S. Zhao, S. Lu, H. Huang, R. Li, K. R. Adair, X. Sun, *Energy Environ. Sci.* **2019**, *12*, 2665; b) X. Li, J. Liang, N. Chen, J. Luo, K. R. Adair, C. Wang, M. N. Banis, T.-K. Sham, L. Zhang, S. Zhao, S. Lu, H. Huang, R. Li, X. Sun, *Angew. Chem., Int. Ed.* **2019**, *58*, 16427.
- [147] L. M. Riegger, R. Schlem, J. Sann, W. G. Zeier, J. Janek, *Angew. Chem., Int. Ed.* **2021**, *60*, 6718.
- [148] D. Cao, Y. Zhang, A. M. Nolan, X. Sun, C. Liu, J. Sheng, Y. Mo, Y. Wang, H. Zhu, *Nano Lett.* **2020**, *20*, 1483.
- [149] P. Braun, C. Uhlmann, M. Weiss, A. Weber, E. Ivers-Tiffée, *J. Power Sources* **2018**, *393*, 119.
- [150] D. Danilov, R. A. H. Niessen, P. H. L. Notten, *J. Electrochem. Soc.* **2011**, *158*, A215.
- [151] a) A. Bielefeld, D. A. Weber, J. Janek, *J. Phys. Chem. C* **2019**, *123*, 1626; b) A. Bielefeld, D. A. Weber, J. Janek, *ACS Appl. Mater. Interfaces* **2020**, *12*, 12821.
- [152] H. Shen, E. Yi, M. Amores, L. Cheng, N. Tamura, D. Y. Parkinson, G. Chen, K. Chen, M. Doeff, *J. Mater. Chem. A* **2019**, *7*, 20861.
- [153] a) H. Chen, Q.-y. Liu, M.-x. Jing, F. Chen, W.-y. Yuan, B.-w. Ju, F.-y. Tu, X.-q. Shen, S.-b. Qin, *ACS Appl. Mater. Interfaces* **2020**, *12*, 15120; b) Q. Guo, F. Xu, L. Shen, S. Deng, Z. Wang, M. Li, X. Yao, *Energy Mater. Adv.* **2022**, *2022*, 9753506.
- [154] a) Z. Li, H.-X. Xie, X.-Y. Zhang, X. Guo, *J. Mater. Chem. A* **2020**, *8*, 3892; b) K. Liu, X. Li, J. Cai, Z. Yang, Z. Chen, B. Key, Z. Zhang, T. L. Dzwiniel, C. Liao, *ACS Energy Lett.* **2021**, *6*, 1315.
- [155] B. Liu, L. Zhang, S. Xu, D. W. McOwen, Y. Gong, C. Yang, G. R. Pastel, H. Xie, K. Fu, J. Dai, *Energy Storage Mater.* **2018**, *14*, 376.
- [156] A. Gupta, E. Kazyak, N. P. Dasgupta, J. Sakamoto, *J. Power Sources* **2020**, *474*, 228598.
- [157] J. Liu, X. Gao, G. O. Hartley, G. J. Rees, C. Gong, F. H. Richter, J. Janek, Y. Xia, A. W. Robertson, L. R. Johnson, P. G. Bruce, *Joule* **2020**, *4*, 101.
- [158] Y. Xie, H. Gao, J. Gim, A. T. Ngo, Z.-F. Ma, Z. Chen, *J. Phys. Chem. Lett.* **2019**, *10*, 589.
- [159] C.-C. Su, M. He, R. Amine, Z. Chen, Z. Yu, T. Rojas, L. Cheng, A. T. Ngo, K. Amine, *Nano Energy* **2021**, *83*, 105843.
- [160] A. Gupta, J. Sakamoto, *Electrochem. Soc. Interface* **2019**, *28*, 63.
- [161] J. Tong, S. Wu, N. Von Solms, X. Liang, F. Huo, Q. Zhou, H. He, S. Zhang, *Front. Chem.* **2020**, *7*, 945.
- [162] B. Xu, H. Duan, H. Liu, C. A. Wang, S. Zhong, *ACS Appl. Mater. Interfaces* **2017**, *9*, 21077.
- [163] W. Zhou, Z. Wang, Y. Pu, Y. Li, S. Xin, X. Li, J. Chen, J. B. Goodenough, *Adv. Mater.* **2019**, *31*, 1805574.
- [164] X. Pan, H. Sun, Z. Wang, H. Huang, Q. Chang, J. Li, J. Gao, S. Wang, H. Xu, Y. Li, *Adv. Energy Mater.* **2020**, *10*, 2002416.
- [165] K. Liu, Z. Wang, L. Shi, S. Jungstuttwong, S. Yuan, *J. Energy Chem.* **2021**, *59*, 320.
- [166] M. Chen, J. Wu, T. Ye, J. Ye, C. Zhao, S. Bi, J. Yan, B. Mao, G. Feng, *Nat. Commun.* **2020**, *11*, 5809.
- [167] J.-Y. Liang, X.-X. Zeng, X.-D. Zhang, P.-F. Wang, J.-Y. Ma, Y.-X. Yin, X.-W. Wu, Y.-G. Guo, L.-J. Wan, *J. Am. Chem. Soc.* **2018**, *140*, 6767.
- [168] C. Zhan, T. Wu, J. Lu, K. Amine, *Energy Environ. Sci.* **2018**, *11*, 243.
- [169] N. R. Vadivel, S. Ha, M. He, D. Dees, S. Trask, B. Polzin, K. G. Gallagher, *J. Electrochem. Soc.* **2017**, *164*, A508.
- [170] D. Kim, S. Park, O. B. Chae, J. H. Ryu, Y.-U. Kim, R.-Z. Yin, S. M. Oh, *J. Electrochem. Soc.* **2011**, *159*, A193.
- [171] K. Leung, *Chem. Mater.* **2017**, *29*, 2550.
- [172] a) Y. Dai, L. Cai, R. E. White, *J. Electrochem. Soc.* **2012**, *160*, A182; b) X. Lin, J. Park, L. Liu, Y. Lee, A. Sastry, W. Lu, *J. Electrochem. Soc.* **2013**, *160*, A1701.
- [173] F. Sagane, K. Miyazaki, T. Fukutsuka, Y. Iriyama, T. Abe, Z. Ogumi, *Chem. Lett.* **2010**, *39*, 826.
- [174] F. Sagane, T. Abe, Y. Iriyama, Z. Ogumi, *J. Power Sources* **2005**, *146*, 749.
- [175] T. Abe, F. Sagane, M. Ohtsuka, Y. Iriyama, Z. Ogumi, *J. Electrochem. Soc.* **2005**, *152*, A2151.
- [176] H. Huo, Y. Chen, N. Zhao, X. Lin, J. Luo, X. Yang, Y. Liu, X. Guo, X. Sun, *Nano Energy* **2019**, *61*, 119.
- [177] A. Mehrotra, P. N. Ross, V. Srinivasan, *J. Electrochem. Soc.* **2014**, *161*, A1681.
- [178] a) A. Ray, B. Saruhan, *Materials* **2021**, *14*, 2942; b) W.-L. Yuan, X. Yang, L. He, Y. Xue, S. Qin, G.-H. Tao, *Front. Chem.* **2018**, *6*, 59.
- [179] J. Nilsson-Hallén, B. Ahlström, M. Marczewski, P. Johansson, *Front. Chem.* **2019**, *7*, 126.
- [180] P. Ray, A. Balducci, B. Kirchner, *J. Phys. Chem. B* **2018**, *122*, 10535.
- [181] a) A. A. Teran, M. H. Tang, S. A. Mullin, N. P. Balsara, *Solid State Ionics* **2011**, *203*, 18; b) H. Choe, B. Carroll, D. Pasquariello, K. Abraham, *Chem. Mater.* **1997**, *9*, 369; c) G. Appetecchi, D. Zane, B. Scrosati, *J. Electrochem. Soc.* **2004**, *151*, A1369.
- [182] a) X. Zhang, B.-Q. Xu, Y.-H. Lin, Y. Shen, L. Li, C.-W. Nan, *Solid State Ionics* **2018**, *327*, 32; b) X. Zhang, T. Liu, S. Zhang, X. Huang, B. Xu, Y. Lin, B. Xu, L. Li, C.-W. Nan, Y. Shen, *J. Am. Chem. Soc.* **2017**, *139*, 13779.
- [183] T. Kato, T. Hamanaka, K. Yamamoto, T. Hirayama, F. Sagane, M. Motoyama, Y. Iriyama, *J. Power Sources* **2014**, *260*, 292.
- [184] E. Yi, H. Shen, S. Heywood, J. Alvarado, D. Y. Parkinson, G. Chen, S. W. Sofie, M. M. Doeff, *ACS Appl. Energy Mater.* **2020**, *3*, 170.
- [185] J. Zagórski, B. Silván, D. Saurel, F. Aguesse, A. Llordés, *ACS Appl. Energy Mater.* **2020**, *3*, 8344.
- [186] C. Peebles, R. Sahore, J. A. Gilbert, J. C. Garcia, A. Tornheim, J. Bareño, H. Iddir, C. Liao, D. P. Abraham, *J. Electrochem. Soc.* **2017**, *164*, A1579.
- [187] Q. Liu, W. Jiang, M. J. P. Munoz, Y. Liu, Z. Yang, I. Bloom, T. L. Dzwiniel, Y. Li, K. Z. Pupek, Z. Zhang, *ACS Appl. Mater. Interfaces* **2020**, *12*, 23035.
- [188] F. J. Simon, M. Hanauer, A. Henss, F. H. Richter, J. r. Janek, *ACS Appl. Mater. Interfaces* **2019**, *11*, 42186.
- [189] a) B. X. Dong, P. Benington, Y. Kambe, D. Sharon, M. Dolejsi, J. Strzalka, V. F. Burnett, P. F. Nealey, S. N. Patel, *Mol. Syst. Des. Eng.* **2019**, *4*, 597; b) Q. Guo, F. Xu, L. Shen, Z. Wang, J. Wang, H. He, X. Yao, *J. Power Sources* **2021**, *498*, 229934.
- [190] M. R. Busche, T. Drossel, T. Leichtweiss, D. A. Weber, M. Falk, M. Schneider, M.-L. Reich, H. Sommer, P. Adelhelm, J. Janek, *Nat. Chem.* **2016**, *8*, 426.
- [191] a) J. Yan, X. Liu, B. Li, *Adv. Sci.* **2016**, *3*, 1600101; b) J. Vetter, P. Novák, M. R. Wagner, C. Veit, K. C. Möller, J. O. Besenhard, M. Winter, M. Wohlfahrt-Mehrens, C. Vogler, A. Hammouche, *J. Power Sources* **2005**, *147*, 269.
- [192] L. Porz, T. Swamy, B. W. Sheldon, D. Rettenwander, T. Frömling, H. L. Thaman, S. Berendts, R. Uecker, W. C. Carter, Y.-M. Chiang, *Adv. Energy Mater.* **2017**, *7*, 1701003.
- [193] a) X. Han, Y. Gong, K. Fu, X. He, G. T. Hitz, J. Dai, A. Pearse, B. Liu, H. Wang, G. Rubloff, Y. Mo, V. Thangadurai, E. D. Wachsman, L. Hu, *Nat. Mater.* **2017**, *16*, 572; b) W. Luo, Y. Gong, Y. Zhu, K. K. Fu, J. Dai, S. D. Lacey, C. Wang, B. Liu, X. Han, Y. Mo, *J. Am. Chem. Soc.* **2016**, *138*, 12258; c) C. Yang, L. Zhang, B. Liu, S. Xu, T. Hamann, D. McOwen, J. Dai, W. Luo, Y. Gong, E. D. Wachsman, L. Hu, *Proc. Natl. Acad. Sci. USA* **2018**, *115*, 3770.
- [194] B. Liu, L. Zhang, S. Xu, D. W. McOwen, Y. Gong, C. Yang, G. R. Pastel, H. Xie, K. Fu, J. Dai, C. Chen, E. D. Wachsman, L. Hu, *Energy Storage Mater.* **2018**, *14*, 376.
- [195] Y. Ren, T. Liu, Y. Shen, Y. Lin, C.-W. Nan, *Ionics* **2017**, *23*, 2521.
- [196] Y. Gong, K. Fu, S. Xu, J. Dai, T. R. Hamann, L. Zhang, G. T. Hitz, Z. Fu, Z. Ma, D. W. McOwen, X. Han, L. Hu, E. D. Wachsman, *Material. Today* **2018**, *21*, 594.
- [197] D. W. McOwen, S. Xu, Y. Gong, Y. Wen, G. L. Godbey, J. E. Gritton, T. R. Hamann, J. Dai, G. T. Hitz, L. Hu, E. D. Wachsman, *Adv. Mater.* **2018**, *30*, 1707132.

- [198] a) L. Buannic, M. Naviroj, S. M. Miller, J. Zagorski, K. T. Faber, A. Llordés, *J. Am. Ceram. Soc.* **2019**, *102*, 1021; b) H. Shen, E. Yi, S. Heywood, D. Y. Parkinson, G. Chen, N. Tamura, S. Sofie, K. Chen, M. M. Doeff, *ACS Appl. Mater. Interfaces* **2020**, *12*, 3494.
- [199] J. van den Broek, S. Afyon, J. L. M. Rupp, *Adv. Energy Mater.* **2016**, *6*, 1600736.
- [200] R. Pfenninger, M. Struzik, I. Garbayo, E. Stilp, J. L. M. Rupp, *Nat. Energy* **2019**, *4*, 475.
- [201] a) J. Sastre, M. H. Futscher, L. Pompizi, A. Aribia, A. Priebe, J. Overbeck, M. Stiefel, A. N. Tiwari, Y. E. Romanyuk, *Commun. Mater.* **2021**, *2*, 76; b) S. Lobe, C. Dellen, M. Finsterbusch, H. G. Gehrke, D. Sebold, C. L. Tsai, S. Uhlenbruck, O. Guillon, *J. Power Sources* **2016**, *307*, 684.
- [202] a) K. Tadanaga, H. Egawa, A. Hayashi, M. Tatsumisago, J. Mosa, M. Aparicio, A. Duran, *J. Power Sources* **2015**, *273*, 844; b) M. Bitzer, T. Van Gestel, S. Uhlenbruck, B. Hans Peter, *Thin Solid Films* **2016**, *615*, 128.
- [203] A. Bielefeld, D. A. Weber, R. Rueß, V. Glavas, J. Janek, *J. Electrochem. Soc.* **2022**, *169*, 020539.
- [204] H. Fathiannasab, L. Zhu, Z. Chen, *J. Power Sources* **2021**, *483*, 229028.
- [205] a) J. A. Dawson, P. Canepa, T. Famprakis, C. Masquelier, M. S. Islam, *J. Am. Chem. Soc.* **2018**, *140*, 362; b) J.-M. Hu, B. Wang, Y. Ji, T. Yang, X. Cheng, Y. Wang, L.-Q. Chen, *ACS Appl. Mater. Interfaces* **2017**, *9*, 33341.
- [206] H.-C. Yu, M.-J. Choe, G. G. Amatucci, Y.-M. Chiang, K. Thornton, *Comput. Mater. Sci.* **2016**, *121*, 14.
- [207] a) G. Bucci, T. Swamy, Y.-M. Chiang, W. C. Carter, *J. Mater. Chem. A* **2017**, *5*, 19422; b) D. Bistri, C. V. Di Leo, *J. Electrochem. Soc.* **2021**, *168*, 030515.
- [208] a) J. Sunarso, S. Baumann, J. M. Serra, W. A. Meulenberg, S. Liu, Y. S. Lin, J. C. Diniz da Costa, *J. Membr. Sci.* **2008**, *320*, 13; b) C. Sun, R. Hui, J. Roller, *J. Solid State Electrochem.* **2010**, *14*, 1125.
- [209] J. Molenda, A. Stokłosa, T. Bąk, *Solid State Ionics* **1989**, *36*, 53.
- [210] a) M. Park, X. Zhang, M. Chung, G. B. Less, A. M. Sastry, *J. Power Sources* **2010**, *195*, 7904; b) K. J. Griffith, K. M. Wiaderek, G. Cibin, L. E. Marbella, C. P. Grey, *Nature* **2018**, *559*, 556.
- [211] S.-H. Park, P. J. King, R. Tian, C. S. Boland, J. Coelho, C. Zhang, P. McBean, N. McEvoy, M. P. Kremer, D. Daly, J. N. Coleman, V. Nicolosi, *Nat. Energy* **2019**, *4*, 560.
- [212] a) T. Asano, S. Yubuchi, A. Sakuda, A. Hayashi, M. Tatsumisago, *J. Electrochem. Soc.* **2017**, *164*, A3960; b) C. Wang, L. Zhang, H. Xie, G. Pastel, J. Dai, Y. Gong, B. Liu, E. D. Wachsman, L. Hu, *Nano Energy* **2018**, *50*, 393.
- [213] S. B. Ma, H. J. Kwon, M. Kim, S.-M. Bak, H. Lee, S. N. Ehrlich, J.-J. Cho, D. Im, D.-H. Seo, *Adv. Energy Mater.* **2020**, *10*, 2001767.
- [214] a) A. J. Samson, K. Hofstetter, E. Wachsman, V. Thangadurai, *J. Electrochem. Soc.* **2018**, *165*, A2303; b) X. Cheng, J. Huang, W. Qiang, B. Huang, *Ceram. Int.* **2020**, *46*, 3731; c) J. Gao, J. Zhu, X. Li, J. Li, X. Guo, H. Li, W. Zhou, *Adv. Funct. Mater.* **2021**, *31*, 2001918; d) J. Sakamoto, T. Thompson, N. Taylor (University of Michigan), *US20200259211A1* **2020**.
- [215] a) S.-H. Chung, C.-H. Chang, A. Manthiram, *Adv. Funct. Mater.* **2018**, *28*, 1801188; b) X. Zhu, T. Zhao, P. Tan, Z. Wei, M. Wu, *Nano Energy* **2016**, *26*, 565; c) F. Wu, V. Srot, S. Chen, S. Lorgner, P. A. van Aken, J. Maier, Y. Yu, *Adv. Mater.* **2019**, *31*, 1905146.
- [216] a) L. Liu, Z. Wang, H. Li, L. Chen, X. Huang, *Solid State Ionics* **2002**, *152–153*, 341; b) S. Ahmed, S. E. Trask, D. W. Dees, P. A. Nelson, W. Lu, A. R. Dunlop, B. J. Polzin, A. N. Jansen, *J. Power Sources* **2018**, *403*, 56; c) R. Fang, S. Zhao, Z. Sun, D.-W. Wang, H.-M. Cheng, F. Li, *Adv. Mater.* **2017**, *29*, 1606823; d) L. Wang, Z. Wu, J. Zou, P. Gao, X. Niu, H. Li, L. Chen, *Joule* **2019**, *3*, 2086; e) M. W. Chase Jr., *J. Phys. Chem. Ref. Data, Monograph* **1998**, *9*, 1510.
- [217] a) M. Doyle, T. F. Fuller, J. Newman, *J. Electrochem. Soc.* **1993**, *140*, 1526; b) P. Ramadass, B. Haran, P. M. Gomadam, R. White, B. N. Popov, *J. Electrochem. Soc.* **2004**, *151*, A196.
- [218] J. Sturm, A. Rheinfeld, I. Zilberman, F. B. Spingler, S. Kosch, F. Frie, A. Jossen, *J. Power Sources* **2019**, *412*, 204.
- [219] C. Wang, R. Yu, S. Hwang, J. Liang, X. Li, C. Zhao, Y. Sun, J. Wang, N. Holmes, R. Li, H. Huang, S. Zhao, L. Zhang, S. Lu, D. Su, X. Sun, *Energy Storage Mater.* **2020**, *30*, 98.
- [220] a) R. Amin, Y.-M. Chiang, *J. Electrochem. Soc.* **2016**, *163*, A1512; b) H.-J. Noh, S. Youn, C. S. Yoon, Y.-K. Sun, *J. Power Sources* **2013**, *233*, 121.
- [221] L. Wang, R. Xie, B. Chen, X. Yu, J. Ma, C. Li, Z. Hu, X. Sun, C. Xu, S. Dong, T.-S. Chan, J. Luo, G. Cui, L. Chen, *Nat. Commun.* **2020**, *11*, 5889.
- [222] S. Randau, F. Walther, A. Neumann, Y. Schneider, R. S. Negi, B. Mogwitz, J. Sann, K. Becker-Steinberger, T. Danner, S. Hein, A. Latz, F. H. Richter, J. Janek, *Chem. Mater.* **2021**, *33*, 1380.